

**Finite Element Framework for Nanomechanics and  
Electronic Structure Calculations of Semiconductors**

BY

RAGURAMAN KANNAN

B.E., Bharathidasan University, India, 1997  
M.S., Texas A&M University, College Station, 2002

THESIS

Submitted as partial fulfillment of the requirements  
for the degree of Doctor of Philosophy in Materials Engineering  
in the Graduate College of the  
University of Illinois at Chicago, 2011

Chicago, Illinois

Defense Committee:

Mohsen A. Issa, Chair, Department of Civil and Materials Engineering  
Arif Masud, Advisor, University of Illinois, Urbana-Champaign  
Chien H. Wu, Department of Civil and Materials Engineering  
Elisa Budyn, Department of Mechanical and Industrial Engineering  
Sohail Murad, Department of Chemical Engineering

The thesis is dedicated to Hari-Vayu, Raghavendra Swamy, all my Madhwa Gurus, acharyas, brahamanas, my parents (all of whom provided selflessly their monetary and spiritual support through advice and prayers through many turmoils of my life as research assistant), all my teachers and my advisor without whose help it would have never been accomplished.



## ACKNOWLEDGMENT

Nanomechanics part of this work was partially supported by Office of Naval Research Grant N000014-02-1-0143, and the National Academy of Sciences Grant NAS 7251-05-005. This support is gratefully acknowledged. I Would like to thank especially my advisor, Dr. Arif Masud, for his invaluable guidance throughout my research work. I am indeed indebted to him without whose support I could not have finished my research work. I would also like to gratefully acknowledge retired Professor Richard Martin and also Dr. John E. Pask for their invaluable guidance in electronic structure calculations. I like to thank also Dr. Nahil Sobh for his guidance on parallelization of codes using OpenMP and helping us with directions on electronic structure calculations.

I would also like to thank graduate student JaeHyuk Kwack for his help on finding iterative solvers for the code. Last but not the least, I would like thank Harishankar Gajendran, for parallelizing the electronic structure code using MPI, drawing pictures for the thesis work and running codes for convergence tests.

RK

## TABLE OF CONTENTS

| <u>CHAPTER</u> |  | <u>PAGE</u> |
|----------------|--|-------------|
| <b>1</b>       | <b>INTRODUCTION . . . . .</b>  | <b>1</b>    |
| 1.1            | Nanomechanics . . . . .  | 2           |
| 1.2            | Electronic Structure Calculations . . . . .  | 5           |
| 1.2.1          | Stabilized variational formulation . . . . .   | 5           |
| 1.2.2          | B-spline and NURBS based finite element methods for full electronic structure calculations . . . . . | 6           |
| <b>2</b>       | <b>NANOMECHANICS . . . . .</b>   | <b>9</b>    |
| 2.1            | A Multiscale Computational Framework . . . . .   | 9           |
| 2.1.1          | Two-level scale separation . . . . .   | 9           |
| 2.1.2          | Main points of the multiscale framework . . . . .  | 14          |
| 2.2            | Atomic Scale Parameter Dependent Material Properties of Nanotubes . . . . .                          | 15          |
| 2.2.1          | Molecular mechanics model . . . . .  | 15          |
| 2.2.2          | The stick-spiral model . . . . .   | 17          |
| 2.2.2.1        | Equilibrium relations . . . . .  | 19          |
| 2.2.2.2        | Kinematic relations . . . . .  | 19          |
| 2.2.3          | Extracting the quasi-continuum mechanical properties for CNTs . . . . .                              | 20          |
| 2.2.3.1        | Procedural outline for extracting nanoscale dependent properties . . . . .                           | 22          |
| 2.3            | A Framework for Modeling Point Defects in Nanotubes . . . . .  | 23          |
| 2.3.1          | Formation energy of vacancy . . . . .  | 24          |
| 2.3.2          | Evaluation of the force component $\mathbf{f}'$ . . . . .  | 27          |
| 2.3.3          | Salient features of the formulation for modeling defects in nanostructures . . . . .                 | 28          |
| 2.4            | Numerical Results . . . . .  | 30          |
| 2.4.1          | Mechanical response of defect-free nanotubes . . . . .   | 31          |
| 2.4.2          | Mechanical response of nanotubes with topographical defects . . . . .                                | 33          |
| <b>3</b>       | <b>STABILIZED FINITE ELEMENT METHOD FOR SWE . . . . .</b>  | <b>37</b>   |
| 3.1            | The Schrödinger Wave Equation . . . . .  | 37          |
| 3.1.1          | The Standard weak form . . . . .   | 38          |
| 3.2            | The Galerkin/Least-Square Stabilized Form . . . . .  | 39          |
| 3.3            | The Variational Multiscale Method . . . . .  | 40          |

## TABLE OF CONTENTS (Continued)

| <u>CHAPTER</u> |   | <u>PAGE</u> |
|----------------|---|-------------|
| 3.3.1          | The multiscale variational problem . . . . .  | 41          |
| 3.3.2          | Solution of the fine scale problem ( $w'$ ) . . . . .   | 42          |
| 3.3.3          | The coarse scale problem ( $\bar{w}$ ) . . . . .  | 44          |
| 3.3.4          | The HVM stabilized form . . . . .   | 45          |
| 3.3.5          | Quadratic eigenvalue problem for the HVM form . . . . .   | 46          |
| 3.4            | Numerical Examples . . . . .  | 46          |
| 3.4.1          | Convergence rate results for the GLS stabilized formulation . . . . .                             | 48          |
| 3.4.2          | Convergence rate results for the HVM formulation . . . . .  | 51          |
| 3.4.3          | Energy band diagram . . . . .   | 53          |
| 3.4.4          | Convergence rate for a high value of the electronic potential . . . . .                           | 55          |
| <b>4</b>       | <b>B-SPLINES AND NURBS FINITE ELEMENT METHODS FOR ELECTRONIC STRUCTURE CALCULATIONS . . . . .</b> | <b>60</b>   |
| 4.1            | Kohn-Sham Equations . . . . .   | 60          |
| 4.1.1          | Solution of periodic systems . . . . .  | 63          |
| 4.1.2          | Schrödinger wave equation . . . . .   | 63          |
| 4.1.3          | The standard weak form . . . . .  | 66          |
| 4.1.4          | The Poisson problem . . . . .   | 68          |
| 4.1.5          | The standard weak form for the Poisson problem . . . . .  | 69          |
| 4.2            | B-splines and NURBS . . . . .   | 70          |
| 4.2.1          | Knot vectors . . . . .  | 71          |
| 4.2.2          | Definition and properties of B-splines . . . . .  | 72          |
| 4.2.3          | Curves as B-spline parametric functions . . . . .   | 73          |
| 4.2.4          | $h$ -refinement, $p$ -refinement and $k$ -refinement . . . . .                                    | 74          |
| 4.2.5          | Higher dimensional B-splines . . . . .  | 76          |
| 4.2.6          | Rational B-splines . . . . .  | 77          |
| 4.3            | Numerical Results . . . . .   | 78          |
| 4.3.1          | Kronig-Penney problem (3D case) . . . . .   | 78          |
| 4.3.2          | Poisson problem . . . . .   | 81          |
| 4.3.2.1        | Test problem . . . . .  | 81          |
| 4.3.2.2        | Triclinic model . . . . .   | 85          |
| 4.3.2.3        | Silicon empirical pseudopotential . . . . .   | 90          |
| 4.3.3          | Schrödinger equation: Silicon empirical pseudopotential . . . . .                                 | 95          |
| 4.3.4          | Self-consistent study . . . . .   | 97          |
| 4.3.4.1        | Indium atom with all electron potential (1D case) . . . . .                                       | 98          |
| 4.3.4.2        | Bulk silicon and self-consistent procedure . . . . .  | 104         |
| 4.3.4.3        | Gallium arsenide (GaAs) . . . . .   | 107         |
| 4.3.4.4        | Graphene (3D case) . . . . .  | 110         |
| <b>5</b>       | <b>CONCLUDING REMARKS AND FUTURE WORK . . . . .</b>   | <b>112</b>  |
|                | <b>APPENDICES . . . . .</b>   | <b>115</b>  |
|                | <b>Appendix A . . . . .</b>   | <b>116</b>  |

## TABLE OF CONTENTS (Continued)

| <u>CHAPTER</u>             | <u>PAGE</u> |
|----------------------------|-------------|
| Appendix B . . . . .       | 118         |
| CITED LITERATURE . . . . . | 119         |
| VITA . . . . .             | 126         |

## LIST OF TABLES

| <u>TABLE</u> |  | <u>PAGE</u> |
|--------------|--|-------------|
| I            | SOURCE PASK <i>ET AL.</i> [1]. THE RECIPROCAL LATTICE VECTOR $\mathbf{G}$ IS DEFINED IN TERMS OF PRIMITIVE RECIPROCAL LATTICE VECTORS $\mathbf{B}_1$ , $\mathbf{B}_2$ AND $\mathbf{B}_3$ . . . . . | 86          |
| II           | THE RECIPROCAL LATTICE VECTOR $\mathbf{G}$ IS DEFINED IN TERMS OF PRIMITIVE RECIPROCAL LATTICE VECTORS $\mathbf{B}_1$ , $\mathbf{B}_2$ AND $\mathbf{B}_3$ [2] . . . . .                            | 91          |
| III          | TOTAL ENERGY FOR INDIUM ATOM FOR B-SPLINE ORDER K=4 AND MESH RESOLUTIONS N=200 AND N=400. IN COLUMN NIST REFERENCE VALUES ARE PROVIDED. ALL VALUES ARE IN HARTREE . . . . .                        | 101         |

## LIST OF FIGURES

| <b><u>FIGURE</u></b>  | <b><u>PAGE</u></b> |
|---|--------------------|
| 1      Schematic force and moment balance diagram for a typical pattern of four carbon atoms connected via three bond lengths. Localized strains are supposed to be homogeneous at a given point though they may change from point to point in the domain (see [3] for details). . . . .  | 18                 |
| 2      Relaxation of atoms around the defect. (a) Hexagonal pattern without defect, divacancy sites shown in red (b) Configuration of atoms with divacancy and dangling bonds. Immediate neighboring atoms, shown in blue are allowed to relax. (c) Relaxation and reconfiguration of atoms around divacancy. . . . .   | 25                 |
| 3      Schematic diagram of finite element mesh indicating the element that possesses the defective patch. Computational cell is defined as a subinterval of the refined mesh that overlays the element containing defect. In this context element of the coarse mesh that contains defect becomes a super-element. Point defect in the cell is indicated by the dot. . . . . | 28                 |
| 4      Young's modulus for non-defective nanotubes . . . . .  | 32                 |
| 5      Poisson's ratio for non-defective nanotubes . . . . .  | 32                 |
| 6      A schematic diagram of frozen divacancy defect . . . . .   | 33                 |
| 7      Stress strain response for non-defective nanotube . . . . .  | 35                 |
| 8      Stress strain response of defective nanotube . . . . .   | 35                 |
| 9      Young's modulus as function of strain for non-defective nanotubes . . .  | 36                 |
| 10     Young's modulus as function of strain for defective nanotubes . . . . .  | 36                 |
| 11     A family of 3-D linear and quadratic elements. . . . .   | 48                 |

## LIST OF FIGURES (Continued)

| <b><u>FIGURE</u></b> |  | <b><u>PAGE</u></b> |
|----------------------|--|--------------------|
| 12                   | Convergence rates for eigenvalues using linear brick elements. . . . .                   | 49                 |
| 13                   | Convergence rates for eigenvalues using linear tetrahedral elements. . .                 | 49                 |
| 14                   | Convergence rates for eigenvalues using quadratic brick elements. . . . .                | 50                 |
| 15                   | Convergence rates for eigenvalues using quadratic tetrahedral elements.                  | 50                 |
| 16                   | Convergence rates for eigenvalues using linear brick elements. . . . .                   | 51                 |
| 17                   | Convergence rates for eigenvalues using linear tetrahedral elements. . .                 | 52                 |
| 18                   | Convergence rates for eigenvalues using quadratic brick elements. . . . .                | 52                 |
| 19                   | Convergence rate for eigenvalues using quadratic tetrahedral elements.                   | 53                 |
| 20                   | Energy band diagram for the GLS formulation. . . . .                                     | 54                 |
| 21                   | Energy band diagram for the HVM formulation. . . . .                                     | 54                 |
| 22                   | Convergence rates for eigenvalues using linear brick elements (GLS). . .                 | 55                 |
| 23                   | Convergence rates for eigenvalues using linear tetrahedral elements (GLS).               | 56                 |
| 24                   | Convergence rates for eigenvalues using quadratic brick elements (GLS).                  | 56                 |
| 25                   | Convergence rates for eigenvalues using quadratic tetrahedral elements<br>(GLS). . . . . | 57                 |
| 26                   | Convergence rates for eigenvalues using linear brick elements (HVM). .                   | 57                 |
| 27                   | Convergence rates for eigenvalues using linear tetrahedral elements (HVM).               | 58                 |
| 28                   | Convergence rates for eigenvalues using quadratic brick elements (HVM).                  | 58                 |
| 29                   | Convergence rates for eigenvalues using quadratic tetrahedral elements<br>(HVM). . . . . | 59                 |
| 30                   | Convergence rates for second order NURBS . . . . .                                       | 79                 |
| 31                   | Convergence plots for second order B-Splines . . . . .                                   | 79                 |
| 32                   | Energy band diagram for quadratic B-splines with mesh $8^3$ mesh . . . .                 | 81                 |

## LIST OF FIGURES (Continued)

| <u>FIGURE</u> |   | <u>PAGE</u> |
|---------------|---|-------------|
| 33            | Plot of the potential along the body diagonal (a) $p = 2$ , (b) $p = 3$ , (c) $p = 4$ . . . . .   | 83          |
| 34            | Error in the potential along the body diagonal (a) $p = 2$ , (b) $p = 3$ , (c) $p = 4$ . . . . .  | 84          |
| 35            | Convergence rates for the Poisson problem with analytical potential, $V = \sin(2\pi x) \sin(2\pi y) \sin(2\pi z)$ . . . . .                                     | 85          |
| 36            | Plot of the potential along the body diagonal for triclinic model (a) $p=2$ , (b) $p=3$ , (c) $p=4$ . . . . .   | 87          |
| 37            | Error in the potential along the body diagonal for triclinic model (a) $p=2$ , (b) $p=3$ , (c) $p=4$ . . . . .  | 88          |
| 38            | Convergence rates for the triclinic model . . . . .   | 89          |
| 39            | Plot of the potential along the body diagonal for silicon empirical pseudo-potential (a) $p = 2$ , (b) $p = 3$ , (c) $p = 4$ . . . . .                          | 92          |
| 40            | Error in the potential along the body diagonal for silicon empirical pseudo-potential (a) $p = 2$ , (b) $p = 3$ , (c) $p = 4$ . . . . .                         | 93          |
| 41            | Convergence rates for the silicon empirical pseudo-potential . . . . .  | 94          |
| 42            | Convergence rates for the first five eigenvalues at a given $\mathbf{k}$ point. . . .   | 95          |
| 43            | Band structure for silicon pseudo-potential (a) $p = 2$ , (b) $p = 3$ . . . . .   | 96          |
| 44            | Convergence plot for $E_t(\rho)$ as a function of $numel$ . . . . .   | 102         |
| 45            | Convergence plot for energies (equations 74-78) as a function of radial domain length, $\xi$ for B-spline order $\mathbf{p} = 4$ and 200 elements . . . . .     | 102         |
| 46            | Convergence plot for energies (equations 74-78) as a function of radial domain length, $\xi$ for B-spline order $\mathbf{p} = 4$ and 400 elements . . . . .     | 103         |
| 47            | Convergence plot for total energies of each orbital as a function of radial domain length, $\xi$ for B-spline order $\mathbf{p} = 4$ and 200 elements . . . . . | 103         |
| 48            | Convergence plot for total energies of each orbital as a function of radial domain length, $\xi$ for B-spline order $\mathbf{p} = 4$ and 400 elements . . . . . | 104         |



## LIST OF FIGURES (Continued)

| <u>FIGURE</u> |   | <u>PAGE</u> |
|---------------|---|-------------|
| 49            | Conventional unit cell and Primitive unit cell. . . . .                   | 105         |
| 50            | First Brillouin zone and irreducible wedge . . . . .                      | 105         |
| 51            | Band diagram for Bulk silicon and B-spline order $p = 2$ . . . . .        | 106         |
| 52            | Band diagram for Bulk silicon and B-spline order $p = 3$ . . . . .        | 106         |
| 53            | Band diagram for gallium arsenide (GaAs) and B-spline order $p = 2$ . .   | 108         |
| 54            | Band diagram for gallium arsenide (GaAs) and B-spline order $p = 3$ . .   | 108         |
| 55            | Convergence rates for gallium arsenide (GaAs) and B-spline order $p = 2$  | 109         |
| 56            | Primitive unit cell and First Brillouin zone with high-symmetry points    | 111         |
| 57            | Band diagram for graphene and B-spline order $p = 2$ . . . . .            | 111         |
| 58            | Silicon Local pseudopotential [2, 4] and its corresponding charge density | 118         |

## LIST OF ABBREVIATIONS

|       |                                |
|-------|--------------------------------|
| SWE   | Schrödinger Wave Equation      |
| DFT   | Density Functional Theory      |
| NURBS | Non-uniform Rational B-Splines |
| PW    | Planewave                      |

## SUMMARY

This thesis presents a variational computational framework for nanomechanics and electronic structure calculations of semiconductors. In order to predict the properties of semiconductor devices involving coupling between mechanical and electronic properties like flexible electronics, a scalable computational framework is the need of the time. The thesis provides the first step towards carrying out such computations by providing a real space method for electronic computations and computationally efficient nanomechanics framework. However further study is required to combine mechanical and electronic computational framework.

A multiscale computational framework using finite element method is presented for nanomechanics problems that combines fully coupled discrete models like molecular structural mechanics models at small scales and quasi-continuum mechanics models at larger scales. The quasi-continuum models use material moduli defined via internal variables which are functions of local atomic configuration, while the molecular mechanics model incorporates interatomic potentials into its discrete model to derive nanoscale based material moduli. Point defects like vacancy perturb the local atomic configuration and induce forces locally. A homogenization scheme is used to evaluate the equivalent material moduli around the defect area by evaluation of defect formation energy and incorporating it into molecular structural mechanics model. The hierarchical multiscale finite element framework seamlessly combines both discrete and quasi-

## SUMMARY (Continued)

continuum models at each integration point and evaluates stress strain response and material properties for defective and non-defective material. Representative examples are provided.

For electronic structure calculations the thesis starts with a study of stabilized formulation of Schrödinger wave equation and numerical studies are conducted with Lagrange basis functions for tetrahedral and hexahedral elements for three dimensional Kronig-Penney problem. It is followed by presentation of B-splines and NURBS based finite element formulation for linear Schrödinger wave equation and non-linear, non-local Kohn-Sham equations. The higher order continuity and variation diminishing property of B-splines and NURBS basis functions offer significant advantage over  $C^0$  Lagrange basis functions for representing high gradient solutions with higher precision. In addition NURBS functions accurately represent geometries including conic sections with minimum parameters thus avoiding errors due to boundary conditions and/or geometries in electronic structure calculations. Self-consistent Kohn-Sham equations consisting of Schrödinger wave equation and Poisson equations are solved. Representative examples are provided for bulk gallium Arsenide, silicon and graphene and compared with planewave solutions.

## 1 INTRODUCTION

This thesis provides a computational framework for multiscale nanomechanics problems and also a real space finite element framework for *ab initio* electronic structure calculations. The thesis consists of two parts. The first part deals with a computational framework to seamlessly combine quasi-continuum models and discrete models, like molecular mechanics or *ab initio* calculations, in order to predict mechanical response and mechanical properties of nanoscale materials with presence of defects or other local configuration changes at atomic level. The section on nanomechanics gives a detailed background.

In order to efficiently combine discrete models like molecular-mechanics or *ab initio* electronic structure calculations with quasi continuum models and to evaluate the coupled mechanical and electronic properties of materials like flexible electronic devices, a robust and scalable computational model for electronic structure calculations is the need of the day. Particularly computational models for electronic structure calculations based on real space methods like finite element methods is an active area of research. This thesis is preliminary step to towards this direction. The section on electronic structure calculations details the present scenario and significant developments in our work.

## 1.1 Nanomechanics

This section of thesis demonstrates the computational framework in the context of defective and non-defective Carbon nanotubes (CNTs). CNTs are cylindrical molecules composed of carbon atoms in a periodic hexagonal arrangement. From a nanostructure viewpoint CNTs can be regarded as graphene sheets, i.e., 2-D array of carbon atoms in a hexagonal pattern, rolled up in a way as to form seamless cylinders [5]. Nanotubes possess remarkable mechanical and electronic properties that make them promising candidates for application in nanotechnology [6, 7]. Modeling of these nanomaterials involves phenomena with multiple spatial and temporal scales and this has attracted considerable attention from the research community. In general two approaches have been adopted by various researchers to describe material properties at small and large length scales: (i) the bottom up approach that is based on quantum/molecular mechanics, and (ii) the top down approach that is based on continuum mechanics. A good account of the modeling issues in CNTs and an overview of the various methods proposed in the literature is presented in Liu and coworkers [8, 9], Belytschko *et al.* [10–12], Yakobson and coworkers [13, 14], and references therein.

The availability of accurate interatomic potentials makes classical MD simulations a prominent tool for modeling nanotubes [15–19]. However single scale methods such as ab initio quantum mechanical methods or molecular dynamics (MD) methods have difficulty in analyzing hybrid structures due to the limitations in terms of the time and the length scales that these methods are confined to [9, 11]. Qian *et al.* [8] indicate that despite the increase in the computational power and improvement in algorithms, classical molecular dynamics simulation is limited

to 106-108 atoms for a few nanoseconds. On the other hand pure continuum based models for nanomechanics are not sensitive to the changes in the local atomic configurations and therefore cannot account for the nanoscale effects. One numerical approach that has been applied to many problems is to use MD only in localized regions in which the atomic-scale dynamics are important, while using a continuum simulation method everywhere else [11, 20–22]. The issue of disparate time scales in the two regions has been addressed and some simplified treatments of the interface between the atomistic and continuum regimes have been proposed [9]. Huang and coworkers have proposed a nanoscale based continuum theory [23, 24], and Gao and coworkers have developed stick-spiral models for CNTs and graphene sheet [3]. In the present era of nanotechnology, it has become increasingly important to model phenomena at microscopic length scales that lie between the mesoscopic scales and the nanoscales. However a microscopic model can involve up to a scale of several microns consisting of billions of atoms, which is outside the range of MD simulations to date [8]. In view of these technical difficulties, new multiscale approaches are required to successfully address the class of problems where molecular scales interact with microscales [25]. For some successful multiscale approaches that provide a link between quantum/molecular and continuum descriptions of the material properties, the interested reader is referred to the works of Belytschko and coworkers [11], Liu and coworkers [8, 9], and Huang and coworkers [26] (and references therein).

This part of thesis presents a mathematically consistent multiscale computational framework for bridging the gap between molecular mechanics and quasi-continuum mechanics in the modeling of carbon nanotubes. Contrary to the computational nesting of information from smaller scales into the larger ones, we propose a novel mathematical nesting of scales that yields

the hierarchical multiscale method. We employ two overlapping domains: a quasi-continuum domain for the defect free graphene sheets and nanotubes, and an atomistic domain that overlays the region containing point defects and models the localized fields around defects. For the modeling of the quasi-continuum domain, interatomic potentials [15,19] are incorporated in the stick-spiral model of Chang and Gao [3] that yields nanoscale based mechanical material moduli via a set of analytical equations. These material moduli are functions of internal variables of changes in bond lengths and bond angles, and are then used in the quasi-continuum modeling of the defect free nanostructures. In the atomistic calculations around the point defects, the formation energy of vacancy (section 2.3.1) [27,28] is evaluated and employed in conjunction with the stick-spiral model [3] to account for the local changes in the atomic structure and to generate the localized force fields. These localized nanoscale force fields are then used in the variational multiscale method to model the localized displacements in the vicinity of vacancies and defects.

An outline of the chapter 2 is as follows. In section 2.1 we present the general variational multiscale framework that underlies the proposed computational nanomechanics method. Section 2.2 presents the stick-spiral molecular mechanics model of Chang and Gao [3] embedded with interatomic potentials [15,19] to extract scale dependent material properties of continuously deforming CNTs. Section 2.3 presents the formation energy of vacancy that is employed to extract the localized material properties in the vicinity of the defects, and a method to extract the driving forces for the modeling of mechanical fields around the point defects. Numerical results are presented in Section 2.4.



## 1.2 Electronic Structure Calculations

This section of thesis consists of two parts.

### 1.2.1 Stabilized variational formulation

The first part deals with numerical study of linear SWE with Lagrange basis functions. The time-independent Schrödinger equation, termed as the Schrödinger wave equation (SWE) is used to determine the electronic structure of periodic solids. SWE has a differential form that involves continuous functions of continuous variables, and is therefore suitable for the application of variational methods to the study of electronic properties of periodic materials. The eigen-solutions of SWE correspond to different quantum states of the system. Various numerical approaches have been adopted for the solution of SWE that include finite element [2, 29–31] and finite difference methods [32, 33]. The advantages and utility of finite element method over ab-initio methods is discussed in detail in [29].

In this section we explore two variational formulations for SWE. Our objective is to study the convergence properties of the finite element methods based on the proposed variational formulations where we have employed lower-order standard Lagrange interpolation functions. We are motivated by the notion of subgrid scale methods [34, 35] which in the present context can help in an accurate calculation of higher eigenvalues in the system. Stabilized methods based on variational multiscale ideas, when applied to a number of physical phenomena [36–40] have shown higher accuracy on cruder discretizations as compared to the corresponding standard Galerkin formulations.

An outline of chapter 3 is as follows. Section 3.1 presents the Schrödinger wave equation and its standard Galerkin form. Section 3.2 presents the Galerkin/Least-Squares (GLS) formulation for SWE. Section 3.3 develops a stabilized formulation that is motivated by the variational multiscale ideas. Section 3.4 presents results that demonstrate the accuracy and convergence properties of the methods for a model problem (Kronig-Penney problem) for which analytical results are available.

### **1.2.2 B-spline and NURBS based finite element methods for full electronic structure calculations**

First-principles (ab-initio) computational techniques like density functional theory (DFT) [41, 42] has provided important insight into the electronic and chemical properties of real materials, namely those containing defects, impurities, surfaces etc., without the need to have any experimental data as input. In DFT, Schrödinger wave equation and Poisson equation are solved self-consistently until convergence is achieved. Traditional numerical techniques in this field use plane-wave (PW) basis functions [43, 44], which are not local in real space. This (a.) seriously limits the size of the problem that can be solved as global basis functions like PW leads to  $O(N^3)$  system where  $N$  refers to the number of PW basis functions in the system; (b.) introduces inefficiencies in parallel implementation of code due to communication between processors for evaluation of non-local terms; (c.) PW basis have the same resolution everywhere in real space and thus is inefficient for problems with local inhomogeneities or where local electron states are important; (d.) In addition PW basis functions are limited to periodic boundary condition, which is disadvantageous with respect to cluster and surface calculations; (e.) Fourier

transform, which is inefficient for parallel computing, is required for PW method. As an attempt to overcome these inefficiencies of PW method, a finite element variational framework is suggested. In finite element framework basis functions have local support, thus minimizes communication in parallel codes. In addition algorithms can be designed to lead to a linear scaling system because of local support of basis functions, which is highly advantageous for solving large scale problems. Finite element framework allows implementation of Dirichlet, Neumann, mixed in addition to periodic boundary conditions and thus useful for cluster and surface calculations. For more detailed discussion on this topic please refer Pask *et al.* [1]. Recently Pask *et al.* [1,2] has used  $C^0$  Lagrange basis functions for DFT calculations in finite element framework limited to pseudopotential formulation [45]. In this paper we use higher order formulation using B-spline and NURBS basis functions in finite element framework. Hughes *et al.* [46] have demonstrated the use of B-spline and NURBS basis functions in the context of solid mechanics and finite element framework. The advantage of B-spline and NURBS basis functions with respect to Lagrange basis functions are (a.) B-splines and NURBS provide  $C^p$  or  $C^{p-k}$  basis functions, where  $p$  is the order of B-spline or NURBS basis function and  $k$  refers to multiplicity of knot values in knot vector. This will be explained in detail in the section 4.2. Higher order basis functions can represent high gradient functions as atomic potentials more accurately. (b.) In addition, unlike Lagrange basis functions display Gibbs phenomenon for higher order polynomials, B-spline and NURBS functions have variation diminishing property [46]. This property again is useful in representing high gradients in solution more accurately. (c.) NURBS functions can represent geometries with conic sections, like cylinders or spheres, accurately with

minimum parameters, unlike Lagrange basis function where geometry has to be approximated. This is useful in accurately applying boundary conditions, thus avoiding errors in computation.

In section 4.1, we review the solution of Kohn-Sham equations in finite element framework. Then we give an introduction to B-spline and NURBS basis functions and their relevant properties in section 4.2. In section 4.3, we discuss the some numerical results for both self-consistent and non-self-consistent solution of Schrdinger wave equation.

## 2 NANOMECHANICS

### 2.1 A Multiscale Computational Framework

A mathematically consistent multiscale framework for bridging the gap between molecular mechanics (fine scales) and quasi-continuum mechanics (microscales) is presented here for the modeling of micro- and nanostructures. A hierarchical multiscale variational framework based on the work of Masud *et al.* [47, 48], and Masud and Franca [35], the key ideas underlying the proposed multiscale method for computational micro- and nanomechanics is illustrated.

#### 2.1.1 Two-level scale separation

Let  $\Omega \subset \mathbb{R}^{n_{sd}}$  be an open bounded region with piecewise smooth boundary  $\Gamma$ . In general the number of space dimensions  $n_{sd}$  is equal to 3, however for planar nanomaterials like graphene sheets or unwrapped nanotubes  $n_{sd}$  is equal to 2. Boundary  $\Gamma$  admits a unique decomposition  $\Gamma = \Gamma_g \cup \Gamma_h$ , where  $\Gamma_g$  and  $\Gamma_h$  are parts of the boundary with prescribed Dirichlet and Neumann conditions, respectively. Let  $\mathcal{L}$  be the operator of the equation governing the deformation of the nanostructure. Abstract form of the governing equation is:

$$\mathcal{L}u = f \text{ in } \Omega \tag{2.1}$$

where  $\mathbf{u}$  is the unknown field, and  $\mathbf{f}$  is the forcing function. Without loss of generality we consider Dirichlet type boundary conditions  $\mathbf{u} = g$  on  $\Gamma_g$ . The standard variational form can be expressed as:

$$(\mathbf{w}, \mathcal{L}\mathbf{u}) = (\mathbf{w}, \mathbf{f}) \quad (2.2)$$

where  $\mathbf{w}$  represents the appropriate test functions, and  $(\cdot, \cdot) = \int_{\Omega} (\cdot) d\Omega$  is the  $L_2(\Omega)$  - inner product. We consider discretization of the domain into non overlapping subregions/elements. The sum over the interiors of these subregions is indicated as  $\Omega'$  and is defined as  $\Omega' = \bigcup_{e=1}^{numel} (int) \Omega^e$ , where *numel* is the total number of elements in the computational grid. The sum over element boundaries is indicated as  $\Gamma'$  and is defined as  $\Gamma' = \bigcup_{e=1}^{numel} \Gamma^e$ .

We assume an overlapping additive decomposition of the total solution into coarse scales  $\tilde{\mathbf{u}}$  (i.e., meso-to-micro scales) and fine scales  $\mathbf{u}'$  (i.e., micro-to nano scales), represented as

$$\mathbf{u} = \tilde{\mathbf{u}} + \mathbf{u}' \quad (2.3)$$

Likewise we assume an overlapping sum decomposition of the weighting function

$$\mathbf{w} = \tilde{\mathbf{w}} + \mathbf{w}', \quad (2.4)$$

where  $\tilde{\mathbf{w}}$  are the weighting functions for the coarse scales and  $\mathbf{w}'$  are the weighting functions for the fine scales. To keep the presentation simple and without loss of generality, we assume that the fine scales vanish at the inter-element boundaries  $\Gamma'$ .

We also assume a unique additive decomposition of the forcing function into coarse scales  $\tilde{\mathbf{f}}$  (meso-to-micro) and fine scales  $\mathbf{f}'$  (micro-to-nano) components, represented as

$$\mathbf{f} = \tilde{\mathbf{f}} + \mathbf{f}' \quad (2.5)$$

Substituting the additively decomposed  $\mathbf{u}$ ,  $\mathbf{w}$  and  $\mathbf{f}$  in (2.2) we get

$$(\tilde{\mathbf{w}} + \mathbf{w}', \mathcal{L}(\tilde{\mathbf{u}} + \mathbf{u}')) = (\tilde{\mathbf{w}} + \mathbf{w}', \tilde{\mathbf{f}} + \mathbf{f}') \quad (2.6)$$

The proposed decomposition of the forcing function gives rise to a further decomposition of the coarse and fine scale solutions such that

$$\tilde{\mathbf{u}} = \tilde{\mathbf{u}}_{\tilde{\mathbf{f}}} + \tilde{\mathbf{u}}_{\mathbf{f}'} \quad (2.7)$$

$$\mathbf{u}' = \mathbf{u}'_{\tilde{\mathbf{f}}} + \mathbf{u}'_{\mathbf{f}'} \quad (2.8)$$

wherein  $\tilde{\mathbf{u}}_{\tilde{\mathbf{f}}}$  and  $\mathbf{u}'_{\tilde{\mathbf{f}}}$  are the coarse and fine scale components of the solution that arise because of meso-to-micro force terms  $\tilde{\mathbf{f}}$ . Similarly,  $\tilde{\mathbf{u}}_{\mathbf{f}'}$  and  $\mathbf{u}'_{\mathbf{f}'}$  are the coarse and fine scale components of the solution that arise because of micro-to-nano force terms  $\mathbf{f}'$ . Substituting (2.7) and (2.8) in (2.6) we get

$$(\tilde{\mathbf{w}} + \mathbf{w}', \mathcal{L}((\tilde{\mathbf{u}}_{\tilde{\mathbf{f}}} + \tilde{\mathbf{u}}_{\mathbf{f}'}) + (\mathbf{u}'_{\tilde{\mathbf{f}}} + \mathbf{u}'_{\mathbf{f}'}))) = (\tilde{\mathbf{w}} + \mathbf{w}', \tilde{\mathbf{f}} + \mathbf{f}') \quad (2.9)$$

Equation (2.9) yields a fully coupled system for the coarse and fine solution fields that arise because of the meso-micro forcing functions  $\tilde{\mathbf{f}}$  and the micro-nano forcing function  $\mathbf{f}'$ . Assuming a unique additive decomposition of  $\mathbf{f}$  into  $\tilde{\mathbf{f}}$  and  $\mathbf{f}'$ , we can split (2.9) into two sub-problems.

Meso-Micro Scale Problem:

$$(\tilde{\mathbf{w}} + \mathbf{w}', \mathcal{L}(\tilde{\mathbf{u}}_{\tilde{\mathbf{f}}} + \mathbf{u}'_{\tilde{\mathbf{f}}})) = (\tilde{\mathbf{w}} + \mathbf{w}', \tilde{\mathbf{f}}) \quad (2.10)$$

Micro-Nano Scale Problem:

$$\left( \tilde{\mathbf{w}} + \mathbf{w}', \mathcal{L} \left( \tilde{\mathbf{u}}_{\mathbf{f}'} + \mathbf{u}'_{\mathbf{f}'} \right) \right) = (\tilde{\mathbf{w}} + \mathbf{w}', \mathbf{f}') \quad (2.11)$$

**Remark 2.1:** In this framework  $\tilde{\mathbf{f}}$  represents the quasi-continuum forcing functions while  $\mathbf{f}'$  represents the point forces associated with the point defects. These point forces are obtained via inter-atomic potentials as explained in section 2.3.

**Remark 2.2:** The mathematical conditions on the split of (2.9) into (2.10) and (2.11) for the case where the underlying equation (2.1) is nonlinear are discussed in Masud and Franca [35].

It is important to note that if we sum (2.10) and (2.11), we recover equation (2.9). Equation (2.10) is driven by the meso-to-micro force terms  $\tilde{\mathbf{f}}$  and it yields solution fields  $\tilde{\mathbf{u}}_{\tilde{\mathbf{f}}}$  and  $\mathbf{u}'_{\tilde{\mathbf{f}}}$ . Likewise, equation (2.11) is driven by micro-to-nano force terms  $\mathbf{f}'$  and it yields the solution fields  $\tilde{\mathbf{u}}_{\mathbf{f}'}$  and  $\mathbf{u}'_{\mathbf{f}'}$  that are meso-to-micro and micro-to-nano fields, respectively. We now split the *meso-micro scale problem* and the *micro-nano scale problem* into sub-system 1 and sub-system 2, respectively.

Sub-system 1: Employing the linearity of the weighting function slot in (2.10) and (2.11) we get the following two problems for the coarse or the meso-to-micro scales:

$$\left( \tilde{\mathbf{w}}, \mathcal{L} \left( \tilde{\mathbf{u}}_{\mathbf{f}'} + \mathbf{u}'_{\mathbf{f}'} \right) \right) = (\tilde{\mathbf{w}}, \tilde{\mathbf{f}}) \quad (2.12)$$

$$\left( \tilde{\mathbf{w}}, \mathcal{L} \left( \tilde{\mathbf{u}}_{\mathbf{f}'} + \mathbf{u}'_{\mathbf{f}'} \right) \right) = (\tilde{\mathbf{w}}, \mathbf{f}') \quad (2.13)$$



Sub-system 2: Similarly, from (2.10) and (2.11) we get two problems for the fine or the micro-to-nano scales:

$$\left( \mathbf{w}', \mathcal{L} \left( \tilde{\mathbf{u}}_{\tilde{\mathbf{f}}} + \mathbf{u}'_{\tilde{\mathbf{f}}} \right) \right) = \left( \mathbf{w}', \tilde{\mathbf{f}} \right) \quad (2.14)$$

$$\left( \mathbf{w}', \mathcal{L} \left( \tilde{\mathbf{u}}_{\mathbf{f}'} + \mathbf{u}'_{\mathbf{f}'} \right) \right) = \left( \mathbf{w}', \mathbf{f}' \right) \quad (2.15)$$

The key idea at this point is to solve the sub-system 2 locally so as to extract the fine scale solution components  $\mathbf{u}'_{\tilde{\mathbf{f}}}$  and  $\mathbf{u}'_{\mathbf{f}'}$ . These components can then be substituted in the sub-system 1, thereby eliminating the fine scales, yet retaining their effects. As presented in Masud and Franca [35], the solution of (2.14) when substituted in (2.12) leads to the following multiscale form of the variational problem where the fine-scale solution induced by the fine-scale forcing function is mathematically embedded in the corresponding coarse-scale problem.

$$\left( \tilde{\mathbf{w}}, \mathcal{L} \tilde{\mathbf{u}}_{\tilde{\mathbf{f}}} \right) + \left( \mathcal{L}^* \tilde{\mathbf{w}}, -\tau_1 \mathcal{L} \tilde{\mathbf{u}}_{\tilde{\mathbf{f}}} \right) = \left( \tilde{\mathbf{w}}, \tilde{\mathbf{f}} \right) - \left( \mathcal{L}^* \tilde{\mathbf{w}}, \tau_1 \tilde{\mathbf{f}} \right) \quad (2.16)$$

where  $\mathcal{L}^*$  is the adjoint operator. The boundary term is annihilated due to the assumption of fine-scales becoming zero at the inter-element boundaries, i.e.,  $\mathbf{u}'_{\tilde{\mathbf{f}}} = \mathbf{0}$  on  $\mathbf{\Gamma}'$ . The second term on the left hand side in (2.16) is the multiscale/stabilization term and is a function of the residual of the resolvable scales, i.e., function of the residual of coarse scales. Consequently, equation (2.16) gives rise to a stabilized form for the subproblem which is driven by the meso-to-micro force terms  $\tilde{\mathbf{f}}$ , and it will be used to model the defect free nanostructures.

Likewise we can take equation (2.15), which is the fine-scale problem driven by the fine-scale forcing functions and extract  $\mathbf{u}'_{\mathbf{f}'}$  via analytical or numerical methods. The functional form of  $\mathbf{u}'_{\mathbf{f}'}$  can then be substituted in the corresponding coarse-scale problem given by equation (2.13).

This results in the following variational form that is driven by the micro-to-nano force terms  $\mathbf{f}'$ , and it will be used to model the fine scale fields around the defects in nanostructures.

$$(\tilde{\mathbf{w}}, \mathcal{L}\tilde{\mathbf{u}}_{\mathbf{f}'}) + (\mathcal{L}^*\tilde{\mathbf{w}} - \tau_2\mathcal{L}\tilde{\mathbf{u}}_{\mathbf{f}'}) = (\tilde{\mathbf{w}}, \mathbf{f}') - (\mathcal{L}^*\tilde{\mathbf{w}}, \tau_2\mathbf{f}') \quad (2.17)$$

It is important to realize that the solution of (2.17) gives  $\tilde{\mathbf{u}}_{\mathbf{f}'}$  which is the coarse scale component of the solution field that arises because of the micro-to-nano force terms  $\mathbf{f}'$ .

**Remark 2.3:** *Equations (2.16) and (2.17) present a system of two equations that yield the scale dependent solutions to the governing equation that is driven by scale dependent forcing functions, respectively.*

**Remark 2.4:** *The proposed method provides a framework for bridging the scales in computational micro- and nanomechanics. In this context  $\mathbf{u}'_{\tilde{\mathbf{f}}}$  and  $\tilde{\mathbf{u}}_{\mathbf{f}'}$  are the bridging scales as they transfer information from one scale level to the other.*

### 2.1.2 Main points of the multiscale framework

This section summarizes the important aspects of the proposed framework for computational micro- and nanomechanics.

1. From (2.14) we obtain  $\mathbf{u}'_{\tilde{\mathbf{f}}}$  which when substituted in (2.12) gives rise to the variational equation (2.16) that yields a multiscale/stabilized form for  $\tilde{\mathbf{u}}_{\tilde{\mathbf{f}}}$ . This equation furnishes the solution  $\tilde{\mathbf{u}}_{\tilde{\mathbf{f}}}$  where the effects of the bridging scale  $\mathbf{u}'_{\tilde{\mathbf{f}}}$  that arises because of meso-to-micro force terms  $\tilde{\mathbf{f}}$  are mathematically embedded.
2. From (2.15) we obtain  $\mathbf{u}'_{\mathbf{f}'}$  which is the fine scale solution induced by the fine scale forcing functions. Substituting  $\mathbf{u}'_{\mathbf{f}'}$  in (2.13) gives rise to a multiscale/stabilized form for  $\tilde{\mathbf{u}}_{\mathbf{f}'}$ .

This component of the unknown field arises because of micro-to-nano force terms  $\mathbf{f}'$ , and plays the role of bridging scales in our framework.

3. The total solution to the problem is obtained via the principal of superposition.

$$\tilde{\mathbf{u}} = \tilde{\mathbf{u}}_{\tilde{\mathbf{f}}} + \tilde{\mathbf{u}}_{\mathbf{f}'} \quad (2.18)$$

For the case of nonlinear problems one can employ the Lagrange multiplier method for overlapping solutions, proposed by Belytschko *et al.* [11].

***Remark 2.5:*** Problem described by equation (2.17) can be solved over a smaller sub-domain  $\Omega_{sub} \subseteq \Omega$  by defining a representative domain or unit cell with periodic Neumann boundary conditions. Consequently, the cost of solving (2.17) around the point defects can be reduced substantially.

## 2.2 Atomic Scale Parameter Dependent Material Properties of Nanotubes

In the quasi-continuum modeling of defect-free nanostructures (2.16), interatomic interactions are incorporated into nanoscale based material moduli. These moduli are defined through internal variables that are functions of changes in bond lengths and bond angles and therefore depend on the local atomic configurations.

### 2.2.1 Molecular mechanics model

In general materials are modeled either via phenomenological/continuum models or quantum/molecular mechanics models. The latter includes classical molecular dynamics and ab initio methods. From a computational viewpoint, molecular mechanics and/or quantum me-

chanics models are expensive to be carried out on nanotubes where length is of the order of micrometers. On the other hand continuum mechanics models do not take into account changes in structure at the molecular level of the materials and therefore cannot precisely model vacancy defects or Stone-Wales transformations.

From molecular mechanics perspective, the nanosystem energy can be written as

$$U = U_\rho + U_\theta + U_\varphi + U_\Omega + U_{vdw} + U_{es} \quad (2.19)$$

where  $U_\rho$  is the bond stretch energy,  $U_\theta$  is the energy due to bond angle bending,  $U_\varphi$  is the inversion energy,  $U_\Omega$  is the torsional energy,  $U_{vdw}$  represents the Van der Waals energy, and  $U_{es}$  is the electrostatic energy. For the axial deformations in graphene sheets and carbon nanotubes a stick-spiral model wherein the system energy is based on nuclear positions has been presented by Chang and Gao [3]. We follow [3] and consider the bond stretch energy  $U_\rho$  and bond angle bending energy  $U_\theta$  in the molecular mechanics model, and ignore the other energy contributions. Consequently, (2.19) is reduced to the following equation.

$$U(\Delta r, \Delta \theta) = U_\rho(\Delta r) + U_\theta(\Delta \theta) \quad (2.20)$$

The functional forms of the bond stretch energy and bond angle rotation energy that are considered in this work are given by the modified Morse potentials presented in [10] and are written as follows:

$$U_\rho(\Delta r) = D_e \left\{ \left[ 1 - e^{-\beta \Delta r} \right]^2 - 1 \right\} \quad (2.21)$$

$$U_\theta(\Delta \theta) = \frac{1}{2} K_\theta (\Delta \theta)^2 \left[ 1 + K_{sextic} (\Delta \theta)^4 \right] \quad (2.22)$$

where  $\Delta r$  and  $\Delta\theta$  are the changes in the bond-length and the bond-angle, respectively. The various constants in equations (2.21) and (2.22) are given in [10]:  $D_e = 0.6031 \text{ nN.nm}$ ,  $K_{sextic} = 0.754 \text{ rad}^{-4}$ ,  $\beta = 26.25 \text{ nm}^{-1}$ ,  $K_\theta = 1.42 \text{ nN.nm/rad}^2$ .

By differentiating the energy equations (2.21) and (2.22) with respect to  $\Delta r$  and  $\Delta\theta$ , one obtains the force-stretch and moment angle-variation relations, respectively.

$$F(\Delta r) = 2\beta D_e \left(1 - e^{-\beta\Delta r}\right) e^{-\beta\Delta r} \quad (2.23)$$

$$M(\Delta\theta) = k_\theta \Delta\theta \left[1 + 3k_{sextic}(\Delta\theta)^4\right] \quad (2.24)$$

**Remark 2.6:** *One can consider other functional forms of the bond stretch energy and bond angle rotation energy (see e.g., [15–19]) in the stick-spiral model that is used in conjunction with the multiscale framework proposed here.*

### 2.2.2 The stick-spiral model

This section describes the stick spiral model by Chang and Gao [3] that is derived based on the molecular mechanics model for carbon nanotubes. Employing kinematic considerations, this model provides relations between axial force  $f$ , axial-strain  $\varepsilon$ , and lateral strain  $\varepsilon'$  in terms of the changes in bond-lengths and bond-angles. We have employed this model to extract bond-length and bond-angle dependent mechanical material properties, where the changes in the bond lengths and bond angles are obtained from the converged strain fields during nonlinear calculations of mechanically deforming nanotubes. For clarity of presentation, we briefly outline

the salient features of the stick-spiral model, followed by the procedure how these nanoscale based mechanical properties are employed in the proposed multiscale computational framework.

Figure 1 presents four carbon atoms that are connected via three interatomic bonds i.e., a typical unit that repeats itself to yield hexagonal patterns in carbon nanotubes and produces graphene sheets in a planar configuration. From a kinematic viewpoint, an externally applied axial force  $f$  results in changes in the bond lengths and bond angles till the new stretched configuration comes in a state of self equilibrium. Our objective is to find these equilibrated bond lengths and angles, and we use the stick-spiral model of [3] that provides a set of analytical equations that relate axial force with axial and lateral strain via the changes in bond-lengths and bond-angles.

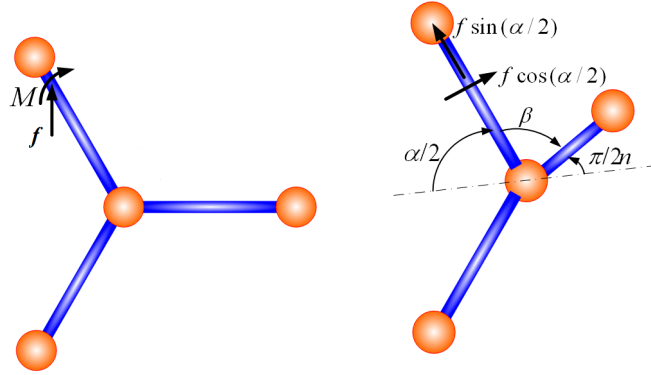


Figure 1. Schematic force and moment balance diagram for a typical pattern of four carbon atoms connected via three bond lengths. Localized strains are supposed to be homogeneous at a given point though they may change from point to point in the domain (see [3] for details).

### 2.2.2.1 Equilibrium relations

As shown in Figure 1, for any pair of carbon atoms, a component of force  $f$  acts along the line connecting the two atoms and a component is orthogonal to it. The force component that acts along the bond length results in stretching the bond and the component that is orthogonal results in changing the bond angle. Based on these kinematic considerations, Chang and Gao [3] present a stick-spiral model that gives force-equilibrium relations and the moment-equilibrium relations for the armchair nanotubes  $(n,n)$  and zigzag nanotubes  $(n,0)$ . For sake of completeness of discussion, these relations are listed as follows:

Armchair nanotubes  $(n,n)$ :

$$f \sin(\alpha/2) = F(\Delta r) \text{ (Force equilibrium)} \quad (2.25)$$

$$f(r/2) \cos(\alpha/2) = M(\Delta\alpha) + M(\Delta\beta) \cos(\phi) \text{ (Moment equilibrium)} \quad (2.26)$$

Zigzag nanotubes  $(n,0)$ :

$$f \cos(\pi - \alpha) = F(\Delta r) \text{ (Force equilibrium)} \quad (2.27)$$

$$f(r/2) \sin(\pi - \alpha) = M(\Delta\alpha) + M(\Delta\beta) \cos(\phi) \text{ (Moment equilibrium)} \quad (2.28)$$

### 2.2.2.2 Kinematic relations

From the stick spiral model for armchair and zigzag nanotubes the changes in bond-length and bond-angle are related to the axial strain via the following expressions.

Armchair nanotubes  $(n,n)$ :

$$\varepsilon = [\Delta r \sin(\alpha/2) + (r/2) \cos(\alpha/2) \Delta \alpha] / [r \sin(\alpha/2)] \quad (2.29)$$

where  $\alpha = 2\pi/3$  and  $\beta = \pi - \arccos[0.5 \cos(\pi/(2n))]$ .

Zigzag nanotubes  $(n,0)$ :

$$\varepsilon = [2\Delta r / \cos(\pi - \alpha) + \Delta r \cos(\pi - \alpha) + r \sin(\pi - \alpha) \Delta \alpha] / [r [1 + \cos(\pi - \alpha)]] \quad (2.30)$$

where  $\alpha = 2\pi/3$  and  $\beta = \pi - \arccos[0.5 \cos(\pi/(2n))]$ .

### 2.2.3 Extracting the quasi-continuum mechanical properties for CNTs

Substituting the force-stretch relation (2.23) and moment angle-variation relation (2.24) in the force equilibrium and moment equilibrium relations from section 2.2.2.1 we get two equations in terms of axial force  $f$ . Substituting for  $f$  from one into the other gives rise to one nonlinear equation in terms of the changes in bond-length  $\Delta r$  and bond-angle  $\Delta \theta$ , which are still unknowns. In order to solve the two unknowns  $\Delta r$  and  $\Delta \theta$ , we need one more equation. This equation is provided by the kinematic relations in the stick-spiral model in terms of the given applied axial strain  $\varepsilon$  and the kinematic quantities  $\Delta r$  and  $\Delta \theta$ , as presented for the armchair and the zigzag nanotubes in section 2.2.2.2. Now solving the two equations in a *self consistent fashion* yields the equilibrated values for  $\Delta r$  and  $\Delta \theta$ . These values are then used to extract the quasi-continuum properties of the defect-free nanotubes as follows:

Armchair nanotubes  $(n,n)$ :



Using  $\Delta r$  in the force-equilibrium relation (2.25) we get axial force  $f$  that yields axial stress  $\sigma$  defined as

$$\sigma = f / (r t [1 + \cos(\alpha/2)]) \quad (2.31)$$

where  $t = 0.34$  nm is the interlayer spacing in graphite. The lateral strain  $\varepsilon'$  for the armchair CNTs is given by the stick-spiral model as:

$$\varepsilon' = (\Delta r \cos(\alpha/2) - r/2 \sin(\alpha/2) \Delta \alpha) / (r [1 + \cos(\alpha/2)]) \quad (2.32)$$

Zigzag nanotubes  $(n,0)$ :

Using  $\Delta r$  in the force-equilibrium relation (2.27) we get axial force  $f$  that yields axial stress  $\sigma$  defined as

$$\sigma = f / (r t \sin(\pi - \alpha)) \quad (2.33)$$

The lateral strain  $\varepsilon'$  for the zigzag CNTs is given by the stick-spiral model as:

$$\varepsilon' = (\Delta r \sin(\pi - \alpha) - r \cos(\pi - \alpha) \Delta \alpha) / (r \sin(\pi - \alpha)) \quad (2.34)$$

Once the stress and lateral strain are evaluated via the stick-spiral model, the scale-dependent mechanical material properties of Young's modulus and Poisson's ratio are obtained as:

$$\text{Young's Modulus : } E = \sigma / \varepsilon \quad (2.35)$$

$$\text{Poisson's Ratio : } \nu = -\varepsilon' / \varepsilon \quad (2.36)$$

**Remark 2.7:** *The procedure presented above is repeated at every step and for every integration point in an element, and it results in continuous updating of the mechanical parameters that are then used in the quasi-continuum model given in equation (2.16).*

### 2.2.3.1 Procedural outline for extracting nanoscale dependent properties

This section provides a summary of the procedure described in Sections 2.2.1-2.2.3. Once the converged displacement field is attained that yields converged strains, the next step is to extract the changes in bond-lengths and bond-angles corresponding to the new equilibrated state. The stick spiral model of Chang and Gao [3] provides moment equilibrium and force equilibrium equations, and based on kinematic considerations it also provides a relation between the longitudinal strain and the changes in bond-lengths and bond-angles. We employ interatomic potentials in these equations and find the equilibrated bond-lengths and bond-angles. This is done as follows (say for the armchair nanotubes):

1. Substituting the force-stretch relation (2.23) and the moment-angle variation relation (2.24) in the force equilibrium relation (2.25) and the moment equilibrium relation (2.26) yields two equations in terms of axial-force/bond  $f$ . Eliminating  $f$  via substitution from one of these equations into another yields a nonlinear relation between  $\Delta r$  and  $\Delta\alpha$ .
2. Kinematic considerations of the stick-spiral model of Chang and Gao [3] yield a relation between longitudinal strain  $\varepsilon$ ,  $\Delta r$  and  $\Delta\alpha$  as describe in Section 2.2.2
3. Given the converged longitudinal strain obtained from the converged displacement fields in the non-linear calculations, one can solve the two equations in a self-consistent fashion and obtain the values of changes in bond-lengths  $\Delta r$  and bond-angles  $\Delta\alpha$ .

4. Once  $\Delta r$  and  $\Delta\alpha$  are evaluated numerically, equations (2.31) through (2.36) present the procedure to evaluate nanoscale dependent mechanical properties of nanomaterials.
5. To economize the computations, the nanoscale based elastic constants are evaluated only at the beginning of each load step because at that time level a converged strain field is available from previous load step.

***Remark 2.8:*** *The case of graphene sheet is attained in the limit as  $n \rightarrow \infty$  and the angles are  $\alpha = \beta = 2\pi/3$ . We follow the procedure outlined above to extract the scale dependent mechanical material properties that are then used in the quasi-continuum modeling of the continuously deforming graphene sheets.*

### 2.3 A Framework for Modeling Point Defects in Nanotubes

This section provides physical meanings to the additive split of the forcing function  $\mathbf{f}$  that was introduced in Section 2.1. We consider  $\tilde{\mathbf{f}}$  as the force field for the quasi-continuum model used for the defect free nanotubes and graphene sheets where the modulus of elasticity  $E$  and the Poisson's ratio  $\nu$  are calculated based on nanoscale parameters presented in Section 2.2. In order to apply the multiscale framework to the modeling of point defects in nanotubes and graphene sheets, we need to provide physical meanings to the term  $\mathbf{f}'$  and then describe a method to derive  $\mathbf{f}'$ .

Localized defects appear in the form of pentagons or heptagons embedded in regular hexagonal pattern in CNTs and graphene sheets. The local bond lengths and bond angles around defects are therefore different from that in the defect free region in its ground state. Consequently, the localized energy around the defects is higher as compared to the energy in the

defect free region. In our multiscale framework presented in (2.9),  $\mathbf{f}'$  represents the force field corresponding to the excess localized energy around the defect that helps maintain the surrounding atoms in their new equilibrated state with associated bond lengths and bond angles. This fine scale force field  $\mathbf{f}'$  is employed in equation (2.11) to model the mechanical fields in the vicinity of the defects.

### 2.3.1 Formation energy of vacancy

This section presents procedure for evaluation of formation energy of defect. Figure 2 shows a schematic diagram of atoms and the bonds affected by the presence of vacancy. In our calculations we have assumed that only immediate neighboring atoms, as indicated in blue color in Figure 2, are affected by the presence of divacancy. We have employed second generation Brenner potentials for calculations of defect formation energy [19]. The assumption of using only the immediate neighboring atoms in the evolution of formation energy is reasonable when one observes that Brenner potential has a cut off of 0.2 nm, while the bond-length is 0.142 nm for unstrained nanotube. This defines the patch of atoms that contribute to the formation energy of vacancy. The size of the computational cell, which in the context of the finite element method is the element that contains the defect, can be of the order of five to ten times the patch size. Suppose there are ‘ $N$ ’ carbon atoms in the non-defective patch. We can evaluate the average stretch energy stored in a carbon-carbon bond of this system as described below.

The total energy of perfect lattice as shown in Figure 2(a) is evaluated as follows.

$$E_{non-defective} = \frac{1}{2} \sum_{i,j(i \neq j)}^N [V^R(r_{ij}) - b_{ij} V^A(r_{ij})] \quad (2.37)$$

The functions  $V^R(r_{ij})$  and  $V^A(r_{ij})$  represent all interatomic repulsions and attractions from valence electrons respectively, and are defined in Brenner *et al.* [19].  $N$  is the number of atoms in the perfect lattice.

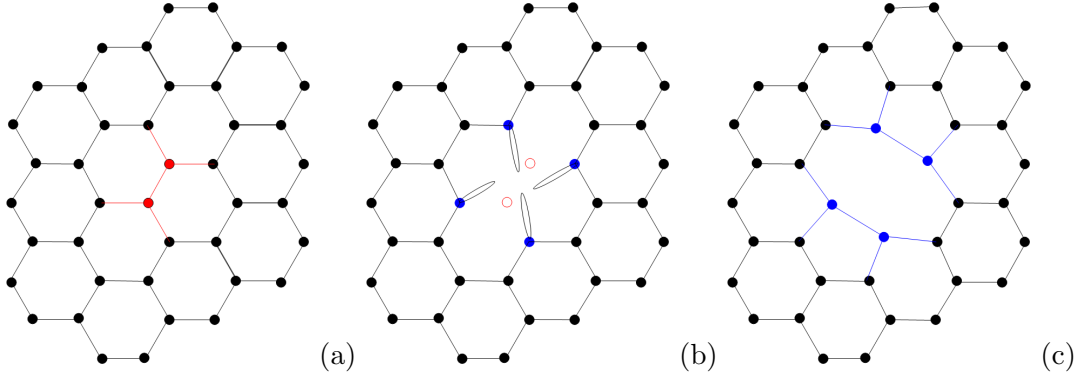


Figure 2. Relaxation of atoms around the defect. (a) Hexagonal pattern without defect, divacancy sites shown in red (b) Configuration of atoms with divacancy and dangling bonds.

Immediate neighboring atoms, shown in blue are allowed to relax. (c) Relaxation and reconfiguration of atoms around divacancy.

The total energy of the lattice with divacancy is evaluated by allowing neighboring atoms around vacancy to relax. This is achieved through minimization of energy of this lattice with respect to varying lattice positions of immediate neighboring atoms. Figures 2(b) and 2(c) show the relaxation and reconfiguration of atoms around divacancy.

The formation energy is defined as follows.

$$E_{vacancy}^{formation} = E_{defective}^{relaxed} - \frac{N-2}{N} E_{non-defective} \quad (2.38)$$

where  $E_{defective}^{relaxed}$  is the total energy of the defective lattice after allowing relaxation of neighboring atoms. The average stretch energy in defective lattice is obtained as

$$U_{\rho}^{defective} = U_{\rho}^{non-defective}(\Delta r) + \frac{E_{vacancy}^{formation}}{M} \quad (2.39)$$

where  $M$  is the total number of bonds in the defective lattice.

We reconsider (2.20) and modify the stretch energy of the defect free material with the energy given by (2.39). Taking derivative with respect to the change in bond length  $\Delta r$  we get an expression for the homogenized force-stretch relation:

$$\begin{aligned} F(\Delta b)_{defective} &= \partial U_{\rho}^{defective} / \partial \Delta r \\ &= F(\Delta r) + \frac{F_{formation}}{M} \end{aligned} \quad (2.40)$$

where

$$\begin{aligned} F_{formation} &= \partial E_{vacancy}^{formation} / \partial \Delta r \\ &= \partial E_{defective}^{relaxed} / \partial \Delta r - \frac{(N-2)}{N} (\partial E_{non-defective} / \partial \Delta r) \end{aligned} \quad (2.41)$$

Once the updated force-stretch relation is obtained via (2.40), we employ the procedure outlined in Section 2.2 to extract the nanoscale based quasi-continuum mechanical material properties around the point defects in the nanotubes. These material parameters are then used in the variational problem driven by  $\mathbf{f}'$ .

**Remark 2.9:** *In order to keep the model and associated calculations simple the defect is assumed to be frozen during the course of deformation of CNTs, i.e., further interatomic bonds do not appear nor do the existing bonds break at or around the current defect.*

**Remark 2.10:** *It is important to note that the scale dependent nanomechanical material properties are evaluated based on the new equilibrated bond lengths and bond angles around the point defect. These values are different from the equilibrated bond lengths and angles away from the defect.*

**Remark 2.11:** *Similar computations can be made for defects like Stone-Wales transformations. Zhou et al. [27] gives a simple empirical formula to evaluate Stone-Wales formation energy in case of carbon nanotubes. Li et al. [28] have computed formation energies of Stone-Wales defect through first principle methods in case of graphite. The computed formation energy can be used to extract material properties as outlined in the procedure described above.*

### 2.3.2 Evaluation of the force component $\mathbf{f}'$

In the multiscale framework presented in equation (2.9),  $\mathbf{f}'$  represents the force field corresponding to the excess localized energy around the defect that maintains the surrounding atoms in their new equilibrated state with new bond lengths and bond angles as shown in Figure 2. We write the minimization problem of the relative energy in a weak form and the fine scale force field  $\mathbf{f}'$  is extracted by solving a linearized variational equation at each load step.

$$(w_i, f'_i) = (w_{i,j}, \sigma_{ij}^{defective}) - (w_{i,j}, \sigma_{ij}^{non-defective}) \quad (2.42)$$

where  $\sigma^{defective}$  represents the stress field of the defective patch and  $\sigma^{non-defective}$  represents the stress field associated with the non-defective patch. Figure 3 shows the schematic diagram of the finite element mesh indicating the coarse element that contains the defect. A sub-mesh is generated over this coarse mesh as shown in Fig. 3 and the sub intervals of this refined mesh are termed as computational cells.

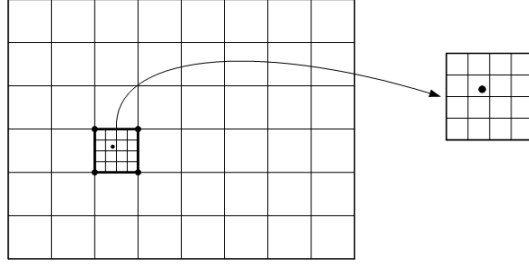


Figure 3. Schematic diagram of finite element mesh indicating the element that possesses the defective patch. Computational cell is defined as a subinterval of the refined mesh that overlays the element containing defect. In this context element of the coarse mesh that contains defect becomes a super-element. Point defect in the cell is indicated by the dot.

Weak solution to equation (2.42) in the computational cell containing defect yields  $\mathbf{f}'$ . The contribution to  $\mathbf{f}'$  from other cells in the sub-mesh is zero because these cells do not contain the defect. It is reasonable to assume that the effect of  $\mathbf{f}'$  is localized around the point defect. Consequently equation (2.17) is solved on the refined sub-mesh that is generated over the element of the coarse mesh containing the point defect, and is termed as the super-element (see Figure 3).

### 2.3.3 Salient features of the formulation for modeling defects in nanostructures

1. The quasi-continuum model has nano length-scales built in it because of the dependence of the modulus of elasticity  $E(r, \theta)$  and the Poisson's ratio  $\nu(r, \theta)$  on the inter-atomic bond lengths  $r$  and bond angles  $\theta$ .
2. The local defects in the graphene sheet induce an atomic-scale (fine scale) force field which is indicated by  $\mathbf{f}'$ . This atomic-scale force field is obtained through equation (2.42)



where formation energy of the vacancy embedded with interatomic potentials for defective and non-defective nanostructure has been employed to define  $\sigma^{defective}$  and  $\sigma^{non-defective}$ . This fine scale force field drives the problem for the localized displacement field around defects in the nanostructure.

3. The case where problems driven by  $\tilde{\mathbf{f}}$  and  $\mathbf{f}'$  given in equations (2.16) and (2.17) respectively are linear problems, the total solution around defects can be obtained via principle of superposition as

$$\tilde{\mathbf{u}} = \tilde{\mathbf{u}}_{\tilde{\mathbf{f}}} + \tilde{\mathbf{u}}_{\mathbf{f}'} \quad (2.43)$$

4. The case where problems driven by  $\tilde{\mathbf{f}}$  and  $\mathbf{f}'$  are nonlinear, Lagrange multiplier methods for overlapping solutions can be employed as presented in Belytschko *et al.* [11].
5. The case where body force  $\tilde{\mathbf{f}} = \mathbf{0}$ , the problem for the defect free nanostructure (graphene sheet or nanotubes) is driven by edge traction and/or the prescribed edge displacement fields.
6. The defective inter-atomic bond lengths are on the order of nano-meters (see Figure 2).

The defective patch of atoms that contains the point defect and is used to evaluate energy associated with  $\mathbf{f}'$  via (2.39) – (2.41) is typically spread over six to eight bond diameters. The size of the computational cell (i.e., sub-interval of the sub mesh) can be taken equal to five to ten times the patch size (see Fig. 3). Employing a refined sub-mesh, the super-element that contains the cells can be one to two orders of magnitude larger than the representative computational cell that contains the point defect. Depending on the size of the global mesh, which can be another one to two orders of magnitude larger than

the element on which the refined sub-mesh is created, one can scale up from the nanometer  $10^{-9}$  m range to a specimen size that lies between micro-scale  $10^{-6}$  m and meso-scale  $10^{-4}$  m.

7. Defects in the nanostructure are explicitly represented via the interatomic potentials. For the case when there are no defects in the lattice,  $\mathbf{f}' = \mathbf{0}$  and the solution given by  $\tilde{\mathbf{u}}_{\tilde{\mathbf{f}}}$  is the total solution for the defect-free nanostructure. This is a very important attribute of the proposed computational framework and ensures that the proposed method is a self-consistent method.

## 2.4 Numerical Results

The multiscale framework presented in Section 2.1 leads to a hierarchical finite element method that has been implemented using four-node isoparametric elements [47, 48]. As presented in Section 2.2, the mechanical material properties are evaluated at the integration points via a set of internal variables that are functions of interatomic potentials. These interatomic potentials are functions of the changes in the bond lengths and bond angles that occur because of the local state of deformation. The underlying idea is based on internal variable formalism for the nanoscale based mechanical material properties and a consistent updating of material properties concurrently feeds information from the molecular scales into the quasi-continuum equations. The resulting nonlinear finite element method is used for studying the mechanical response of defect-free and defective carbon nanotubes.

#### 2.4.1 Mechanical response of defect-free nanotubes

This section presents the simulated mechanical material properties of zigzag and armchair tubes. Two types of interatomic potentials have been investigated by incorporating them in the nano-structural model: modified Morse potential [10] and the Tersoff-Brenner potential [19].

Figure 4 presents the Young's modulus for the nanotubes as a function of the changes in the tube diameter. Open symbols represent the response of armchair nanotubes and solid symbols represent the response of zigzag nanotubes. Both modified Morse as well as the Brenner potentials have been employed to extract the modulus of elasticity of CNTs. The value of Young's modulus as predicted by using Brenner potential is approximately 5% higher than that predicted by Morse potential. For each of these cases the simulated Young's modulus is slightly higher for the armchair CNTs than that for the zigzag CNTs of the same diameter.

Computed results are also compared with published literature where results from Goze *et al.* [20] are an upper bound and results from Popov *et al.* [21] are a lower bound to the present calculations. The predicted mechanical response lies in the general range of the expected mechanical material properties for the various types of CNTs [49, 50]. Figure 5 presents the Poisson's ratio for the two types of nanotubes as a function of change in the tube diameter. Once again modified Morse as well as the Brenner potentials have been employed and a good agreement has been attained with the published results.

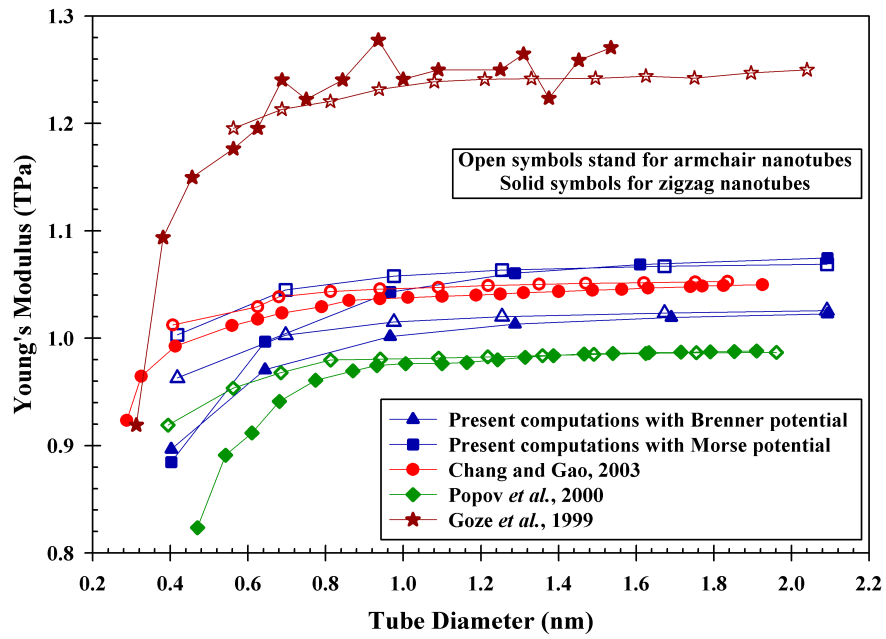


Figure 4. Young's modulus for non-defective nanotubes

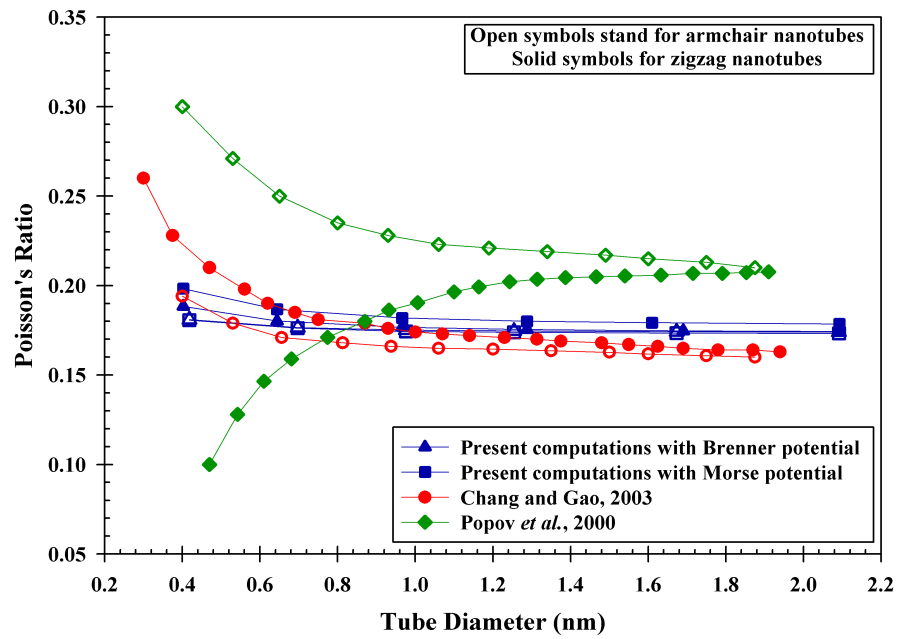


Figure 5. Poisson's ratio for non-defective nanotubes

### 2.4.2 Mechanical response of nanotubes with topographical defects

The proposed multiscale framework is also applied to the modeling of mechanical response of carbon nanotubes with topographical defects such as vacancies (see eg. [10,27,51]). We consider that the defects arise because of missing atoms that result in a change in the hexagonal pattern in graphene sheets and nanotubes.

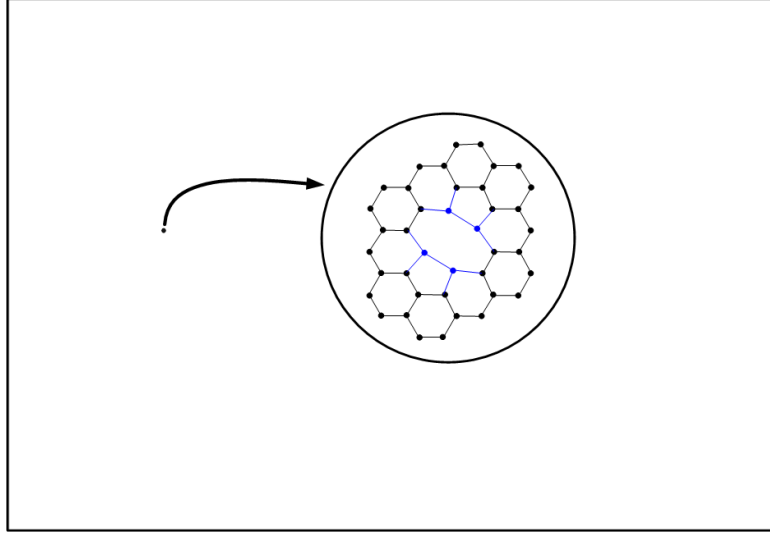


Figure 6. A schematic diagram of frozen divacancy defect

These defects stay frozen during the mechanical loading of the CNT, i.e., further defects do not appear as a function of deformation. Figure 6 shows a schematic diagram of a defect due to divacancy that is assumed to exist in the initial configuration of the CNT and this defect persists through the deformation process. Figures 7 and 8 present the stress-strain plots for the non-defective and defective (5,5) armchair tubes, respectively. Once again results

are compared with various theoretical models presented in [51], primarily based on quantum mechanical and molecular dynamic models. The present model predicts the nano-stress-strain relation with great accuracy. It is important to note that these results have been obtained on a single processor desktop computer at a fraction of the computational effort as compared with the quantum mechanical and molecular dynamical models.

Figures 9 and 10 present Young's modulus as a function of increasing deformation represented in the form of increasing strain for the non-defective and defective (5,5) armchair CNTs. These calculations were also carried out on a single processor desktop computer. Once again the multiscale model predicts mechanical properties within the envelope provided by the DFT and the PM3 models reported in [51].

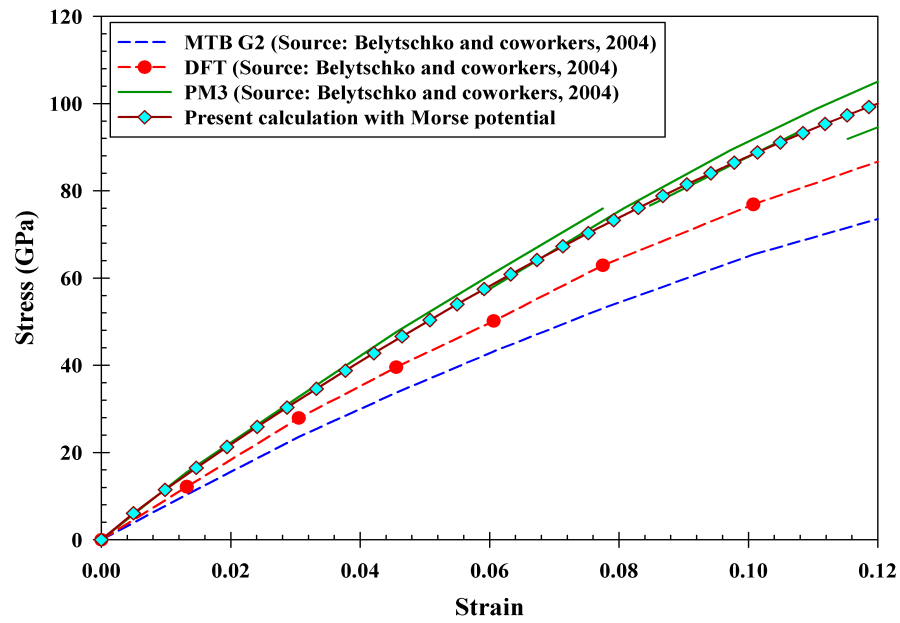


Figure 7. Stress strain response for non-defective nanotube

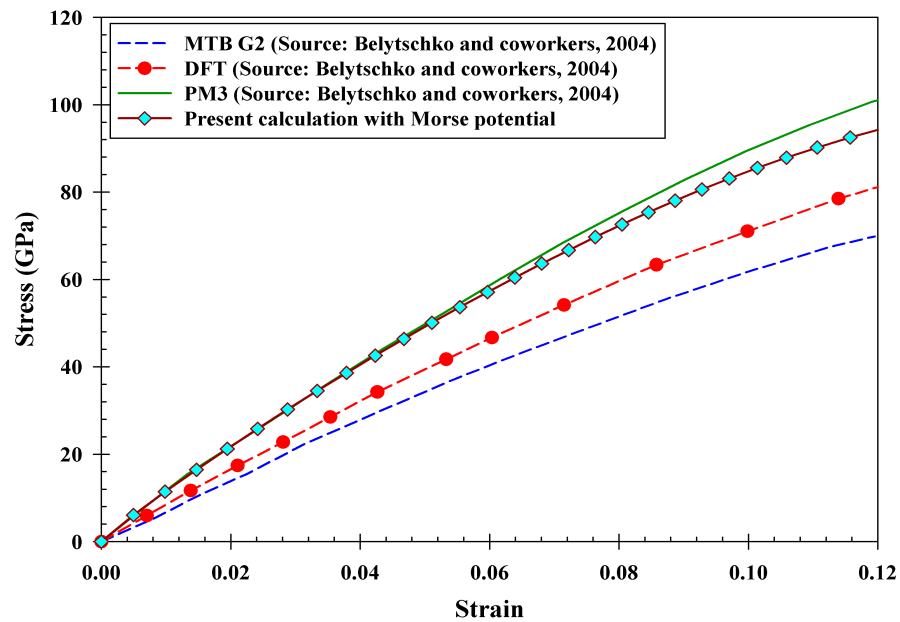


Figure 8. Stress strain response of defective nanotube

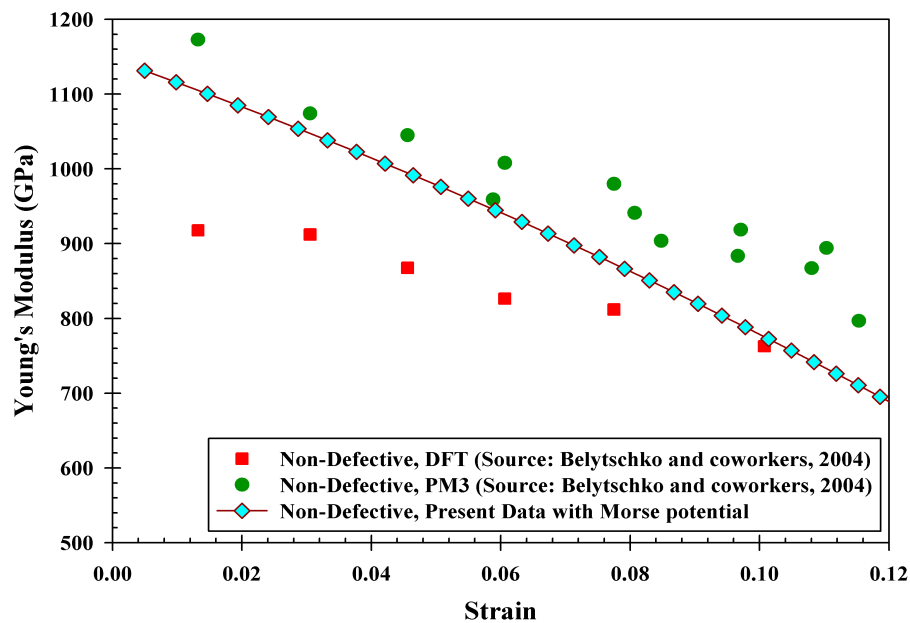


Figure 9. Young's modulus as function of strain for non-defective nanotubes

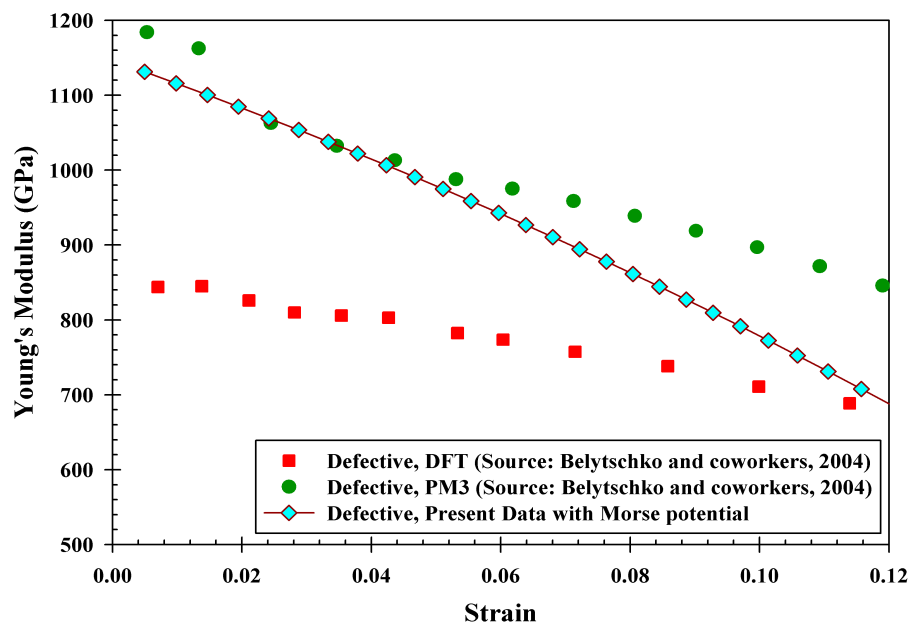


Figure 10. Young's modulus as function of strain for defective nanotubes



### 3 STABILIZED FINITE ELEMENT METHOD FOR SWE

#### 3.1 The Schrödinger Wave Equation

Let  $\Omega \subset \mathbb{R}^{n_{sd}}$  be an open bounded region with piece wise smooth boundary  $\Gamma$ . The number of space dimensions  $n_{sd} = 3$ . The Schrödinger wave equation can be written as

$$-\kappa \Delta v(\mathbf{x}) - i2\kappa \mathbf{k} \bullet \nabla v(\mathbf{x}) + \kappa k^2 v(\mathbf{x}) + V(\mathbf{x}) v(\mathbf{x}) = \varepsilon(\mathbf{k}) v(\mathbf{x}) \quad \text{in } \Omega \quad (3.1)$$

Solution of the SWE satisfies Bloch's theorem of periodicity of the wave function. From the periodicity condition, the boundary conditions are taken to be of the form.

$$v(\mathbf{x}) = v(\mathbf{x} + \mathbf{R}) \quad \text{on } \Gamma \quad (3.2)$$

$$\mathbf{n} \cdot \nabla v(\mathbf{x}) = \mathbf{n} \cdot \nabla v(\mathbf{x} + \mathbf{R}) \quad \text{on } \Gamma \quad (3.3)$$

where  $v(\mathbf{x})$  is the complex valued cell periodic function or the unknown complex scalar field, namely the wave function (or the eigenfunction),  $\mathbf{x}$  represents position vector,  $\mathbf{n}$  represents outward unit normal vector to the boundary  $\Gamma$  of a unit cell,  $V(\mathbf{x})$  is the electronic potential or the potential energy of an electron in a charge density  $\rho(\mathbf{x})$  at the position  $\mathbf{x}$  and is considered periodic over a unit cell, and  $i$  is the imaginary unit.  $\varepsilon(\mathbf{k})$  is the eigen-energy associated with

the particle as a function of wavevector (position vector in reciprocal space)  $\mathbf{k}$ .  $\mathbf{R}$  refers to the lattice vectors of the unit cell, and  $\kappa = \frac{\hbar^2}{2m}$  and  $\hbar = \frac{h}{2\pi}$  are constants, where  $h$  is the Planck's constant and  $m$  is the effective mass of electron.

***Remark 3.1:*** *The values of  $V(\mathbf{x})$  and  $v(\mathbf{x})$  in a periodic solid are completely determined by their values in a single unit cell. Therefore solutions of the Schrödinger equation in a periodic solid can be reduced to their solutions in a single unit cell, subject to periodic boundary conditions consistent with Equations. (2) and (3), respectively.*

### 3.1.1 The Standard weak form

Let  $\mathcal{V} \subset H^1(\Omega^{n_{sd}}) \cap C^0(\Omega^{n_{sd}})$  denote the space of trial solutions and weighting functions for the unknown scalar field where periodicity of the boundary condition is embedded in the admissible space.

$$\mathcal{V} = \{v | v \in H^1(\Omega^{n_{sd}}), v(\mathbf{x}) = v(\mathbf{x} + \mathbf{R}) \quad \forall \mathbf{x} \in \Gamma\} \quad (3.4)$$

The standard weak form for the complex valued problem is

$$-(w, i2\kappa \mathbf{k} \bullet \nabla v) + (\nabla w, \kappa \nabla v) + (w, (\kappa k^2 + V) v) = (w, \varepsilon v) \quad (3.5)$$

where  $w$  is the weighting function for  $v$ , and  $(\bullet, \bullet) = \int_{\Omega} (\bullet) d\Omega$  i.e.,  $L_2$  product of the indicated arguments over domain  $\Omega$ . Discretization of the standard weak form gives rise to a generalized eigenvalue problem for the complex valued cell periodic function or the eigen-function  $v(\mathbf{x})$  and the associated eigen-energy  $\varepsilon(\mathbf{k})$ .

**Remark 3.2:** *Galerkin method seems to work for the present problem, however typical applications in the literature have been presented in the context of Hermite cubic functions [2, 29]. Employing lower order Lagrange shape functions in the standard Galerkin formulation results in reduced accuracy in the evaluation of higher eigenvalues in the system.*

**Remark 3.3:** *Our objective in this work is to explore numerical methods that can provide higher accuracy in the estimation of higher eigenvalues, while using lower order Lagrange shape functions on computational domains that are less dense than the grids employed for the corresponding Galerkin method.*

### 3.2 The Galerkin/Least-Square Stabilized Form

This section presents the Galerkin Least/Squares (GLS) form for the Schrödinger wave equation. GLS stabilization is a standard technique employed in computational fluid dynamics to enhance the stability of the underlying Galerkin variational formulations, that also manifests itself in terms of improved accuracy on relatively cruder discretizations. Basic idea of stabilized methods is to add a least squares form of the Euler-Lagrange equations to the standard Galerkin form presented in equation (3.5), thus strengthening the variational structure of the problem.

$$\begin{aligned}
 & (\nabla w, \kappa \nabla v) - (w, i2\kappa \mathbf{k} \bullet \nabla v) + (w, (\kappa k^2 + V - \varepsilon) v) + \\
 & \left( \begin{array}{l} (-\kappa \Delta - i2\kappa \mathbf{k} \bullet \nabla + \kappa k^2 + V) w, \\ \tau^{GLS} [(-\kappa \Delta - i2\kappa \mathbf{k} \bullet \nabla + \kappa k^2 + V - \varepsilon) v] \end{array} \right) = 0
 \end{aligned} \tag{3.6}$$

In equation (3.6) we have used the idea of Petrov-Galerkin methods and have dropped the  $\epsilon$  term in the weighting function slot of the additional stabilization term. This helps in reducing

the order of the resulting eigenvalue problem from quadratic to linear. In (3.6)  $\tau^{GLS}$  is the stabilization parameter that will be defined later.

***Remark 3.4:*** *The GLS method is shown to yield higher accuracy for many physical problems [34, 52] and in the present case it sets the stage for exploring the variational multiscale ideas for application to SWE.*

### 3.3 The Variational Multiscale Method

This section develops and explores the properties of another stabilized method that finds its roots in the Variational Multiscale method proposed by Hughes [34], and is termed as the HVM form. A basic premise of multiscale approach is to acknowledge the presence of the fine scales that may not be resolved by a given spatial discretization. We consider the bounded domain  $\Omega$  to be discretized into non-overlapping regions  $\Omega^e$  (element domains) with boundaries  $\Gamma^e$ ,  $e = 1, 2, \dots, numel$  such that  $\Omega = \bigcup_{e=1}^{numel} \bar{\Omega}^e$ . We denote the union of element interiors and element boundaries by  $\Omega'$  and  $\Gamma'$  respectively, i.e.  $\Omega' = \bigcup_{e=1}^{numel} (int)\Omega^e$  (element interiors) and  $\Gamma' = \bigcup_{e=1}^{numel} \Gamma^e$  (element boundaries). We assume an overlapping sum decomposition of the scalar field  $v(\mathbf{x})$  into coarse- or resolvable-scales and fine- or the subgrid-scales.

$$v(\mathbf{x}) = \bar{v}(\mathbf{x}) + v'(\mathbf{x}) \quad (3.7)$$

Likewise, we assume an overlapping sum decomposition of the weighting function into the coarse- and the fine-scale components, respectively.

$$w(\mathbf{x}) = \bar{w}(\mathbf{x}) + w'(\mathbf{x}) \quad (3.8)$$

We further make an assumption that the subgrid scales although non-zero within the elements, vanish identically over the element boundaries, i.e.  $v' = w' = 0$  on  $\Gamma'$ .

We now introduce the appropriate spaces of functions for the coarse- and fine-scale fields and specify direct sum decomposition on these spaces, i.e.  $v = \bar{v} \oplus v'$  where  $\bar{v}$  is the space of trial solutions and weighting functions for the coarse-scale field and is identified with the standard finite element space, while  $v'$  is the space of fine-scale functions. These spaces are subject to the restriction imposed by the stability of the formulation that requires  $\bar{v}$  and  $v'$  to be linearly independent.

### 3.3.1 The multiscale variational problem

We now substitute the trial solutions (3.7) and the weighting functions (3.8) in the standard variational form (3.5), which yields

$$\begin{aligned} & -(\bar{w} + w', i2\kappa \mathbf{k} \bullet \nabla (\bar{v} + v')) + (\nabla(\bar{w} + w'), \kappa \nabla (\bar{v} + v')) \\ & + (\bar{w} + w', (\kappa k^2 + V) (\bar{v} + v')) = (\bar{w} + w', \varepsilon (\bar{v} + v')) \end{aligned} \tag{3.9}$$

With suitable assumptions on the fine scale field (i.e., fine-scales vanish at the inter element boundaries) and employing the linearity of the weighting function slot, we can split the problem into coarse- and fine-scale parts, indicated as  $\bar{w}$  and  $w'$ , respectively.

Coarse-scale Problem  $\bar{w}$

$$\begin{aligned} & -(\bar{w}, i2\kappa \mathbf{k} \bullet \nabla (\bar{v} + v')) + (\nabla \bar{w}, \kappa \nabla (\bar{v} + v')) \\ & + (\bar{w}, (\kappa k^2 + V) (\bar{v} + v')) = (\bar{w}, \varepsilon (\bar{v} + v')) \end{aligned} \tag{3.10}$$

### Fine-scale Problem $w'$

$$\begin{aligned}
& - (w', i2\kappa \mathbf{k} \bullet \nabla (\bar{v} + v')) + (\nabla w', \kappa \nabla (\bar{v} + v')) \\
& + (w', (\kappa k^2 + V) (\bar{v} + v')) = (w', \varepsilon (\bar{v} + v'))
\end{aligned} \tag{3.11}$$

The underlying idea at this point is to solve the fine-scale problem (3.11), which is defined over the sum of element interiors, to obtain the fine scale solution  $v'$ . This solution is then substituted in the coarse-scale problem given by (3.10), thereby eliminating the fine scales, yet retaining their effect.

### **3.3.2 Solution of the fine scale problem ( $w'$ )**

Employing linearity of the solution slot in equation (3.11), applying integration by parts, and rearranging terms, the fine scale problem reduces to

$$\begin{aligned}
& - (w', i2\kappa \mathbf{k} \bullet \nabla v')_{\Omega'} + (\nabla w', \kappa \nabla v')_{\Omega'} + (w', (\kappa k^2 + V) v')_{\Omega'} \\
& - (w', \varepsilon v')_{\Omega'} = (w', i2\kappa \mathbf{k} \bullet \nabla \bar{v} + \kappa \Delta \bar{v} - (\kappa k^2 + V) \bar{v} + \varepsilon \bar{v})_{\Omega'}
\end{aligned} \tag{3.12}$$

From (3.12) one can see that the fine scale problem is driven by the residual of Euler-Lagrange equations of the coarse scales defined over the sum of element interiors. Without loss of generality, we assume that the fine scales  $v'$  and  $w'$  are represented via bubbles over element domains. i.e.,

$$v'|_{\Omega^e} = b_I^e v'_e \quad \text{on } \Omega^e \tag{3.13}$$

$$w'|_{\Omega^e} = b_2^e w'_e \quad \text{on } \Omega^e \tag{3.14}$$

where  $b_1^e$  and  $b_2^e$  represent the bubble shape functions, and  $v_e'$  and  $w_e'$  represent the coefficients for the fine-scale trial solutions and weighting functions, respectively. Substituting (3.13) and (3.14) in the fine-scale problem (3.12) we get

$$\begin{aligned} & - (b_2^e w_e', i2\kappa \mathbf{k} \bullet \nabla b_1^e v_e')_{\Omega'} + (\nabla b_2^e w_e', \kappa \nabla b_1^e v_e')_{\Omega'} + (b_2^e w_e', (\kappa k^2 + V) b_1^e v_e')_{\Omega'} \\ & - (b_2^e w_e', \varepsilon b_1^e v_e')_{\Omega'} = (b_2^e w_e', i2\kappa \mathbf{k} \bullet \nabla \bar{v} + \kappa \Delta \bar{v} - (\kappa k^2 + V) \bar{v} + \varepsilon \bar{v})_{\Omega'} \end{aligned} \quad (3.15)$$

Taking the constant coefficients  $w_e'$  and  $v_e'$  out of the integral expressions and employing arbitrariness of  $w_e'$ , we can solve for the fine-scale coefficients  $v_e'$

$$v_e' = \frac{-1 (b_2^e, (-\kappa \Delta - i2\kappa \mathbf{k} \bullet \nabla + \kappa k^2 + V - \varepsilon) \bar{v})_{\Omega'}}{[(\nabla b_2^e, \kappa \nabla b_1^e)_{\Omega'} + (b_2^e, (-i2\kappa \mathbf{k} \bullet \nabla + \kappa k^2 + V - \varepsilon) b_1^e)_{\Omega'}]} \quad (3.16)$$

We can now reconstruct the fine scale field via recourse to (3.13). In order to keep the presentation simple, and for the case where the residual of the coarse scales over element interiors can be considered constant, we can simplify fine scales  $v'(x)$  as follows:

$$v'(x) = -\tau [(-\kappa \Delta - i2\kappa \mathbf{k} \bullet \nabla + \kappa k^2 + V - \varepsilon) \bar{v}] \quad (3.17)$$

Within the context of stabilized methods  $\tau$  is defined as the stability parameter. In the derivation presented above  $\tau$  has an explicit form

$$\tau = b_1^e \int_{\Omega^e} b_2^e d\Omega \left[ (\nabla b_2^e, \kappa \nabla b_1^e)_{\Omega'} + (b_2^e, (-i2\kappa \mathbf{k} \bullet \nabla + \kappa k^2 + V - \varepsilon) b_1^e)_{\Omega'} \right]^{-1} \quad (3.18)$$

**Remark 3.5:** In our numerical calculations we have simplified the definition of  $\tau$  by setting  $\varepsilon = 0$  in equation (3.18).

**Remark 3.6:** The definition of the bubble functions completely resides in the definition of the stability parameter  $\tau^{HVM}$ . Consequently, a choice of specific bubbles only affects the value of  $\tau^{HVM}$ . Stabilization parameters that are based on element-level matrices and element-level vectors have also been used in SUPG and GLS methods [52]

### 3.3.3 The coarse scale problem ( $\bar{w}$ )

Employing linearity of the solution slot in the coarse-scale sub-problem (3.10) and applying integration by parts, one can combine  $v'$  terms as

$$\begin{aligned} & -(\bar{w}, i2\kappa \mathbf{k} \bullet \nabla \bar{v}) + (\nabla \bar{w}, \kappa \nabla \bar{v}) + (\bar{w}, (\kappa k^2 + V - \varepsilon) \bar{v}) \\ & + ((i2\kappa \mathbf{k} \bullet \nabla - \kappa \Delta + \kappa k^2 + V - \varepsilon) \bar{w}, v') = 0 \end{aligned} \tag{3.19}$$

Substituting  $v'$  from (3.17) in (3.19) yields the resulting stabilized formulation.

$$\begin{aligned} & (\nabla \bar{w}, \kappa \nabla \bar{v}) - (\bar{w}, i2\kappa \mathbf{k} \bullet \nabla \bar{v}) + (\bar{w}, (\kappa k^2 + V - \varepsilon) \bar{v}) - \\ & \left( \begin{array}{c} (-\kappa \Delta + i2\kappa \mathbf{k} \bullet \nabla + \kappa k^2 + V - \varepsilon) \bar{w}, \\ \tau [(-\kappa \Delta - i2\kappa \mathbf{k} \bullet \nabla + \kappa k^2 + V - \varepsilon) \bar{v}] \end{array} \right) = 0 \end{aligned} \tag{3.20}$$



### 3.3.4 The HVM stabilized form

The HVM stabilized form (3.20) is completely expressed in terms of the coarse or resolvable scales. Therefore, in order to keep the notation simple we drop the superposed bars and we write the resulting form as

$$\begin{aligned}
 & (\nabla w, \kappa \nabla v) - (w, i2\kappa \mathbf{k} \bullet \nabla v) + (w, (\kappa k^2 + V - \varepsilon) v) \\
 & - \left( \begin{array}{l} (-\kappa \Delta + i2\kappa \mathbf{k} \bullet \nabla + \kappa k^2 + V - \varepsilon) w, \\ \tau [(-\kappa \Delta - i2\kappa \mathbf{k} \bullet \nabla + \kappa k^2 + V - \varepsilon) v] \end{array} \right) = 0
 \end{aligned} \tag{3.21}$$

**Remark 3.7:** *The first three terms in (3.21) are the standard Galerkin terms. Fourth term has appeared due to the assumption of the existence of fine scales. This term is not present in the standard Galerkin formulation.*

**Remark 3.8:** *The sub-grid scales are proportional to the residual of the coarse scales as shown in (3.12) and (3.17), i.e., it is a residual based method and therefore satisfies consistency ab initio.*

**Remark 3.9:** *When compared with the standard Galerkin method, the multiscale approach involves additional integrals that are evaluated element wise and represent the effects of the sub-grid scales that are modeled in terms of the residuals of the coarse scales of the problem.*

**Remark 3.10:** *For numerical solution of the variational problem where the periodic Dirichlet and Neumann boundary conditions presented in equations (3.1) and (3.2) are already embedded in (3.21), we employ the procedure outlined in Pask et al. [2, 29, 30] and modify element connectivity to produce value-periodic basis functions.*

### 3.3.5 Quadratic eigenvalue problem for the HVM form

The solution procedure for HVM form (3.21) involves a quadratic eigenvalue problem described as follows.

$$(\varepsilon^2 M + \varepsilon C + \mathbf{k}) x = 0 \quad (3.22)$$

where  $M$ ,  $C$ , and  $\mathbf{k}$  are  $n \times n$  matrices,  $\varepsilon$  is the scalar eigenvalue and  $x$  is eigenvector. In order to solve this problem one has to linearize it as follows.

$$Az = \varepsilon Bz \quad (3.23)$$

where

$$A = \begin{bmatrix} 0 & I \\ -K & -C \end{bmatrix}, B = \begin{bmatrix} I & 0 \\ 0 & M \end{bmatrix}, \text{ and } z = \begin{bmatrix} x \\ \varepsilon x \end{bmatrix} \quad (3.24)$$

**Remark 3.11:** *The HVM eigenvalue problem increases the size of matrices from  $n \times n$  to  $2n \times 2n$ , which also increases the cost of computation.*

## 3.4 Numerical Examples

Figure 11 shows a family of 3-D elements that consist of 4 and 10-node tetrahedra and 8 and 27-node brick elements for the numerical solution of the problem. In the numerical tests presented in this section, the functional form of  $\tau^{GLS}$  is taken to be the same as that of  $\tau^{GLS}$  which is defined in equation (3.18). The bubble functions employed for the evaluation of  $\tau$  are at least one order higher than the functions employed for the complex valued wavefunction. Accordingly, quadratic and cubic bubble functions were used for the 8-node and 27-node brick

elements, respectively. In the case of both linear and quadratic tetrahedral elements, quadratic bubbles were used as this bubble function enriches the space of functions in both the cases.

We present the convergence study for the 3D generalized Kronig-Penney problem. The domain under consideration is a cube with electronic potential  $V(\mathbf{x})$  given by

$$V(\mathbf{x}) = V_{1D}(x) + V_{1D}(y) + V_{1D}(z) \quad \text{in } \Omega \quad (3.25)$$

where

$$V_{1D}(s) = \begin{cases} 0 & 0 \leq s < 2 \text{ a.u.} \\ 6.5 \text{ Ry} & 2 \leq s < 3 \text{ a.u.} \end{cases} \quad (3.26)$$

Figures 12 to 19 present convergence rates for the fractional error in the first, fifth and seventh eigenvalues for the Galerkin, GLS, and HVM methods with linear and quadratic shape functions at a selected, but otherwise arbitrary  $\mathbf{k}$  point. Theoretical convergence rate for the eigenvalues for linear and quadratic elements is  $\mathbf{k} + 1$ , where  $\mathbf{k}$  is the order for the interpolation of the complex valued wavefunction  $v$ . Computed rates corroborate the theoretical predictions [53]. In each of the test cases the  $L_2$  error in the computed eigenvalues is smallest for the first eigenvalue and it successively increases for the higher eigenvalues. In these test cases Galerkin solution is the least accurate for any given mesh.

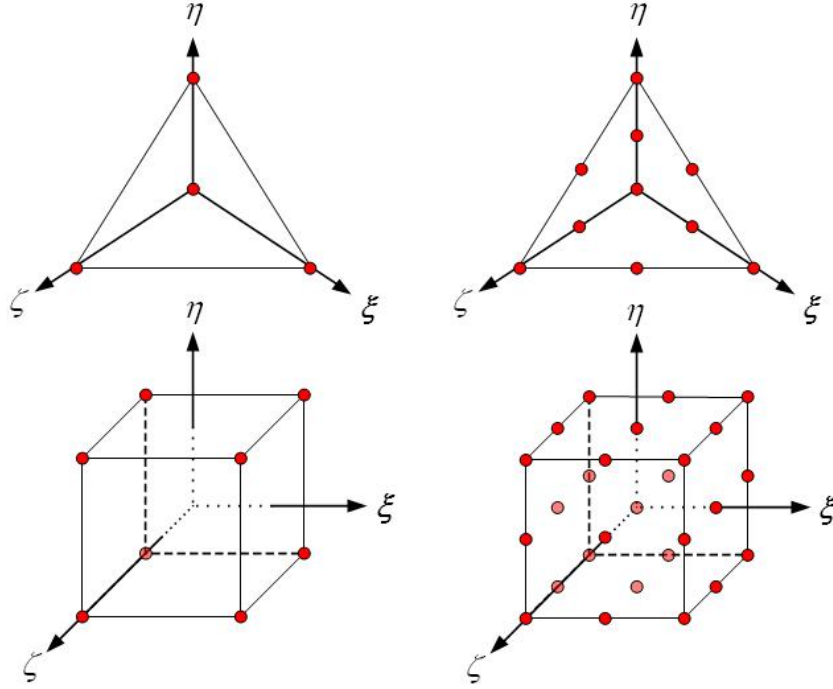


Figure 11. A family of 3-D linear and quadratic elements.

#### 3.4.1 Convergence rate results for the GLS stabilized formulation

Figures 12-15 show convergence properties for the GLS method. Meshes employed for the linear elements are composed of  $4^3$ ,  $8^3$  and  $12^3$ , while meshes employed for quadratic elements are composed of  $2^3$ ,  $4^3$  and  $6^3$  elements. Figures 12 and 13 show a quadratic convergence rate for the computed eigenvalues for linear elements, while cubic convergence rate is attained for the quadratic elements as shown in Figures 14 and 15. In all the cases although there is no increase in convergence rates for the GLS stabilized method as compared to the standard Galerkin method, the results clearly show that the GLS eigenvalues are more accurate than those obtained via the standard Galerkin method.

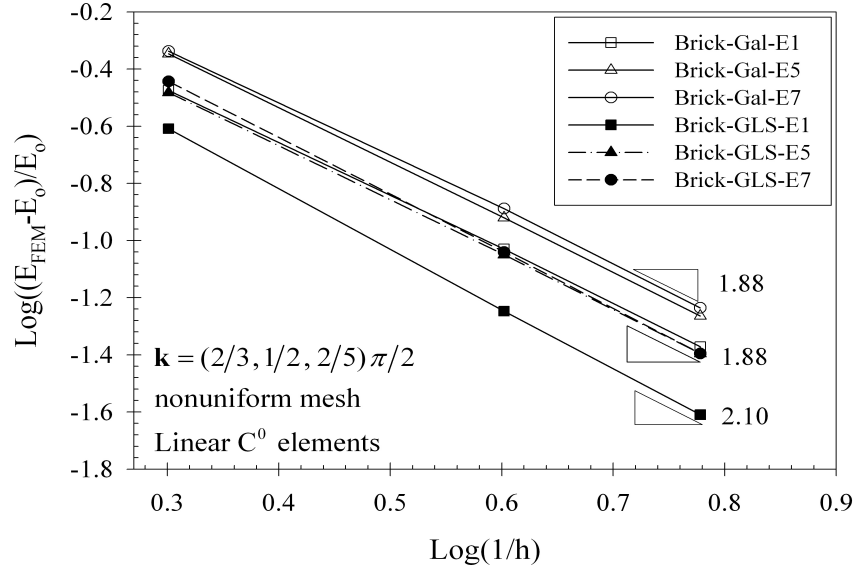


Figure 12. Convergence rates for eigenvalues using linear brick elements.

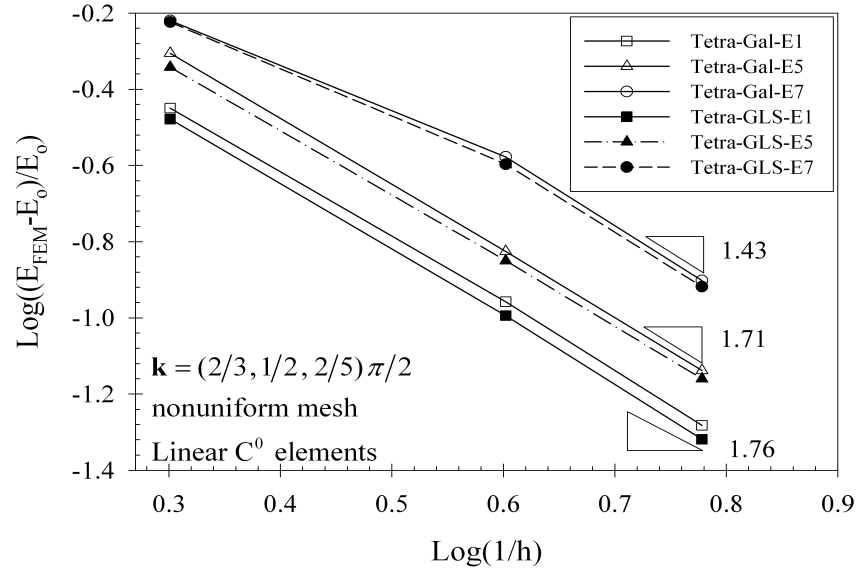


Figure 13. Convergence rates for eigenvalues using linear tetrahedral elements.

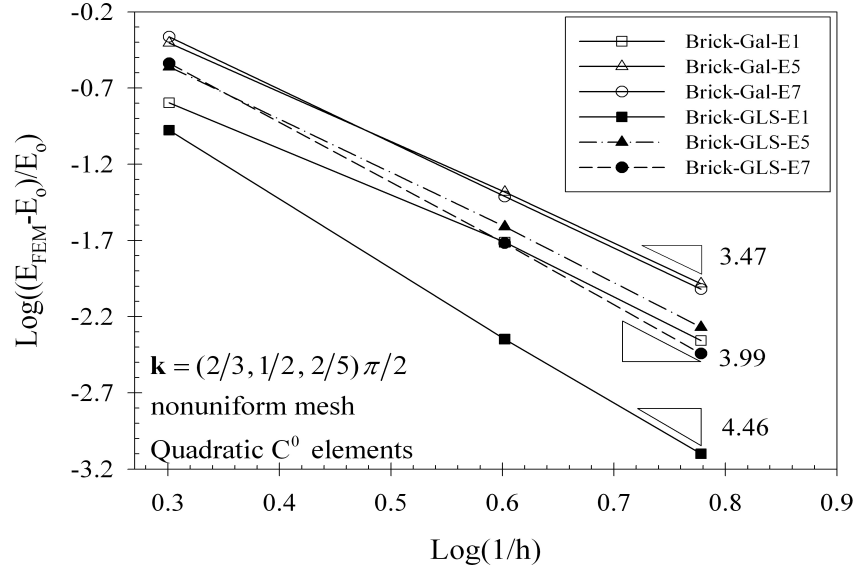


Figure 14. Convergence rates for eigenvalues using quadratic brick elements.

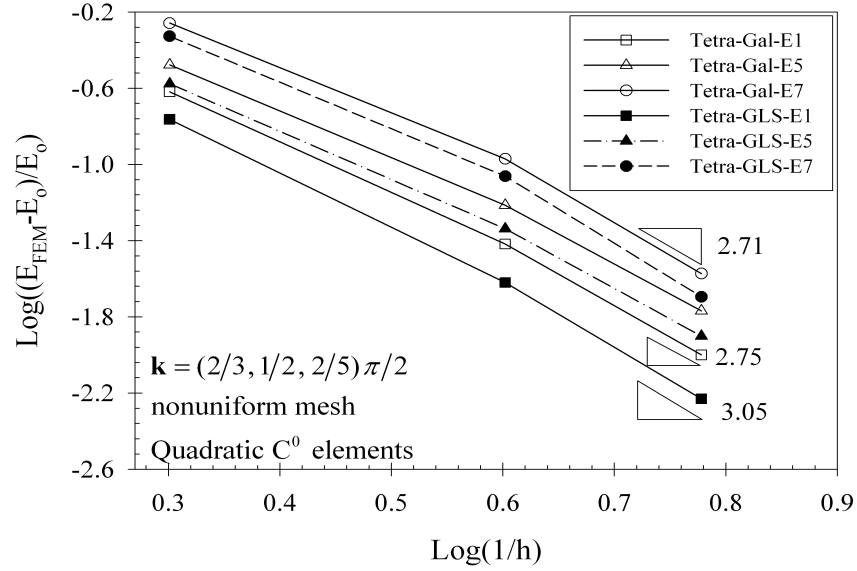


Figure 15. Convergence rates for eigenvalues using quadratic tetrahedral elements.

### 3.4.2 Convergence rate results for the HVM formulation

Figures 16-19 show convergence rates for the HVM method. Meshes employed for the linear elements are composed of  $6 \times 6 \times 6$ ,  $9 \times 9 \times 9$  and  $12 \times 12 \times 12$  elements, while meshes employed for quadratic elements are composed of  $2 \times 2 \times 2$ ,  $4 \times 4 \times 4$  and  $6 \times 6 \times 6$  elements. Once again optimal convergence rates are attained in all the test cases.

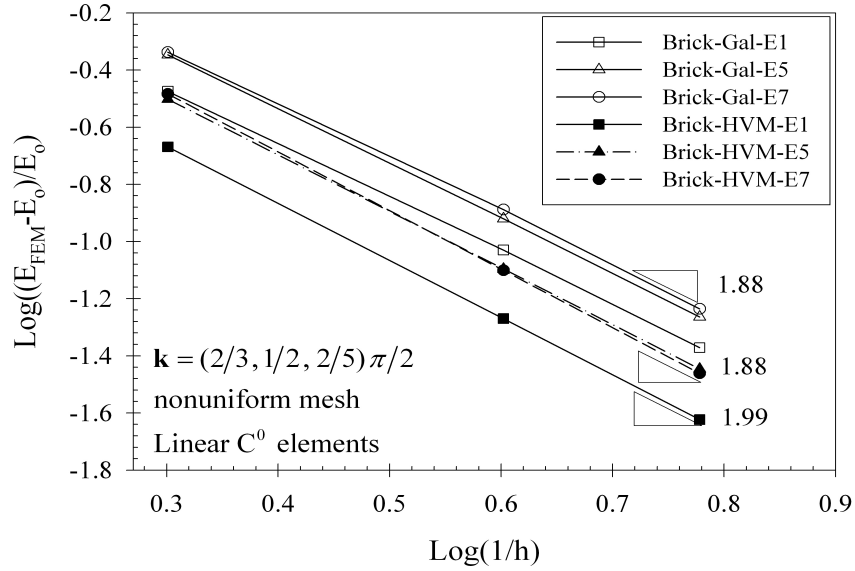


Figure 16. Convergence rates for eigenvalues using linear brick elements.

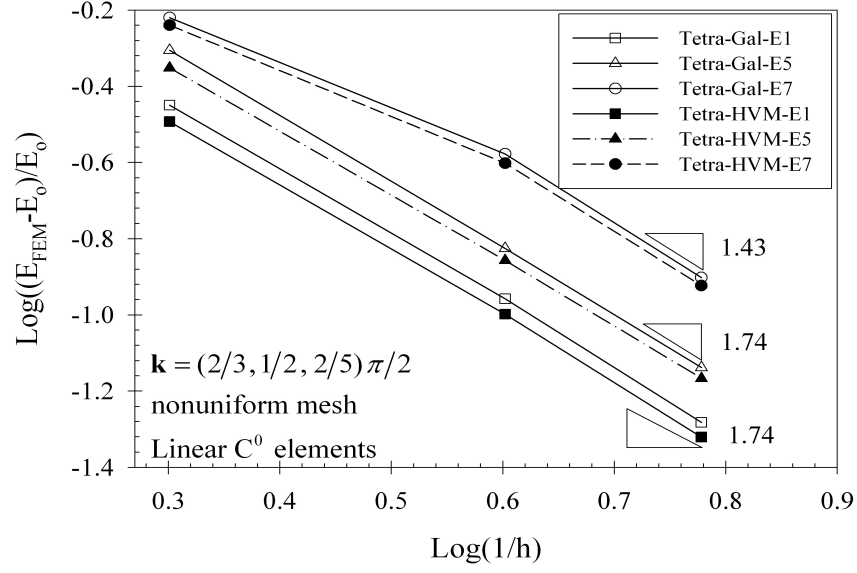


Figure 17. Convergence rates for eigenvalues using linear tetrahedral elements.

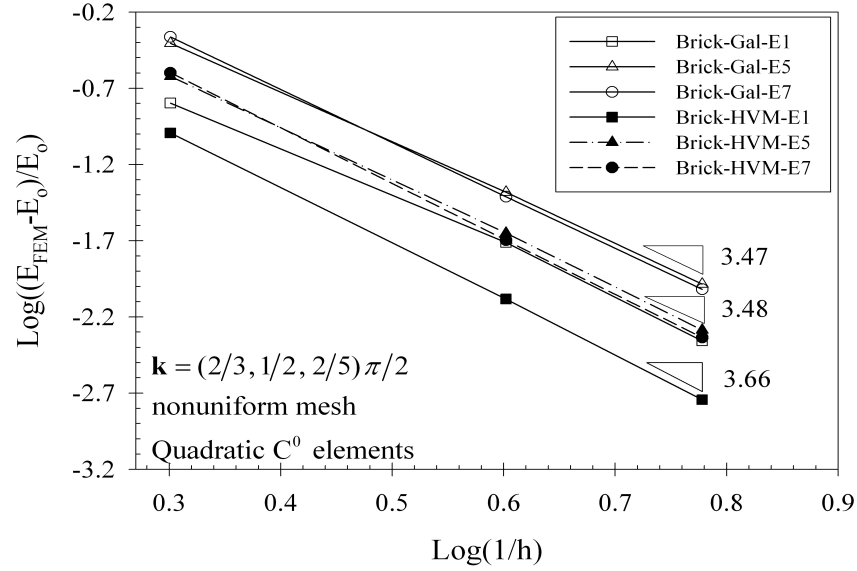


Figure 18. Convergence rates for eigenvalues using quadratic brick elements.



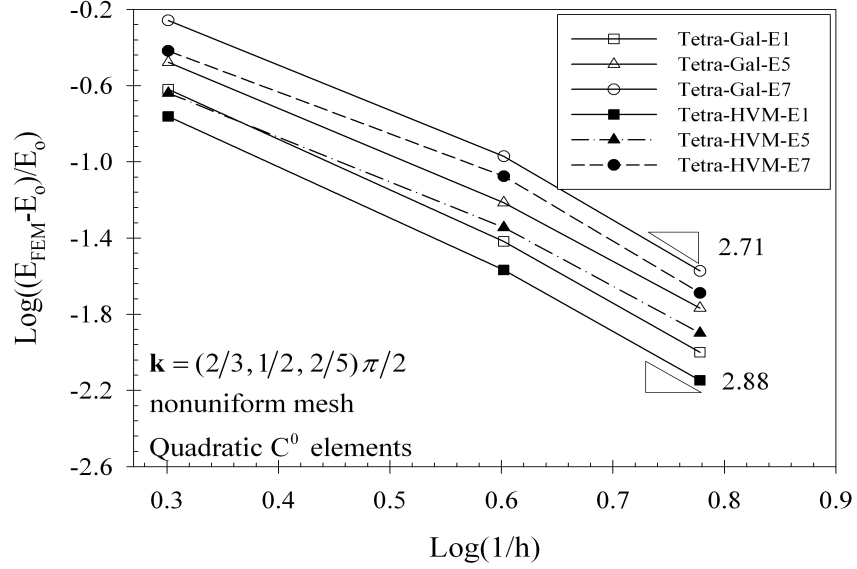


Figure 19. Convergence rate for eigenvalues using quadratic tetrahedral elements.

### 3.4.3 Energy band diagram

Figures 20 and 21 show the eigenvalues computed via the GLS and the HVM formulations for the  $4 \times 4 \times 4$  quadratic brick mesh. Solid lines show the analytical solution and the circles correspond to the computed values. Interested reader is referred to chapter 2 and 3 of Pierrat [54] for a description of the band diagram and the Brillouin zone. In case of Kronig-Penney problem, the first Brillouin zone is a cube of length  $2\pi/3$ . In Figure 20  $\Gamma$  represents the centre of the first Brillouin zone and  $\mathbf{X}$  represents the centre of the face of the first Brillouin zone with unit normal vector  $\langle 1, 0, 0 \rangle$ .

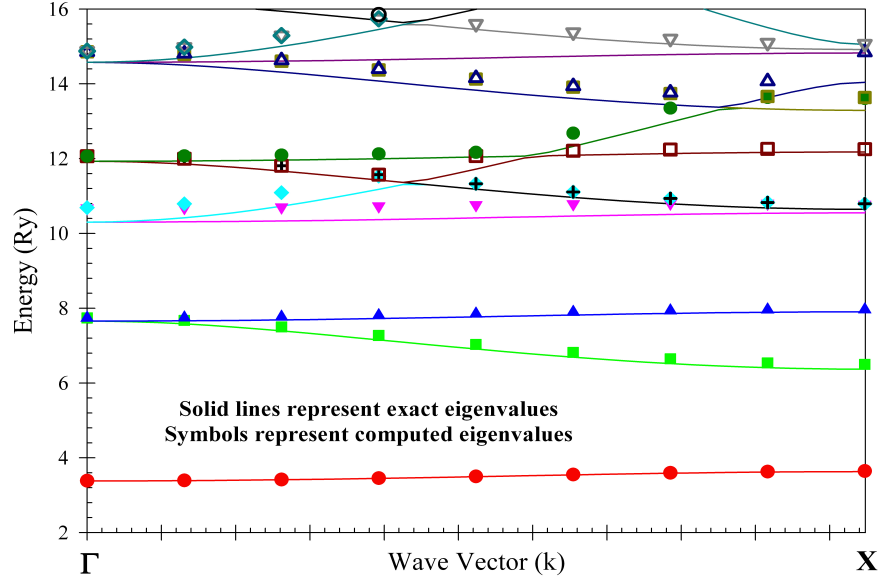


Figure 20. Energy band diagram for the GLS formulation.

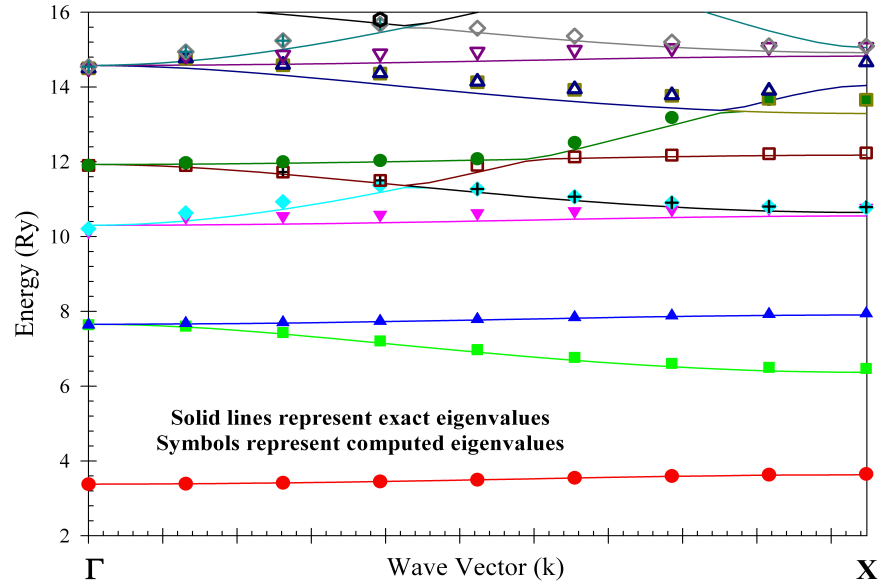


Figure 21. Energy band diagram for the HVM formulation.

### 3.4.4 Convergence rate for a high value of the electronic potential

The range of values for the pseudopotential typically lies between -60 Ry to -10 Ry units. Therefore tests were carried out to see the effects of higher values of the potentials. Figures 22-29 show convergence of the fractional error in the eigenvalues for  $V = 60.5$  Ry. Meshes employed for the present study are same as the ones used in sections 3.4.1 and 3.4.2. Once again optimal rates in the norms considered are attained for the various test cases. The normalized error for Galerkin method is higher even for first few eigenvalues as compared to the GLS and the HVM methods.

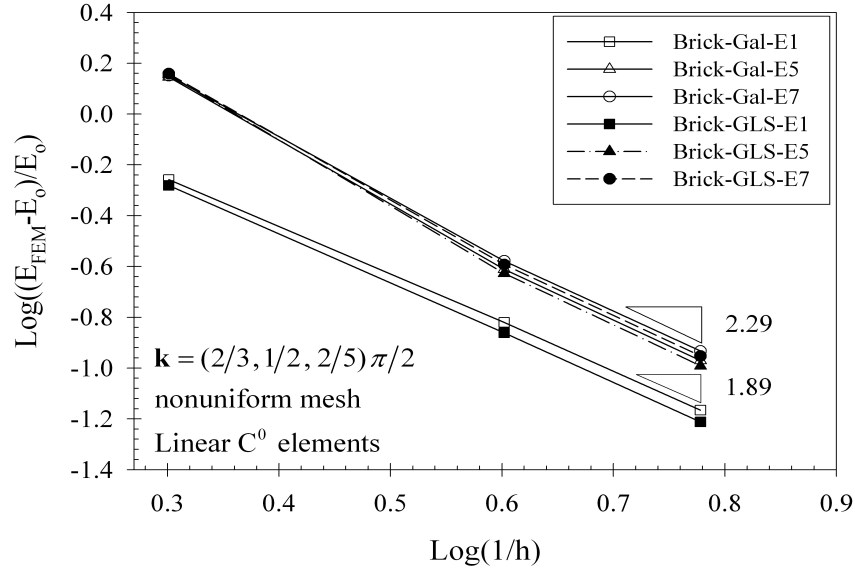


Figure 22. Convergence rates for eigenvalues using linear brick elements (GLS).

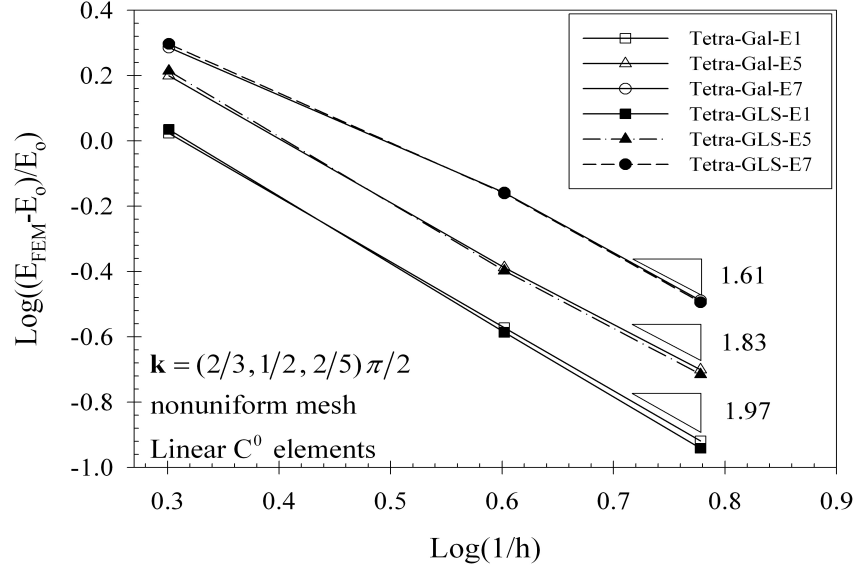


Figure 23. Convergence rates for eigenvalues using linear tetrahedral elements (GLS).

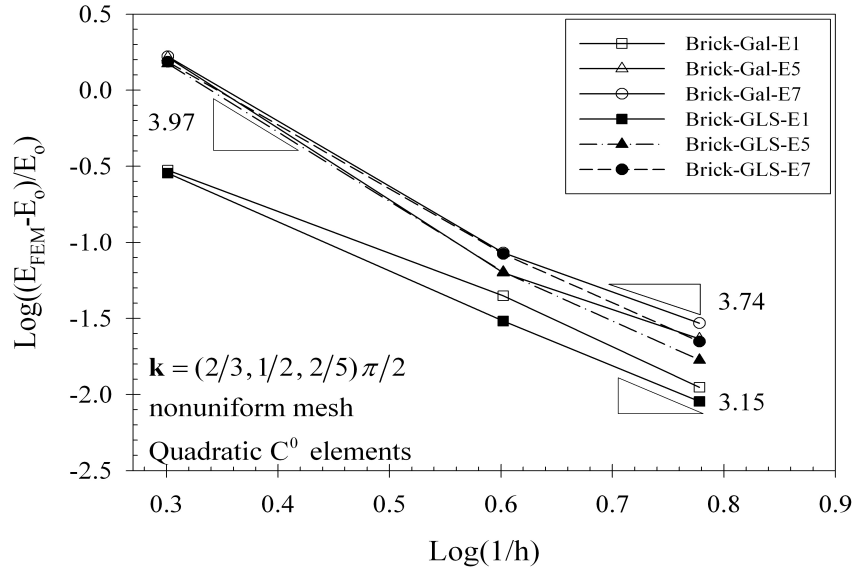


Figure 24. Convergence rates for eigenvalues using quadratic brick elements (GLS).

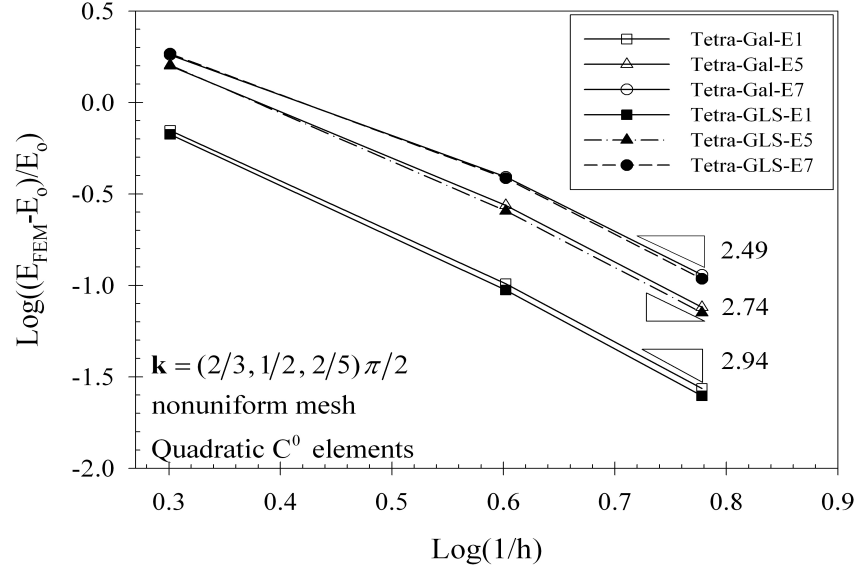


Figure 25. Convergence rates for eigenvalues using quadratic tetrahedral elements (GLS).

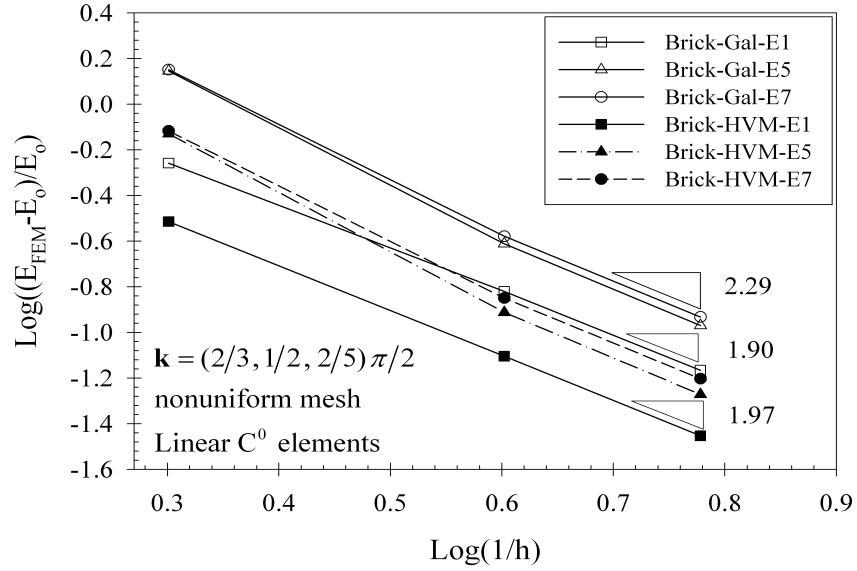


Figure 26. Convergence rates for eigenvalues using linear brick elements (HVM).

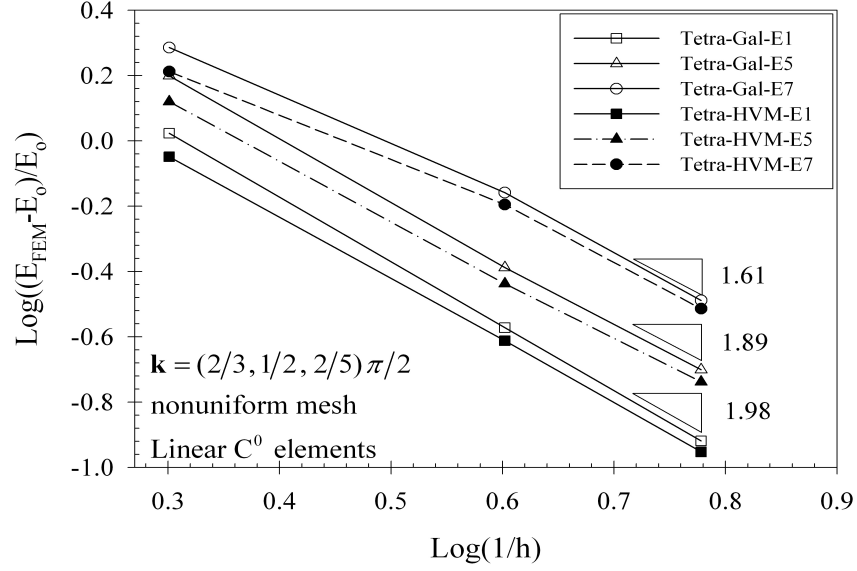


Figure 27. Convergence rates for eigenvalues using linear tetrahedral elements (HVM).

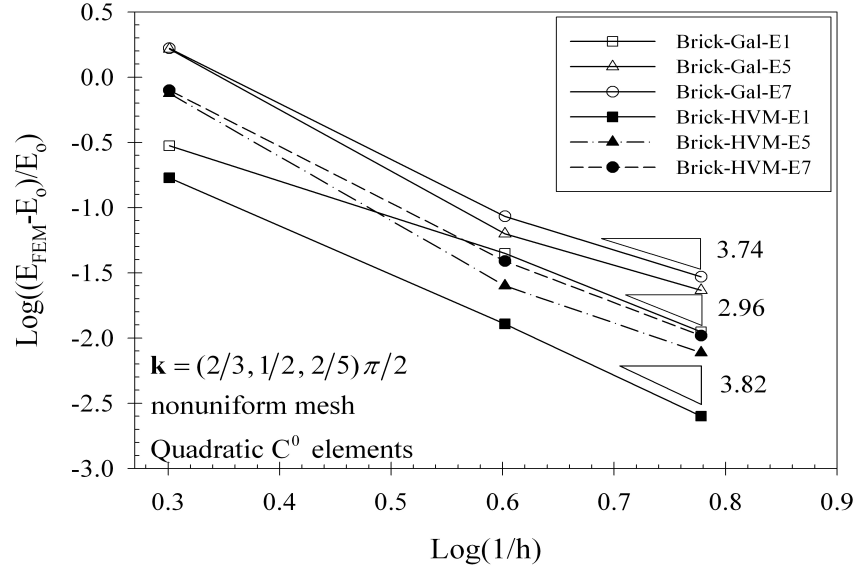


Figure 28. Convergence rates for eigenvalues using quadratic brick elements (HVM).

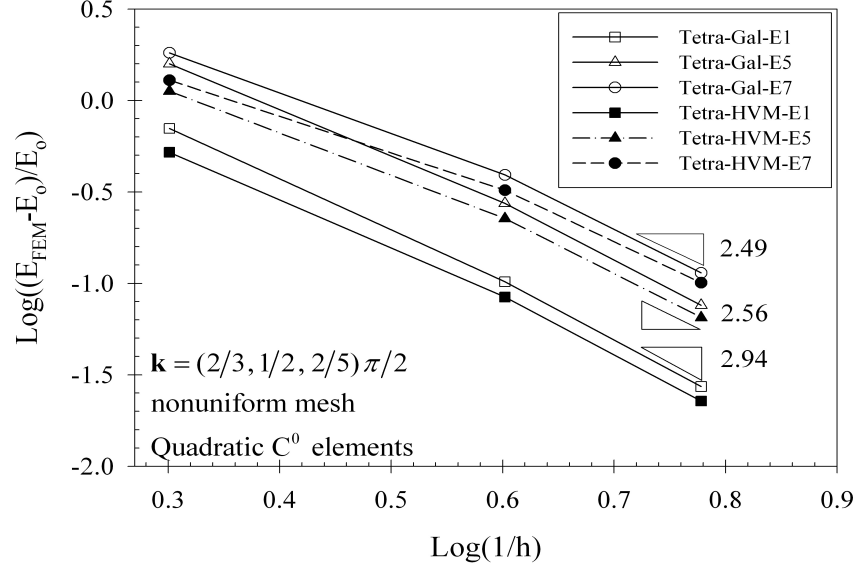


Figure 29. Convergence rates for eigenvalues using quadratic tetrahedral elements (HVM).

## 4 B-SPLINES AND NURBS FINITE ELEMENT METHODS FOR ELECTRONIC STRUCTURE CALCULATIONS

### 4.1 Kohn-Sham Equations

Kohn-Sham framework replaces an original many-body interacting particle problem in an external potential with a non-interacting particle problem moving in an effective potential. The Kohn-Sham equations of DFT [1, 41, 42] are given as follows:

$$-\frac{1}{2}\nabla^2\phi_i(\mathbf{x}) + V_{eff}\phi_i(\mathbf{x}) = \varepsilon_i\phi_i(\mathbf{x}) \quad (4.1)$$

where  $\phi_i(\mathbf{x})$  and  $\varepsilon_i$  are Kohn-Sham eigenfunctions and eigenvalues respectively, and  $V_{eff}$  is the effective electronic potential defined as follows.

$$V_{eff} = V^L + V^{nL} + V_H + V_{XC} \quad (4.2)$$

$$V^L = \sum_a V_a^L(\mathbf{x}) \quad (4.3)$$

$$V^{nL} = \sum_a \int V_a^{nL}(\mathbf{x}, \mathbf{x}') \phi(\mathbf{x}') d\mathbf{x}' \quad (4.4)$$

$$V_H = \int \frac{\rho_e(\mathbf{x}')}{|\mathbf{x} - \mathbf{x}'|} d\mathbf{x}' \quad (4.5)$$



$$V_{XC} = V_{XC}(\mathbf{x}; \rho_e) \quad (4.6)$$

$$\rho_e = \sum_i f_i |\phi_i(\mathbf{x})|^2 \quad (4.7)$$

$V_a^L$  and  $V_a^{nL}$  are the local and non-local terms in the pseudo-potential approximation [45] for an atom denoted by subscript  $a$ .  $V_{XC}$  is the exchange correlation potential,  $V_H$  is the Hartree potential. The form of exchange-correlation potential is determined by the choice of pseudo-potential.  $\rho_e$  is the electron charge density,  $f_i$  is the occupation number associated with eigenstate  $i$ . The integrals extend over all space, with summation extending over all atoms.

The Hartree potential ( $V_H$ ) contains  $1/\vec{r}$  term. Due to this term the total number of terms in the summation of integrand, which extends over all space, is quite large, and therefore computationally inefficient. Accordingly the Hartree term is usually computed by solving an equivalent Poisson problem, instead of actually evaluating the integral given in equation (4.5). By converting the integral into an equivalent Poisson problem, the potential can be computed efficiently. A similar method is used to convert the long range local pseudo-potential into short range densities to achieve computational efficiency.

$$\nabla^2 V_H = \int \nabla^2 \frac{\rho_e(\mathbf{x}')}{|\mathbf{x} - \mathbf{x}'|} d\mathbf{x}' = \int -4\pi \delta(\mathbf{x} - \mathbf{x}') \rho_e(\mathbf{x}') d\mathbf{x}' = -4\pi \rho_e(\mathbf{x}) \quad (4.8)$$

$$\nabla^2 V^L = \sum_a \nabla^2 V_a^L(\mathbf{x}) = \sum_a 4\pi \rho_a^L(\mathbf{x}) \quad (4.9)$$

The Hartree term and the local pseudo-potential term are combined into a single Poisson problem, by evaluating the equivalent density of local pseudo-potential as discussed in Pask *et al.* [1, 2].

$$\nabla^2 V_C = \nabla^2 V_H + \nabla^2 V^L = \sum_a 4\pi\rho_a^L(\mathbf{x}) - 4\pi\rho_e(\mathbf{x}) = f(\mathbf{x}), \quad \mathbf{x} \in \Omega \quad (4.10)$$

where  $V_C$  is the total Coulomb potential.

Due to the nonlinearity engendered by  $V_{eff}$ , the set of equations (4.1) through (4.7) are solved self-consistently until convergence is attained between the newly calculated density and the computed density from the previous iteration. The newly calculated density modifies the effective potential  $V_{eff}$ , especially Hartree and exchange correlation terms. We use Pulay mixing scheme [55] and a history of five calculated densities from previous iterations to evaluate the new density.

**Remark 4.1:** *Different resolution meshes have been employed for the solution of the Poisson problem and the Schrödinger wave equation (SWE). The number of elements for Poisson problem is fixed at 20 for each direction, while that of SWE is varied systematically to determine numerical convergence rates. Since different resolution meshes are used for the coupled Poisson problem and the SWE, the solution from the Poisson/SWE problem is projected on to the mesh of SWE/Poisson problem by finding equivalent integration point through Newton-Raphson method.*

**Remark 4.2:** *Since the B-spline shape function coefficients (control variables) do not have interpolation property, except for at the boundaries, a third mesh is created to find the electron*

charge density values at the nodal points. Electron charge density at any other physical point is determined through Lagrange interpolation functions of the same order as the B-spline functions. The density of this mesh is taken as four times the density of SWE in each direction.

**Remark 4.3:** Mesh refinement was carried out according to the knot insertion rule as discussed in section 4.2.4. This ensures a structured mesh wherein mesh refinement helps conduct convergence rate study.

#### 4.1.1 Solution of periodic systems

The electronic potential for a perfect crystal is periodic.

$$V(\mathbf{x}) = V(\mathbf{x} + \mathbf{R}) \quad (4.11)$$

Bloch's theorem further states that the solution of Schrödinger wave equation (4.1) satisfies the following equations.

$$\phi(\mathbf{x}) = v(\mathbf{x}) e^{i\mathbf{k} \bullet \mathbf{x}} \quad (4.12)$$

where  $\mathbf{k}$  is wavevector (position vector in reciprocal space) and  $v(\mathbf{x}) = v(\mathbf{x} + \mathbf{R})$  is a complex-valued cell periodic function that satisfies the periodic property for all lattice vectors  $\mathbf{R}$ .

#### 4.1.2 Schrödinger wave equation

Let  $\Omega \subset \mathbb{R}^{n_{sd}}$  be an open bounded region with piece wise smooth boundary  $\Gamma$ . The number of space dimensions,  $n_{sd} = 3$ . Applying Bloch's theorem to the Schrödinger equation (4.1) we get

$$-\frac{1}{2}\Delta v(\mathbf{x}) - i\mathbf{k} \bullet \nabla v(\mathbf{x}) + \frac{1}{2}k^2 v(\mathbf{x}) + V(\mathbf{x})v(\mathbf{x}) = \varepsilon(\mathbf{k})v(\mathbf{x}), \quad \mathbf{x} \in \Omega \quad (4.13)$$

$$v(\mathbf{x}) = v(\mathbf{x} + \mathbf{R}), \quad \mathbf{x} \in \Gamma \quad (4.14)$$

$$\mathbf{n} \bullet \nabla v(\mathbf{x}) = \mathbf{n} \bullet \nabla v(\mathbf{x} + \mathbf{R}) \quad \mathbf{x} \in \Gamma \quad (4.15)$$

where  $v(\mathbf{x})$  is the complex valued cell periodic function or the unknown complex scalar field, namely the wave function (eigenfunction),  $i$  is the imaginary unit,  $\mathbf{x}$  represents the position vector,  $\mathbf{n}$  represents outward unit normal vector to the boundary  $\Gamma$  of a unit cell,  $V(\mathbf{x})$  is the electronic potential or the potential energy of an electron in a charge density  $\rho_e(\mathbf{x})$  at the position  $\mathbf{x}$  and is considered periodic over a unit cell.  $\varepsilon(\mathbf{k})$  is the eigen-energy associated with the particle as a function of wavevector (position vector in reciprocal space)  $\mathbf{k}$ .  $\mathbf{R}$  refers to the lattice vectors of the unit cell.

In the context of pseudo-potential approximation [45] and Kohn-Sham framework, the all-electron potential  $V(\mathbf{x})$  is replaced by  $V_{eff}$  (see equation (2)).

$$\begin{aligned} & -\frac{1}{2}\Delta v(\mathbf{x}) - i\mathbf{k} \bullet \nabla v(\mathbf{x}) + \frac{1}{2}k^2 v(\mathbf{x}) + (V^L + V_H + V_{XC}) v(\mathbf{x}) \\ & + e^{-i\mathbf{k} \bullet \mathbf{x}} V^{nL} e^{i\mathbf{k} \bullet \mathbf{x}} v(\mathbf{x}) = \varepsilon(\mathbf{k}) v(\mathbf{x}) \end{aligned} \quad (4.16)$$

The Schrödinger wave equation (4.13) is solved in a periodic and finite domain. However the non-local term  $V^{nL}$  involves integration over entire space and over all atoms. Therefore, this term needs further consideration. Pask *et al.* [1] uses the following procedure to reduce the

non-local term integrated over all space to an integral form defined over a unit cell. A fully separable pseudo-potential [45] for an atom  $a$  usually has the following form.

$$V_a^{nL}(\mathbf{x}, \mathbf{x}') = \sum_{l,m} \chi_{lm}^a(\mathbf{x}) h_l^a \chi_{lm}^a(\mathbf{x}') \quad (4.17)$$

Using equations (4.4) and (4.17), the non-local term  $e^{-i\mathbf{k}\bullet\mathbf{x}} V^{nL} e^{i\mathbf{k}\bullet\mathbf{x}} v(\mathbf{x})$  then becomes

$$\begin{aligned} & e^{-i\mathbf{k}\bullet\mathbf{x}} \sum_{n,a} \int V_a^{nL}(\mathbf{x} - \boldsymbol{\tau}_a - \mathbf{R}_n, \mathbf{x}' - \boldsymbol{\tau}_a - \mathbf{R}_n) v(\mathbf{x}') e^{i\mathbf{k}\bullet\mathbf{x}'} d\mathbf{x}' \\ & = e^{-i\mathbf{k}\bullet\mathbf{x}} \sum_{n,a,l,m} \chi_{lm}^a(\mathbf{x} - \boldsymbol{\tau}_a - \mathbf{R}_n) h_l^a \int \chi_{lm}^a(\mathbf{x}' - \boldsymbol{\tau}_a - \mathbf{R}_n) v(\mathbf{x}') e^{i\mathbf{k}\bullet\mathbf{x}'} d\mathbf{x}' \end{aligned} \quad (4.18)$$

where the integral is over all space centered around an atom located at  $\boldsymbol{\tau}_a$  in a unit cell with origin  $\mathbf{R}_n$ ,  $n$  runs over all lattice vectors  $\mathbf{R}_n$ , and  $a$  runs over all atoms in a unit cell. The integral centered on an atom  $a$  can be written as sum of integrals over unit cells surrounding the atom, which can be further reduced to integral over a unit cell as follows.

$$\begin{aligned} & \int \chi_{lm}^a(\mathbf{x}' - \boldsymbol{\tau}_a - \mathbf{R}_n) v(\mathbf{x}') e^{i\mathbf{k}\bullet\mathbf{x}'} d\mathbf{x}' \\ & = \sum_{n'} \int_{\Omega_{n'}} \chi_{lm}^a(\mathbf{x}' - \boldsymbol{\tau}_a - \mathbf{R}_n) v(\mathbf{x}') e^{i\mathbf{k}\bullet\mathbf{x}'} d\mathbf{x}' \\ & = \sum_{n'} \int_{\Omega} \chi_{lm}^a(\mathbf{x}' - \boldsymbol{\tau}_a - \mathbf{R}_n - \mathbf{R}_{n'}) v(\mathbf{x}' - \mathbf{R}_{n'}) e^{i\mathbf{k}\bullet(\mathbf{x}' - \mathbf{R}_{n'})} d\mathbf{x}' \end{aligned} \quad (4.19)$$

Replacing  $\mathbf{x}' - \mathbf{R}_n$  by  $\mathbf{x}'$  and using  $v(\mathbf{x}) = v(\mathbf{x} + \mathbf{R})$  we have

$$\begin{aligned} & \int \chi_{lm}^a(\mathbf{x}' - \boldsymbol{\tau}_a - \mathbf{R}_n) v(\mathbf{x}') e^{i\mathbf{k}\bullet\mathbf{x}'} d\mathbf{x}' \\ & = \sum_{n'} \int_{\Omega} \chi_{lm}^a(\mathbf{x}' - \boldsymbol{\tau}_a - \mathbf{R}_{n'}) v(\mathbf{x}') e^{i\mathbf{k}\bullet\mathbf{x}'} e^{i\mathbf{k}\bullet\mathbf{R}_n} e^{-i\mathbf{k}\bullet\mathbf{R}_{n'}} d\mathbf{x}' \end{aligned} \quad (4.20)$$

The non-local term  $e^{-i\mathbf{k}\bullet\mathbf{x}} V^{nL} e^{i\mathbf{k}\bullet\mathbf{x}} v(\mathbf{x})$  reduces to

$$\sum_{a,l,m} \left\{ e^{-i\mathbf{k}\bullet\mathbf{x}} \sum_n [e^{i\mathbf{k}\bullet\mathbf{R}_n} \chi_{lm}^a(\mathbf{x} - \boldsymbol{\tau}_a - \mathbf{R}_n)] \times h_l^a \times \int_{\Omega} \left( e^{i\mathbf{k}\bullet\mathbf{x}'} \sum_{n'} [e^{-i\mathbf{k}\bullet\mathbf{R}_{n'}} \chi_{lm}^a(\mathbf{x}' - \boldsymbol{\tau}_a - \mathbf{R}_{n'})] v(\mathbf{x}') d\mathbf{x}' \right) \right\} \quad (4.21)$$

#### 4.1.3 The standard weak form

Let  $\mathcal{V} \subset H^1(\Omega^{n_{sd}}) \cap C^0(\Omega^{n_{sd}})$  denote the space of trial solutions and weighting functions for the unknown scalar field.

$$\mathcal{V} = \{v | v \in H^1(\Omega^{n_{sd}}), v(\mathbf{x}) = v(\mathbf{x} + \mathbf{R}) \quad \forall \mathbf{x} \in \Gamma\} \quad (4.22)$$

The standard weak form is

$$-(w, i\mathbf{k} \bullet \nabla v) + \frac{1}{2} (\nabla w, \nabla v) + \frac{1}{2} (w, k^2 v) + (w, V_{eff} v) = (w, \varepsilon v) \quad (4.23)$$

where  $w$  is the weighting function for  $v$ , and  $(\bullet, \bullet) = \int_{\Omega} (\bullet) d\Omega$  i.e.,  $L_2$  product of the indicated arguments over domain  $\Omega$ .

**Remark 4.4:** *The non-local term in  $V_{eff}$  requires to be handled differently from the conventional element based local evaluation of the finite element matrices and vectors. This is presented explicitly in Appendix A.*

**Remark 4.5:** *Effective potential,  $V_{eff}$ , is non-linear because of the presence of the terms  $V_H$  and  $V_{XC}$  (equation (4.2)) that are in turn functions of the electronic charge density (equa-*

tions (4.5) and (4.6)). Electronic density ( $\rho_e$ ) is calculated from eigenfunctions as shown in equation (4.7).

**Remark 4.6:** Our objective in this work is to explore the higher order smoothness facilitated by the B-splines and NURBS basis functions in the context of the finite element methods as applied to electronic structure calculations.

**Remark 4.7:** B-spline control variables have interpolatory property only at the boundary of the domain due to the repeated knot values at the ends of the knot vectors. Periodic boundary condition is applied by repeating the same control variables at the corresponding boundaries.

Let  $\mathcal{V}^h \subset \mathcal{V}$  denote the finite-dimensional approximation of space of the trial solutions and weighting functions for the unknown scalar field.

$$-\left(w^h, i\mathbf{k} \bullet \nabla v^h\right) + \frac{1}{2} \left(\nabla w^h, \nabla v^h\right) + \frac{1}{2} \left(w^h, k^2 v^h\right) + \left(w^h, V_{eff} v^h\right) = \left(w^h, \varepsilon v^h\right) \quad (4.24)$$

Let  $v^h = \sum_{i=1}^n c_i N_i$  and  $w^h = \sum_{i=1}^n d_i N_i$ , where  $c_i$ ,  $d_i$  are complex coefficients associated with corresponding shape functions for the trial solution and weighting functions respectively. Since the shape functions have local support, the discrete equation takes the following form.

$$\sum_j K_{ij} c_j = \varepsilon \sum_j M_{ij} c_j \quad (4.25)$$

where

$$K_{ij} = \sum_{e=1}^{numel} K_{ij}^e; \quad M_{ij} = \sum_{e=1}^{numel} M_{ij}^e \quad (4.26)$$

$$K_{ij}^e = \int_{\Omega^e} \left( \frac{1}{2} \nabla N_i \bullet \nabla N_j - i \mathbf{k} \bullet N_i \nabla N_j + \frac{1}{2} \mathbf{k}^2 N_i N_j + V_{eff} N_i N_j \right) d\mathbf{x} \quad (4.27)$$

$$M_{ij}^e = \int_{\Omega^e} N_i N_j d\mathbf{x} \quad (4.28)$$

where  $\mathbb{A}$  stands for assembly operation,  $\int_{\Omega^e}$  stands for integration over an element domain  $\Omega^e$  of finite element mesh, and  $numel$  stands for the total number of elements in the finite element mesh.

#### 4.1.4 The Poisson problem

Let  $\Omega \subset \mathbb{R}^{n_{sd}}$  be an open bounded region with piecewise smooth boundary  $\Gamma$ . The number of space dimensions,  $n_{sd} = 3$ .

$$\nabla^2 V_C = f(\mathbf{x}), \quad \mathbf{x} \in \Omega \quad (4.29)$$

$$V_C(\mathbf{x}) = V_C(\mathbf{x} + \mathbf{R}), \quad \mathbf{x} \in \Gamma \quad (4.30)$$

$$\mathbf{n} \cdot \nabla V_C(\mathbf{x}) = \mathbf{n} \cdot \nabla V_C(\mathbf{x} + \mathbf{R}), \quad \mathbf{x} \in \Gamma \quad (4.31)$$

where  $V_C = V_H + V^L$ , and  $f(\mathbf{x}) = \sum_a 4\pi \rho_a^L(\mathbf{x}) - 4\pi \rho_e(\mathbf{x})$  as shown in equation (4.10).  $\mathbf{n}$  represents outward unit normal vector to the boundary  $\Gamma$  of a unit cell  $\Omega$ .

**Remark 4.8:** *The charge densities that are consistent with a derivative periodic smoothly varying function are the ones that are net neutral in the unit cell, as given in the following equation.*



$$\begin{aligned}
\int_{\Omega} f(\mathbf{x}) d\Omega &= \int_{\Omega} \Delta V_C(\mathbf{x}) d\Omega = \int_{\Gamma} \mathbf{n} \cdot \nabla V_C(\mathbf{x}) d\Gamma \\
&= \int_{\Gamma} (\mathbf{n} \cdot \nabla V_C(\mathbf{x}) - \mathbf{n} \cdot \nabla V_C(\mathbf{x} + \mathbf{R})) d\Gamma = 0
\end{aligned} \tag{4.32}$$

**Remark 4.9:** *The local pseudopotential term is converted into equivalent density term as shown in equation (4.9). These density terms for each nuclei position are then superimposed at a location  $\mathbf{x}$  in order to obtain the total density. See section 4 of Pask et al. [1] for more details as well as Appendix B. In addition the density term  $f(\mathbf{x})$ , also includes the electron charge density as shown in equations (4.7) and (4.10). Thus the solution of Poisson equation includes the effects of local pseudopotential term as well as the Hartree potential.*

#### 4.1.5 The standard weak form for the Poisson problem

Let  $\mathcal{S} \subset H^1(\Omega^{n_{sd}}) \cap C^0(\Omega^{n_{sd}})$  denote the space of trial solutions and weighting functions for the unknown scalar field.

$$\mathcal{S} = \{ V_C | V_C \in H^1(\Omega^{n_{sd}}), V_C(\mathbf{x}) = V_C(\mathbf{x} + \mathbf{R}) \quad \forall \mathbf{x} \in \Gamma \} \tag{4.33}$$

The standard weak form is

$$-(\nabla w, \nabla V_C) = (w, f(\mathbf{x})) \tag{4.34}$$

where  $w$  is the weighting function for  $V_C$ , and  $(\bullet, \bullet) = \int_{\Omega} (\bullet) d\Omega$  is the  $L_2$  product of the indicated arguments over domain  $\Omega$ .

Let  $\mathcal{S}^h \subset \mathcal{S}$  denote the finite-dimensional approximation of space of trial solutions and weighting functions for the unknown scalar field. The discretized weak form is:

$$-\left(\nabla w^h, \nabla V_C^h\right)=\left(w^h, f(\boldsymbol{x})\right) \quad (4.35)$$

## 4.2 B-splines and NURBS

NURBS (Non-uniform rational B-splines) are parametric functions of rational polynomials that are typically employed in computer aided design (CAD) to accurately represent complex geometrical shapes with as few parameters as possible. In a series of landmark papers Hughes and coworkers [46] have introduced the notion of Isogeometric Analysis (IGA) wherein B-splines and NURBS are employed for the modeling and analysis of engineering problems. IGA has been successfully applied to fluid mechanics [56, 57] as well as solid/structural mechanics [58, 59]. Amongst the main attributes of the B-splines and NURBS based methodology is the geometrically exact description of the domain of computation, higher order regularity of the method due to the notion of  $k$ -refinement [46], and an efficient integration of the analysis framework with the CAD based geometric modeling framework.

In electronic structure modeling, the unit cell (computational domain) can possess hollow cylindrical configuration like that of the carbon nanotubes (CNTs), solid cylindrical configuration like silicon nanowires, or geometries with conic sections for the deformed nanotubes or nanowires. Because of the (i) exact geometric description of the unit cells in the physical space for various material types, (ii) periodicity of non-linear potentials, and (iii) symmetric and periodic boundary conditions applied on the corresponding surfaces of the unit cell, NURBS based technology offers definite advantage as compared to  $C^0$  framework with reduced regularity and Lagrange interpolation functions. We discuss salient features of B-splines and NURBS in one-

dimensional context, followed by procedure to build multi-dimensional B-spline basis functions in the context of finite elements and conclude with procedure to build NURBS functions out of B-spline functions for one dimensional and multi-dimensional cases. For details interested reader is directed to Piegl and Tiller [60], and Hughes *et al.* [46] for further details.

#### 4.2.1 Knot vectors

Knot vectors define the parametric space for the B-spline functions. They are composed of a sequence of non-decreasing real numbers,  $\Xi = \{\xi_i\}_{i=1}^{n+p+1}$ , where  $\xi_i \leq \xi_{i+1} \in \mathbb{R}$ ,  $i$  is the knot index,  $\xi_i$  is the  $i^{th}$  knot,  $n$  is the total number of basis functions, and  $p$  is the polynomial order or polynomial degree. The interval between two consequent knots, called knot span  $[\xi_i, \xi_{i+1})$  in a knot vector represents an element of the finite element mesh in the parametric space.

**Remark 4.10:** *Once the degree of polynomial is chosen, the knot vector determines completely all the basis functions. Unlike the Lagrange functions, B-spline basis functions are defined in parametric space and not in physical or integration domain.*

**Remark 4.11:** *Unlike the Lagrange functions, B-spline functions do not possess interpolation property corresponding to any knot value. B-splines possess interpolation property on internal knots if they are repeated  $p$  times, and at first and last knots if first and last knots are repeated  $p + 1$  times.*

**Remark 4.12:** *For any interior knot, a B-spline basis function of order  $p$  is  $p - k$  times continuously differentiable, where  $k$  is the multiplicity of the knot. Increasing multiplicity of knots decreases continuity of B-spline basis functions.*

**Remark 4.13:** *When the first and last knots are repeated  $p + 1$  times, then the knot vector is called as non-periodic or open or clamped knot vectors. This ensures B-splines have interpolation property at the corresponding extreme points and application of Dirichlet or periodic boundary conditions become easier. Periodic boundary conditions can also be applied by making first and last knot values equal, but in this paper we limit our discussion to open knot vectors as defined above.*

**Remark 4.14:** *If the knots are equally spaced then they are uniform knot vector, else they are non-uniform knot vectors. The selection of uniform or non-uniform knot vectors is dependent on the physical problem. If a non-uniform mesh can capture the solution more efficiently, then a non-uniform knot vector may be preferred. Non-uniform meshes can be generated by changing other mesh parameters also. This will be discussed in subsequent section (see section 4.2.3).*

#### 4.2.2 Definition and properties of B-splines

There are many definitions of B-spline functions in the literature [46,60,61]. The following definition is based on recurrence formula that Hughes *et al.* [46] have employed in the finite element context. For knot sequence  $\Xi = \{\xi_i\}_{i=1}^{n+p+1}$  as defined in section 4.2.1, B-spline functions of degree zero, i.e.  $p = 0$  is defined as

$$N_{i,0}(\xi) = \begin{cases} 1 & \text{if } \xi_i \leq \xi < \xi_{i+1}, \\ 0 & \text{otherwise.} \end{cases} \quad (4.36)$$

and for  $p \geq 1$

$$N_{i,p}(\xi) = \omega_{i,p}(\xi) N_{i,p-1}(\xi) + (1 - \omega_{i+1,p}(\xi)) N_{i+1,p-1}(\xi) \quad (4.37)$$

where

$$\omega_{i,p}(\xi) = \begin{cases} (\xi - \xi_i) / (\xi_{i+p} - \xi_i) & \text{if } \xi_i \neq \xi_{i+p} \\ 0 & \text{otherwise.} \end{cases} \quad (4.38)$$

**Remark 4.15:**  $N_{i,p}(\xi) = 0$  if  $\xi$  is outside the interval  $[\xi_i, \xi_{i+p+1})$ , i.e. the B-spline functions have local support property. This also shows that B-spline basis functions span over couple of elements of finite element mesh, as knot span  $[\xi_i, \xi_{i+1})$  represents an element of a finite element mesh in the parametric space.

**Remark 4.16:** In any given knot span, at the most  $p + 1$  B-spline basis functions are non-zero.

**Remark 4.17:**  $N_{i,p}(\xi) \geq 0$  for all  $i, p$  and  $\xi$  (non-negativity).

**Remark 4.18:**  $\sum_{j=i-p}^i N_{j,p}(\xi) = 1 \quad \forall \xi \in [\xi_i, \xi_{i+1})$  (partition of unity).

### 4.2.3 Curves as B-spline parametric functions

A curve in  $\mathbb{R}^{n_{sd}}$  is represented by linear combination of B-spline basis functions.

$$C(\xi) = \sum_{i=1}^n B_i N_{i,p}(\xi) \quad (4.39)$$

where  $n$  is the number of basis functions,  $B_i \in \mathbb{R}^{n_{sd}}$ ,  $i = 1, 2, \dots, n$  are the coefficients of B-spline basis functions  $N_{i,p}(\xi)$  and are called the control points. As discussed in remark 13, B-splines do not possess interpolation property where knot values are not repeated. Hence, control points are

not nodal co-ordinates of the physical mesh at these knot values unlike coefficients of Lagrange basis functions. As discussed in remark 14, repetition of knots decreases the continuity of B-spline basis functions, which in turn reduces the continuity of B-spline curves.

**Remark 4.19:** *Equally spaced control points create a non-uniform mesh. By varying control points one can control the geometric shape of the curve and/or the length of mesh elements.*

#### 4.2.4 $h$ -refinement, $p$ -refinement and $k$ -refinement

In order to perform convergence tests with B-spline basis functions, a  $h$ -refinement and a  $p$ -refinement process is required. The following procedures employed by Hughes *et al.* [46] ensures a uniform mesh for convergence analysis. In addition this process should ensure that the curve does not change geometrically or parametrically.

$h$ -refinement is carried out through knot insertion. Let  $\Xi = \{\xi_i\}_{i=1}^{n+p+1}$  be a knot vector with the properties mentioned in section 4.2.1. Let  $\{B_i\}_{i=1}^n$  be the control points associated with a curve for the knot vector  $\Xi = \{\xi_i\}_{i=1}^{n+p+1}$ . If  $\bar{\xi} \in [\xi_k, \xi_{k+1})$  is the new knot value to be inserted, then the new knot vector is  $\Xi = \{\xi_1, \xi_2, \dots, \xi_k, \bar{\xi}, \xi_{k+1}, \dots, \xi_{n+p+1}\}$ . The corresponding  $\{\bar{B}_i\}_{i=1}^{n+1}$  control points are defined as follows. +

$$\bar{B}_i = \alpha_i B_i + (1 - \alpha_i) B_{i-1} \quad (4.40)$$

where

$$\alpha_i = \begin{cases} 1, & 1 \leq i \leq k - p, \\ \frac{\bar{\xi} - \xi_i}{\xi_{i+p} - \xi_i}, & k - p + 1 \leq i \leq k, \\ 0, & k + 1 \leq i \leq n + p + 2. \end{cases} \quad (4.41)$$

**Remark 4.20:** *Mesh refinement for each geometry in numerical results section, was carried out beginning with the lowest possible mesh resolution. In case of cubic domains, the lowest mesh resolution is single element in physical domain and the corresponding knot vector in each direction is  $\left\{ \underbrace{0, 0, \dots, 0}_{p+1}, \dots, \underbrace{1, \dots, 1}_{p+1} \right\}$ .*

Degree elevation or  $p$ -refinement is carried out by a three step process.

1. Convert each segment of B-spline curve, defined by  $[\xi_k, \xi_{k+1})$ , into Bezier segments by repeating the interior knot values  $p$  times, i.e. by knot insertion and finding the new control points.
2. Degree elevate each of these Bezier segments by repeating the knot values of the segment one more time. If  $\{B_i\}_{i=0}^p$  represents the control points of order  $p$  Bezier segment and  $\{Q_i\}_{i=0}^{p+1}$  the control points of order elevated segment, i.e. corresponding  $p+1$  order Bezier segment, then

$$Q_i = (1 - \alpha_i) B_i + \alpha_i B_{i-1} \quad (4.42)$$

where

$$\alpha_i = \frac{i}{p+1}, \quad i = 0, \dots, p+1 \quad (4.43)$$

3. Remove the unnecessary knot values inserted in step (i) and find the new control points.

This gives the control points for the degree elevated or  $p$ -refined mesh.

The above process is to be repeated for each segment consecutively. A detailed description of the procedure for degree elevation can be obtained from Piegl and Tiller [60].

**Remark 4.21:** *In degree elevation process, say from  $p$  to  $p + 1$  knot values in the interior of knot vectors corresponding to order  $p$ , must be repeated at the least one more time. This reduces the number of continuous derivatives for the basis functions, and consequently that of the curve to  $p - 1$ , even after the degree of the curve is elevated to  $p + 1$ .*

In order to overcome the disadvantage stated in remark 21, Hughes *et al.* [46] suggested an alternative to  $p$ -refinement, which is termed as  $k$ -refinement. In this process, we degree elevate the curve with the lowest possible mesh resolution and then apply  $h$ -refinement process as discussed in this section. In most cases, the lowest possible mesh resolution for a curve is already in the form of Bezier segments, and thus the degree elevation process reduces to only step (2.) of  $p$ -refinement process discussed above. This greatly simplifies the algorithmic process. In all convergence studies involving degree elevation,  $k$ -refinement is used.

#### 4.2.5 Higher dimensional B-splines

Higher dimensional B-splines in  $\mathbb{R}^{n_{sd}}$  are obtained by tensor product of single dimensional B-splines. Here we show how three-dimensional basis functions are used to create volumes or solids, which is relevant to physical problems. Just as control points used in defining one-dimensional curves, we use control nets to define solids or surfaces. Given a control net  $\{B_{i,j,k}\}$ , where  $i = 1, 2, \dots, n$ ,  $j = 1, 2, \dots, m$ ,  $k = 1, 2, \dots, l$ , and  $n, m, l$ , are the number of basis functions in each of the parametric directions corresponding to knot vectors as  $\Xi = \{\xi_i\}_{i=1}^{n+p+1}$ ,  $H = \{\eta_i\}_{i=1}^{m+q+1}$ ,  $L = \{\zeta_i\}_{i=1}^{l+r+1}$ , where  $p, q, r$ , are the degrees of one dimensional B-spline basis functions of corresponding parametric directions, the B-spline solid is defined as follows.



$$S(\xi, \eta, \zeta) = \sum_{i=1}^n \sum_{j=1}^m \sum_{k=1}^l B_{i,j,k} N_{i,p}(\xi) M_{j,q}(\eta) L_{k,r}(\zeta) \quad (4.44)$$

#### 4.2.6 Rational B-splines

Rational B-splines are rational B-spline polynomial functions. Quadratic rational B-spline functions can be used to define exactly geometries from conic sections with as few parameters as possible. A rational B-spline curve in  $\mathbb{R}^{n_{sd}}$  is defined as follows.

$$C(\xi) = \sum_{i=1}^n B_i R_{i,p}(\xi) \quad (4.45)$$

where

$$R_{i,p}(\xi) = \frac{N_{i,p}(\xi) w_i}{\sum_{j=1}^n N_{j,p}(\xi) w_j} \quad (4.46)$$

is the  $i^{th}$  rational B-spline basis function of degree  $p$  corresponding to control point  $B_i \in \mathbb{R}^{n_{sd}}$  and weight  $w_i$  for a knot vector  $\Xi = \{\xi_i\}_{i=1}^{n+p+1}$ . Equations (4.40) through (4.43) for  $h$ -refinement or  $p$ -refinement should be applied to weighted control points defined as follows.

$$B_i^w = (w_i B_i^1, w_i B_i^2, \dots, w_i B_i^{n_{sd}}, w_i), \quad i = 1, 2, \dots, n \quad (4.47)$$

where the superscript  $j$  in  $B_i^j$  denotes the components of the vector  $B_i$ . When rational B-splines are defined in a knot vector that is non-uniform and open, then it is called as non-uniform rational B-splines (NURBS). Higher dimensional NURBS are defined by taking tensor product of one-dimensional NURBS similar to section 4.2.5. For a detailed description on how to obtain control points and control net for different geometries please refer Hughes *et al.* [46] and Piegl and Tiller [60].

**Remark 4.22:** *All the properties applicable to B-splines discussed in section 4.2 are also applicable for NURBS.*

**Remark 4.23:** *The unknown degrees of freedom are called as control variables and have the same properties as that of control points or control net depending on the dimension of physical domain.*

**Remark 4.24:** *B-splines are a special case of NURBS functions where the weights are unity.*

### 4.3 Numerical Results

#### 4.3.1 Kronig-Penney problem (3D case)

We present the convergence study for the 3D generalized Kronig-Penney problem. The domain under consideration is a cube with electronic potential given by

$$V(\mathbf{x}) = V_{1D}(x) + V_{1D}(y) + V_{1D}(z) \quad \text{in } \Omega \quad (4.48)$$

where

$$V_{1D}(s) = \begin{cases} 0 & 0 \leq s < 2 \text{ a.u.} \\ 6.5 \text{ Ry} & 2 \leq s < 3 \text{ a.u.} \end{cases}$$

For the three meshes employed for the convergence rate study, the knot vectors and weights for NURBS functions are given as follows. The control points are chosen in such a way that a uniform mesh is created in the physical domain, and the element boundaries are exactly conforming at 2 a.u. in all three directions.

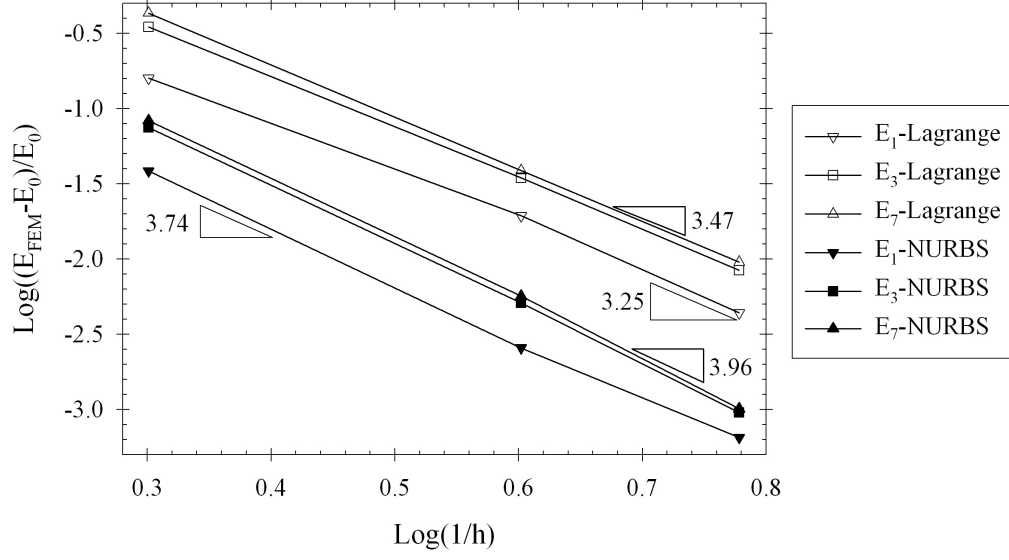


Figure 30. Convergence rates for second order NURBS

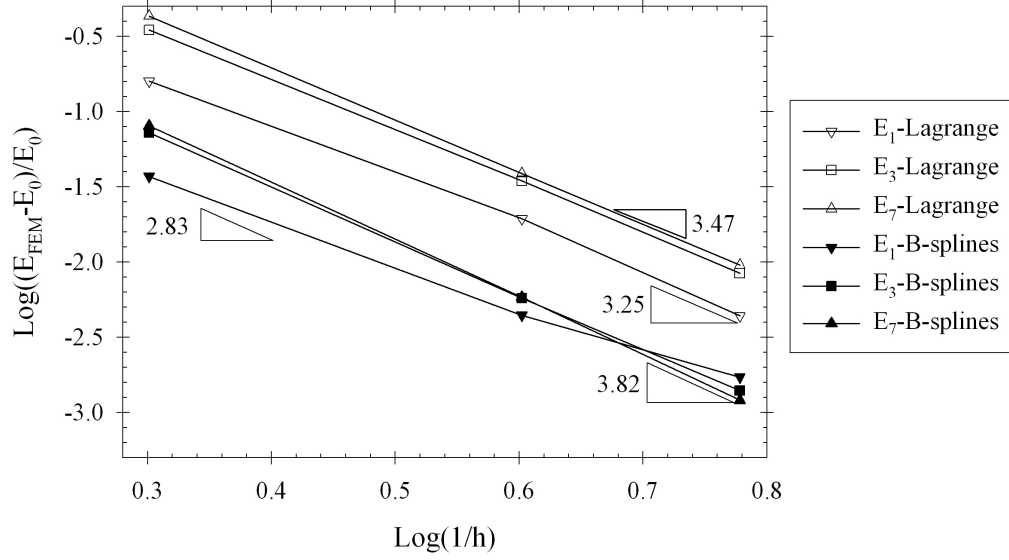


Figure 31. Convergence plots for second order B-Splines

1. **4<sup>3</sup> mesh**: Spline order  $p=2$ , uknot=(0,0,0,1,2,3,4,4,4) [same for other two directions] and weights of (1,1,1,2.365, 2.365, 2.365) for X-direction,
2. **8<sup>3</sup> mesh**: Spline order  $p=2$ , uknot=(0,0,0,1,2,3,4,5,6,7,8,8,8) [same for other two directions] and weights of (1,1,1,1,1, 2.365, 2.365, 2.365, 2.365, 2.365) for X-direction,
3. **12<sup>3</sup> mesh**: Spline order  $p=2$ , uknot=(0,0,0,1,2,3,4,5,6,7,8,9,10,11,12,12,12) [same for other two directions] and weights of (1,1,1,1,1,1,1, 2.365, 2.365, 2.365, 2.365, 2.365, 2.365,2.365) for X-direction,

For the case of B-splines, the weights are all unity, while the knot vectors are chosen to be same as above. For cubic NURBS, knot vectors and weights are chosen in an analogous fashion as described above. Figures 30 and 31 present convergence rates for the fractional error in the first, third and seventh eigenvalues for the Galerkin method with quadratic NURBS and quadratic B-spline basis functions. The results are compared to quadratic Lagrange basis functions. Theoretical convergence rates for the eigenvalues in the  $L_2$  type norm for linear and quadratic elements is  $p + 1$ , where  $p$  is the order for the interpolation of the complex valued wavefunction  $v(\mathbf{x})$ . Computed rates corroborate the theoretical predictions [54] for NURBS, B-spline and Lagrange basis functions. In each of the test cases the normalized error in the computed eigenvalues is smallest for the first eigenvalue and it successively increases for the higher eigenvalues. However it is important to note that the absolute error for the B-splines and NURBS is consistently lower than that of the corresponding Lagrange basis functions [62]. This is attributed to the  $C^1$  continuity of the B-spline and NURBS basis functions as opposed to  $C^0$  continuity of Lagrange functions. Figure 32 represents the energy band diagram for

quadratic B-spline function of  $8^3$  mesh resolution. Computed eigenvalues are plotted against exact eigenvalues computed from a non-linear analytical function [54].

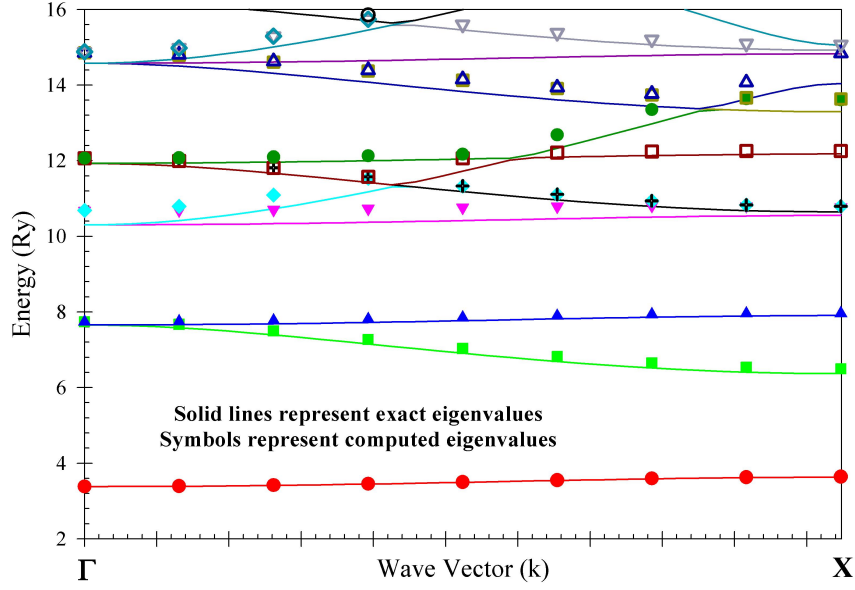


Figure 32. Energy band diagram for quadratic B-splines with mesh  $8^3$  mesh

### 4.3.2 Poisson problem

#### 4.3.2.1 Test problem

In this problem we study the Poisson problem for a given analytical potential for various order B-splines. The analytical potential is given by

$$V = \sin(2\pi x) \sin(2\pi y) \sin(2\pi z) \quad (4.49)$$

The corresponding forcing function,  $f(x, y, z)$ , is given by the Laplacian of the potential as shown in (4.50).

$$f(x, y, z) = -12\pi^2 \sin(2\pi x) \sin(2\pi y) \sin(2\pi z) \quad (4.50)$$

The domain under consideration is a unit cube, where periodic boundary condition is applied on corresponding surfaces. Four uniform meshes composed of  $4^3$ ,  $6^3$ ,  $8^3$  and  $12^3$  elements for B-spline order 2, 3 and 4 are considered. In the legend, the numbers in brackets denote the number of degrees of freedom per direction along the three lattice vectors for the corresponding meshes and polynomial orders. Figures 33 (a-c) are plots of the potential along body diagonal for  $p = 2, 3, 4$ .

The plots of error in potential along body diagonal are shown in Figures 34 (a-c). Even for the crudest mesh, it can be seen that there is one order reduction in error for one order increase in polynomial order. Figure 35 shows the normalized  $L_2$  norm of the error in the computed potential as a function of mesh refinement. Here normalization is with respect to the  $L_2$  norm of the analytical potential in equation (4.49). We obtain optimal convergence rates in each of the cases.

**Remark 4.25:** *As discussed in section 4.2.4, the  $h$ -refinement process was carried out according to equations (4.40), (4.41) for each polynomial order to obtain uniform mesh.  $k$ -refinement is utilized for increasing the polynomial order.*

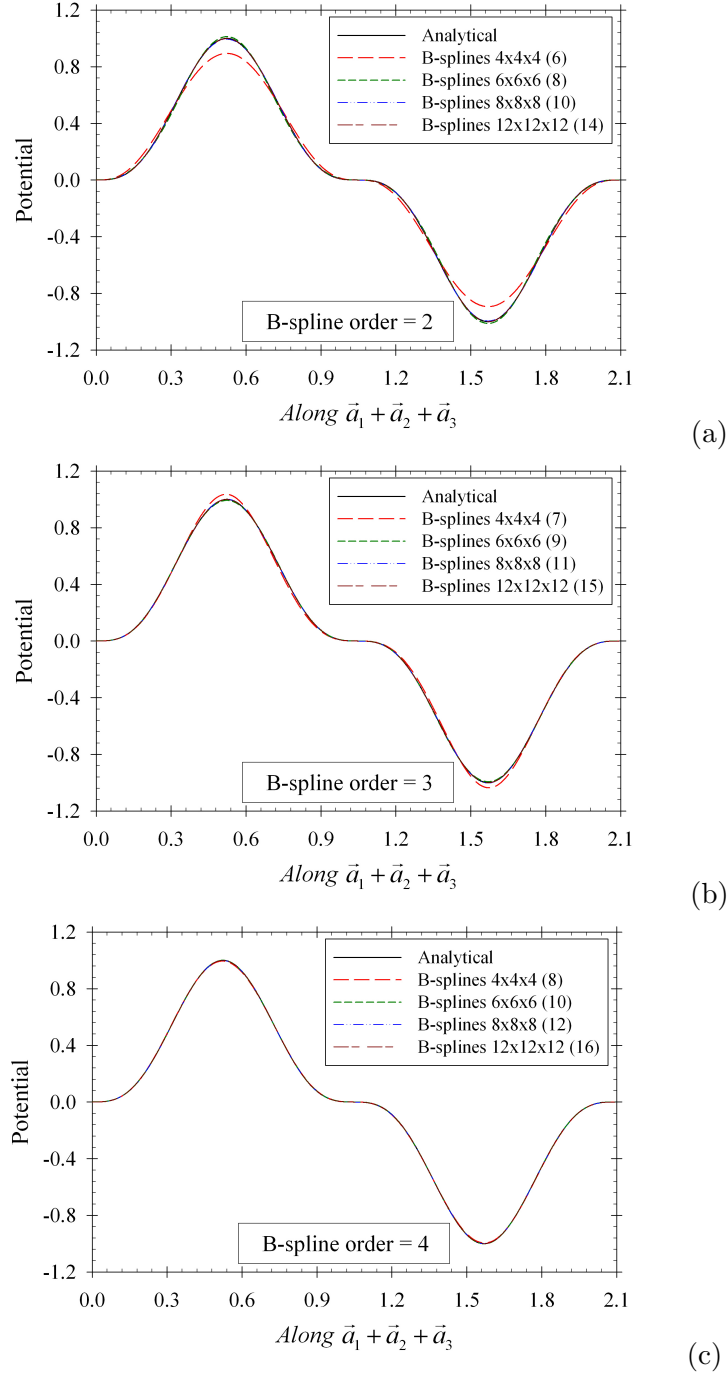


Figure 33. Plot of the potential along the body diagonal (a)  $p = 2$ , (b)  $p = 3$ , (c)  $p = 4$

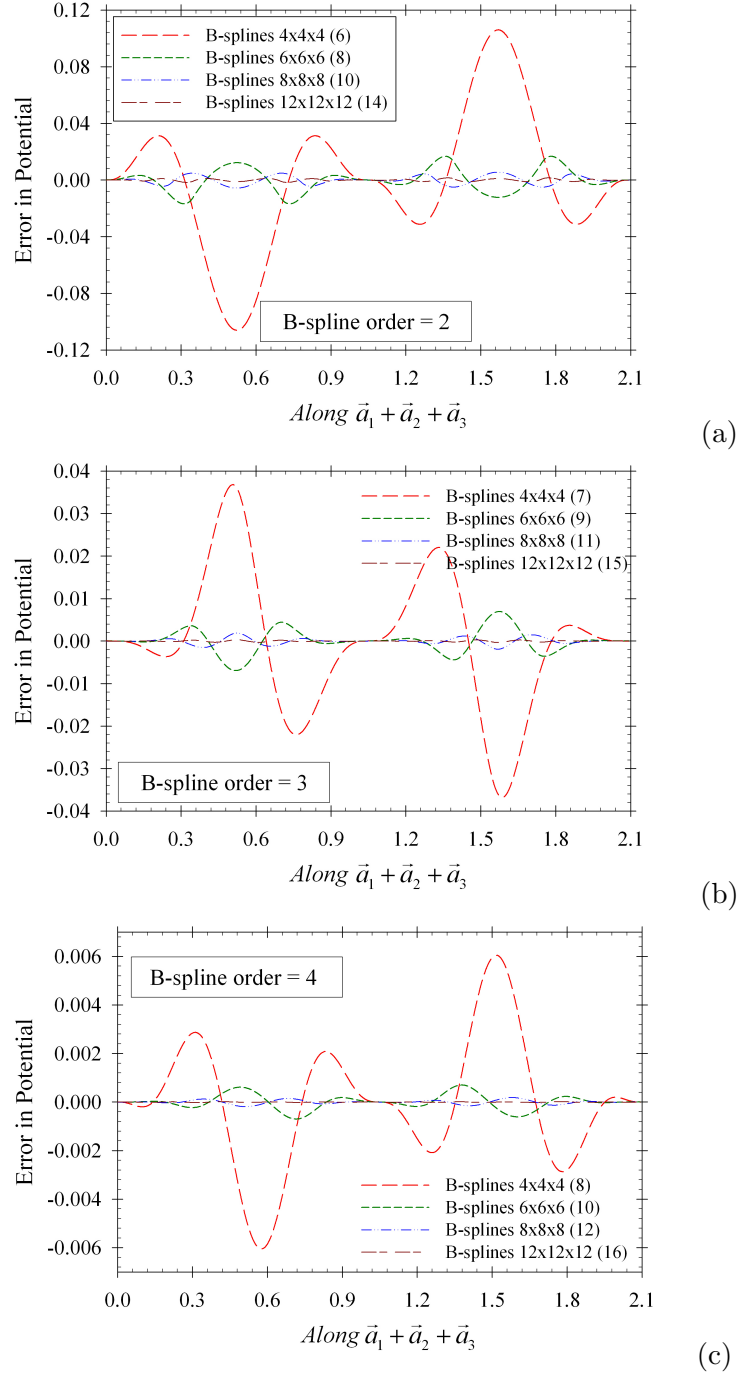


Figure 34. Error in the potential along the body diagonal (a)  $p = 2$ , (b)  $p = 3$ , (c)  $p = 4$



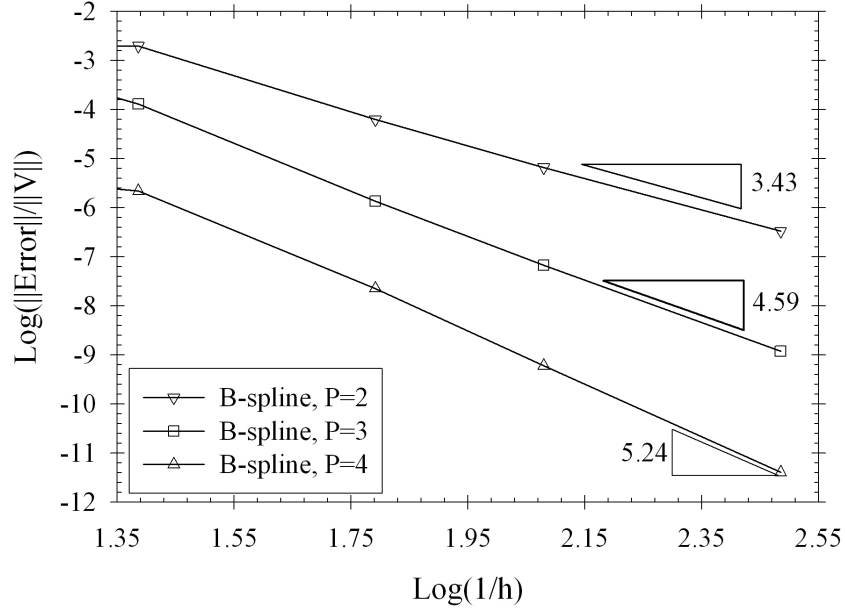


Figure 35. Convergence rates for the Poisson problem with analytical potential,

$$V = \sin(2\pi x) \sin(2\pi y) \sin(2\pi z)$$

#### 4.3.2.2 Triclinic model

Here we show the results for model triclinic charge density. The domain or unit cell is defined by the following primitive lattice vectors.

$$\mathbf{a}_1 = (1.0, 0.0, 0.0), \mathbf{a}_2 = (0.1, 1.0, 0.0), \mathbf{a}_3 = (0.2, 0.3, 1.0) \quad (4.51)$$

and the source term is defined as

$$f = \sum_{\mathbf{G}} \mathbf{G}^2 (a_{\mathbf{G}} \cos \mathbf{G} \cdot \mathbf{x} + b_{\mathbf{G}} \sin \mathbf{G} \cdot \mathbf{x}), \quad (4.52)$$

with the reciprocal lattice vectors  $\mathbf{G}$  and constants  $a_{\mathbf{G}}$  and  $b_{\mathbf{G}}$  being defined as shown in Table

I. The corresponding analytical solution is

$$V = \sum_{\mathbf{G}} a_{\mathbf{G}} \cos \mathbf{G} \cdot \mathbf{x} + b_{\mathbf{G}} \sin \mathbf{G} \cdot \mathbf{x} \quad (4.53)$$

| $\mathbf{G}$ | $a_{\mathbf{G}}$ | $b_{\mathbf{G}}$ |
|--------------|------------------|------------------|
| (1, 0, 0)    | 0.5              | 0.90             |
| (0, 1, 0)    | 0.45             | 0.85             |
| (0, 0, 1)    | 0.40             | 0.80             |
| (1, 1, 0)    | 0.35             | 0.75             |
| (0, 1, 1)    | 0.30             | 0.70             |
| (1, 0, 1)    | 0.25             | 0.65             |
| (1, 1, 1)    | 0.20             | 0.60             |
| (2, 1, 0)    | 0.15             | 0.55             |
| (0, 2, 1)    | 0.10             | 0.50             |
| (1, 0, 2)    | 0.05             | 0.45             |

TABLE I

SOURCE PASK *ET AL.* [1]. THE RECIPROCAL LATTICE VECTOR  $\mathbf{G}$  IS DEFINED IN TERMS OF PRIMITIVE RECIPROCAL LATTICE VECTORS  $\mathbf{B}_1$ ,  $\mathbf{B}_2$  AND  $\mathbf{B}_3$

Mesh refinement (i.e.  $h$ -refinement) and degree elevation (i.e.  $k$ -refinement) are done the same way as discussed for the previous problem and according to discussions in section 4.2.4. In the present problem the solution changes more rapidly with spatial co-ordinates. So the results accordingly vary for  $h$ -refinement and  $k$ -refinement. Figures 36 (a-c) show the plots of potential along body diagonal, for orders  $p = 2, 3, 4$  respectively. Figures 37 (a-c) show the plots of error in potential for different order B-spline basis functions.

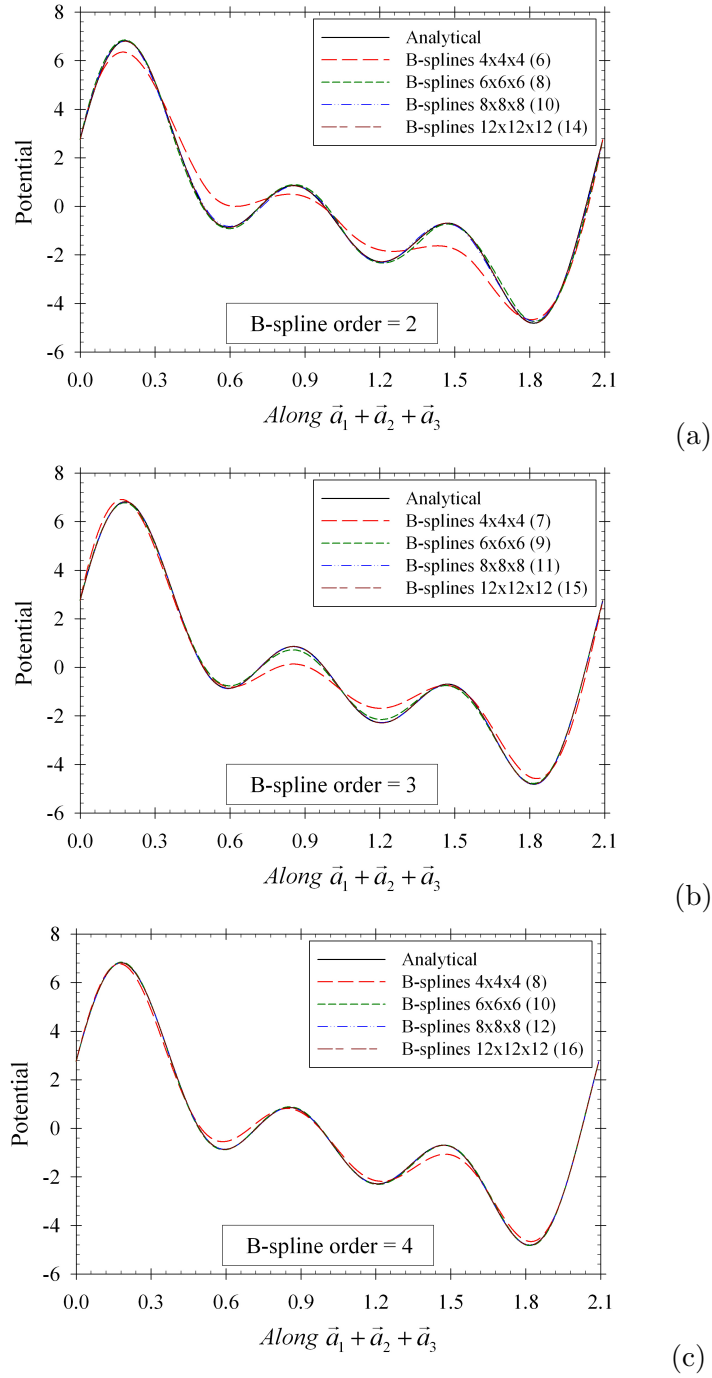


Figure 36. Plot of the potential along the body diagonal for triclinic model (a)  $p=2$ , (b)  $p=3$ ,

(c)  $p=4$

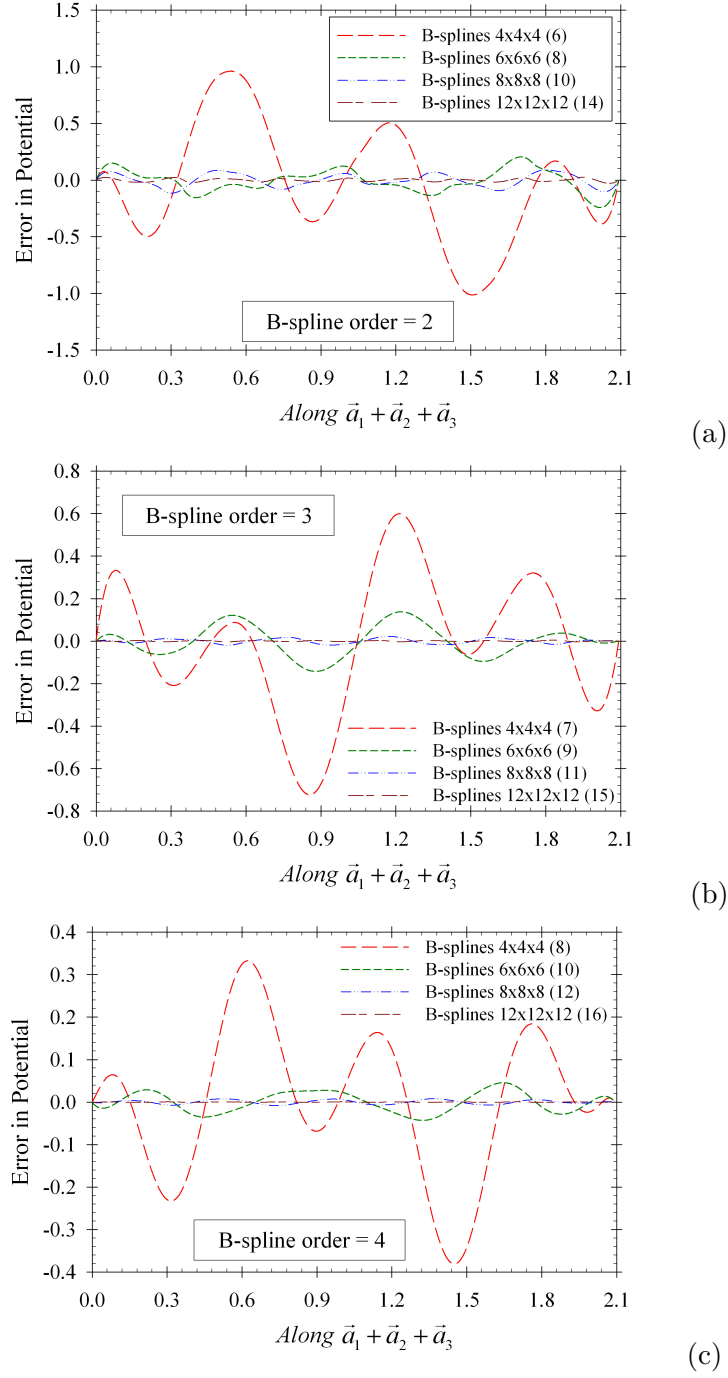


Figure 37. Error in the potential along the body diagonal for triclinic model (a)  $p=2$ , (b)

$p=3$ , (c)  $p=4$

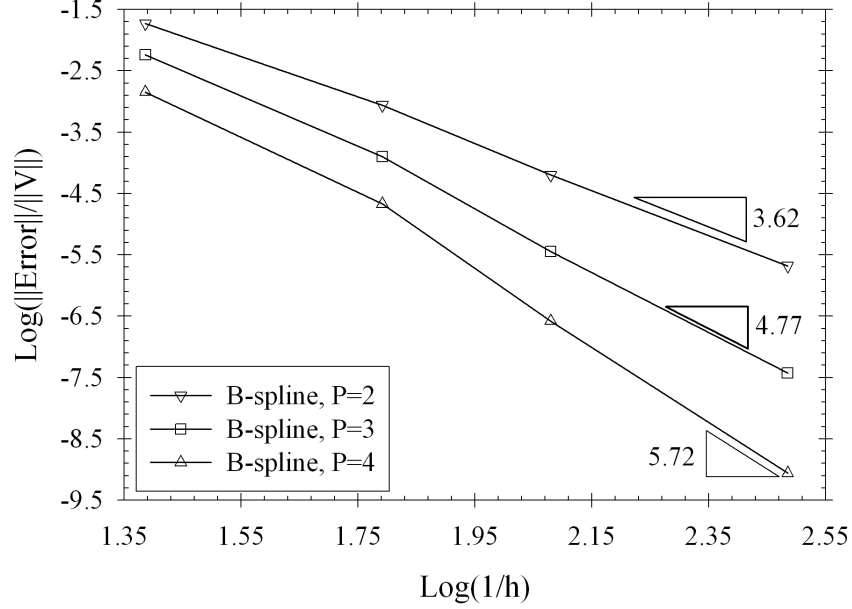


Figure 38. Convergence rates for the triclinic model

Convergence rates are plotted in Figure 38, where normalized  $L_2$  norm of the error in the computed potential is plotted as a function of mesh refinement. Here too normalization is with respect to the  $L_2$  norm of the analytical potential in equation (4.50). We see a reduction in error by one order only for meshes  $8^3$  or higher with the increasing polynomial order. In Table I, the reciprocal lattice vector  $\mathbf{G}$  is defined in terms of primitive lattice vectors  $\mathbf{b}_1$ ,  $\mathbf{b}_2$  and  $\mathbf{b}_3$ . For example (1, 0, 2) implies  $\mathbf{G} = \mathbf{b}_1 + 2\mathbf{b}_3$ . The reciprocal lattice vectors are defined as follows.

$$\mathbf{b}_1 = 2\pi (\mathbf{a}_2 \times \mathbf{a}_3) / (\mathbf{a}_1 \bullet (\mathbf{a}_2 \times \mathbf{a}_3)) = (2\pi, -0.2\pi, -0.34\pi) \quad (4.54)$$

$$\mathbf{b}_2 = 2\pi (\mathbf{a}_3 \times \mathbf{a}_1) / (\mathbf{a}_2 \bullet (\mathbf{a}_3 \times \mathbf{a}_1)) = (0, 2\pi, -0.6\pi) \quad (4.55)$$

$$\mathbf{b}_3 = 2\pi (\mathbf{a}_1 \times \mathbf{a}_2) / (\mathbf{a}_3 \bullet (\mathbf{a}_1 \times \mathbf{a}_2)) = (0, 0, 2\pi) \quad (4.56)$$

#### 4.3.2.3 Silicon empirical pseudopotential

Silicon empirical pseudo-potential of Cohen and Bergstresser [63] is based on FCC unit cell. Here we show the results for model silicon charge density. The domain or unit cell is defined by the following primitive lattice vectors.

$$\mathbf{a}_1 = (0, a/2, a/2), \mathbf{a}_2 = (a/2, 0, a/2), \mathbf{a}_3 = (a/2, a/2, 0) \quad (4.57)$$

where lattice constant  $a = 10.261 \text{ a.u.}$  and the source term is defined as

$$f = \sum_{\mathbf{G}} G^2 S_{\mathbf{G}} V_{\mathbf{G}} e^{-i\mathbf{G} \cdot \mathbf{x}} \quad (4.58)$$

with the reciprocal lattice vectors  $\mathbf{G}$  being defined as shown in Table II. The constants  $S_{\mathbf{G}}$  and  $V_{\mathbf{G}}$  are defined as follows.

$$S_{\mathbf{G}} = \cos \mathbf{G} \cdot \boldsymbol{\tau} \quad (4.59)$$

$$\boldsymbol{\tau} = (1, 1, 1) \frac{a}{8} \quad (4.60)$$

$$V_{\mathbf{G}} = \left\{ \begin{array}{ll} -0.21, & |\mathbf{G}|^2 = 3(2\pi/a)^2 \\ +0.04, & |\mathbf{G}|^2 = 8(2\pi/a)^2 \\ +0.08, & |\mathbf{G}|^2 = 11(2\pi/a)^2 \\ 0, & otherwise \end{array} \right\} \quad (4.61)$$

The corresponding analytical solution is

$$V = \sum_{\mathbf{G}} S_{\mathbf{G}} V_{\mathbf{G}} e^{-i\mathbf{G} \cdot \mathbf{x}} \quad (4.62)$$

In the present problem the solution changes more rapidly (than in the two previous problems) with spatial co-ordinates. So the results accordingly vary for  $h$ -refinement and  $k$ -refinement

as the number of control variables required to capture solution with precision is more. Figures 39 (a-c) show the plots of potential along body diagonal, for orders  $p = 2, 3, 4$  respectively. Figures 40 (a-c) show the plots of error in potential for different order B-spline basis functions.

|                |                |                |               |
|----------------|----------------|----------------|---------------|
| $(-2, -2, -1)$ | $(-2, -1, -2)$ | $(-2, -1, -1)$ | $(-2, -1, 0)$ |
| $(-2, 0, -1)$  | $(-1, -2, -2)$ | $(-1, -2, -1)$ | $(-1, -2, 0)$ |
| $(-1, -1, -2)$ | $(-1, -1, -1)$ | $(-1, -1, 1)$  | $(-1, 0, -2)$ |
| $(-1, 0, 0)$   | $(-1, 0, 1)$   | $(-1, 1, -1)$  | $(-1, 1, 0)$  |
| $(-1, 1, 1)$   | $(0, -2, -1)$  | $(0, -1, -2)$  | $(0, -1, 0)$  |
| $(0, -1, 1)$   | $(0, 0, -1)$   | $(0, 0, 1)$    | $(0, 1, -1)$  |
| $(0, 1, 0)$    | $(0, 1, 2)$    | $(0, 2, 1)$    | $(1, -1, -1)$ |
| $(1, -1, 0)$   | $(1, -1, 1)$   | $(1, 0, -1)$   | $(1, 0, 0)$   |
| $(1, 0, 2)$    | $(1, 1, -1)$   | $(1, 1, 1)$    | $(1, 1, 2)$   |
| $(1, 2, 0)$    | $(1, 2, 1)$    | $(1, 2, 2)$    | $(2, 0, 1)$   |
| $(2, 1, 0)$    | $(2, 1, 1)$    | $(2, 1, 2)$    | $(2, 2, 1)$   |

TABLE II

THE RECIPROCAL LATTICE VECTOR  $\mathbf{G}$  IS DEFINED IN TERMS OF PRIMITIVE  
 RECIPROCAL LATTICE VECTORS  $\mathbf{B}_1$ ,  $\mathbf{B}_2$  AND  $\mathbf{B}_3$  [2]

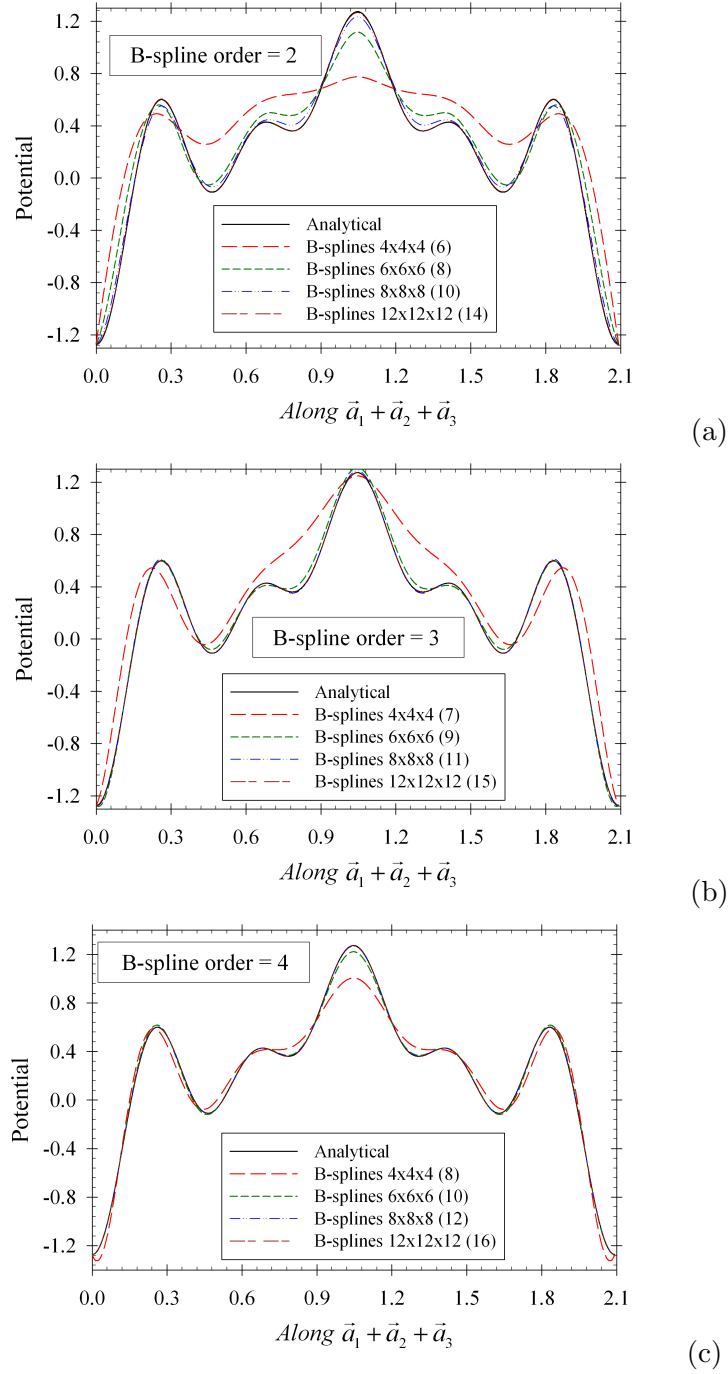


Figure 39. Plot of the potential along the body diagonal for silicon empirical pseudo-potential

(a)  $p = 2$ , (b)  $p = 3$ , (c)  $p = 4$



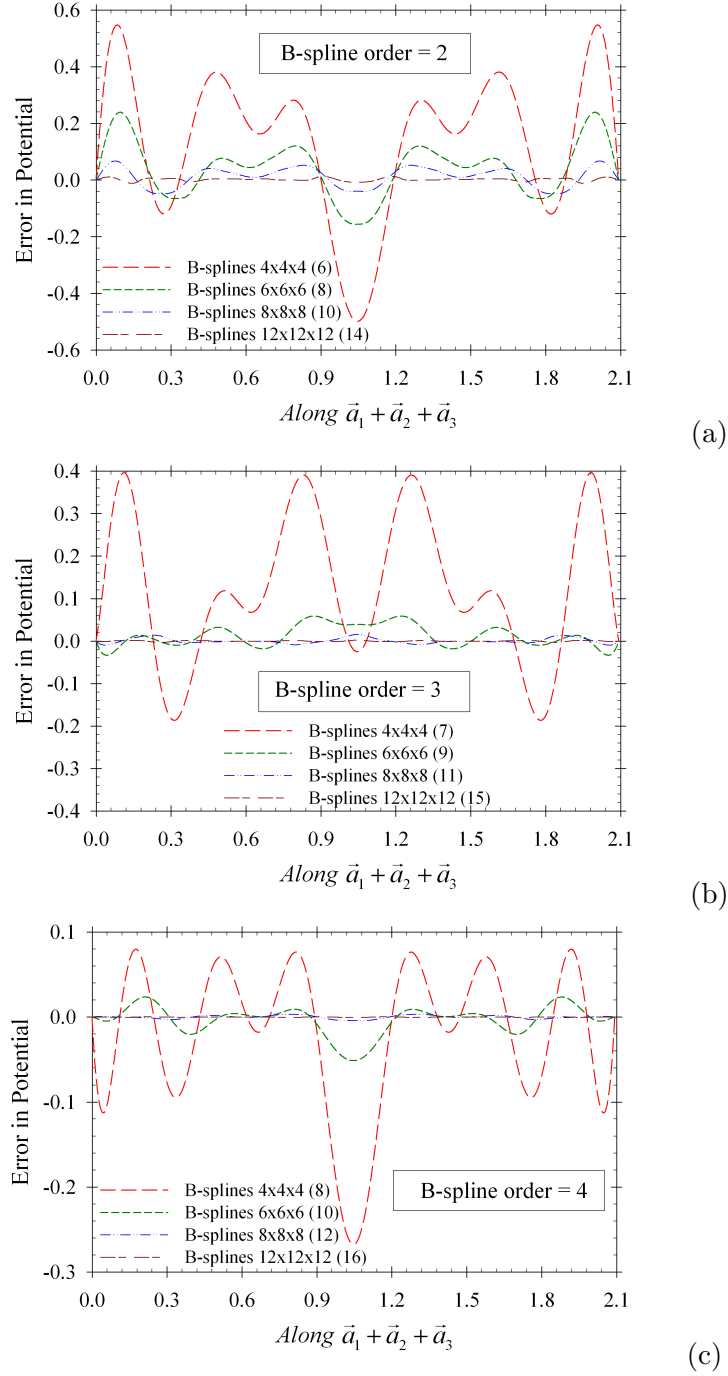


Figure 40. Error in the potential along the body diagonal for silicon empirical

pseudo-potential (a)  $p = 2$ , (b)  $p = 3$ , (c)  $p = 4$

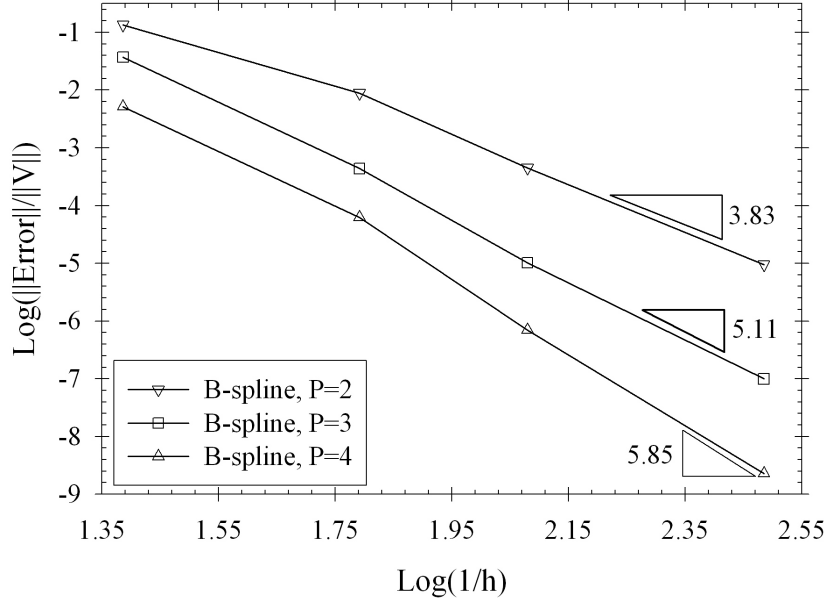


Figure 41. Convergence rates for the silicon empirical pseudo-potential

Convergence rates are plotted in Figure 41, where normalized  $L_2$  norm of the error in the computed potential is plotted as a function of mesh refinement. Here normalization is done with respect to the  $L_2$  norm of the analytical potential in equation (4.59). We see a reduction in the error by one order only for meshes  $6^3$  or higher with the increase in the polynomial order.

In Table II, the reciprocal lattice vector  $\mathbf{G}$  is defined in terms of primitive lattice vectors  $\mathbf{b}_1$ ,  $\mathbf{b}_2$  and  $\mathbf{b}_3$ . For example  $(-2, -2, -1)$  implies  $\mathbf{G} = -2\mathbf{b}_1 - 2\mathbf{b}_2 - \mathbf{b}_3$ . The reciprocal lattice vectors are defined as follows.

$$\mathbf{b}_1 = 2\pi (\mathbf{a}_2 \times \mathbf{a}_3) / (\mathbf{a}_1 \bullet (\mathbf{a}_2 \times \mathbf{a}_3)) = (-0.1949\pi, 0.1949\pi, 0.1949\pi) \quad (4.63)$$

$$\mathbf{b}_2 = 2\pi (\mathbf{a}_3 \times \mathbf{a}_1) / (\mathbf{a}_2 \bullet (\mathbf{a}_3 \times \mathbf{a}_1)) = (0.1949\pi, -0.1949\pi, 0.1949\pi) \quad (4.64)$$

$$\mathbf{b}_3 = 2\pi (\mathbf{a}_1 \times \mathbf{a}_2) / (\mathbf{a}_3 \bullet (\mathbf{a}_1 \times \mathbf{a}_2)) = (0.1949\pi, 0.1949\pi, -0.1949\pi) \quad (4.65)$$

### 4.3.3 Schrödinger equation: Silicon empirical pseudopotential

This test case is a continuation of test case in section 4.3.2.3. The primitive unit cell is defined in equation (4.57). The solution of Poisson problem corresponding to  $20^3$  mesh with the forcing function in equation (4.58) is employed to compute the analytical pseudo-potential in equation (4.62) to drive the SWE. We used the numerical solution from Poisson problem to simulate the self-consistent method, where Poisson problem and SWE are solved self-consistently, instead of using directly the pseudo-potential in equation (4.62). Four meshes with  $4^3$ ,  $6^3$ ,  $8^3$  and  $12^3$  are employed for the mesh sensitivity study and the convergence rate study. We used quadratic and cubic B-splines for this study. In each study the underlying Poisson problem employed the corresponding order B-splines with the  $20^3$  mesh.

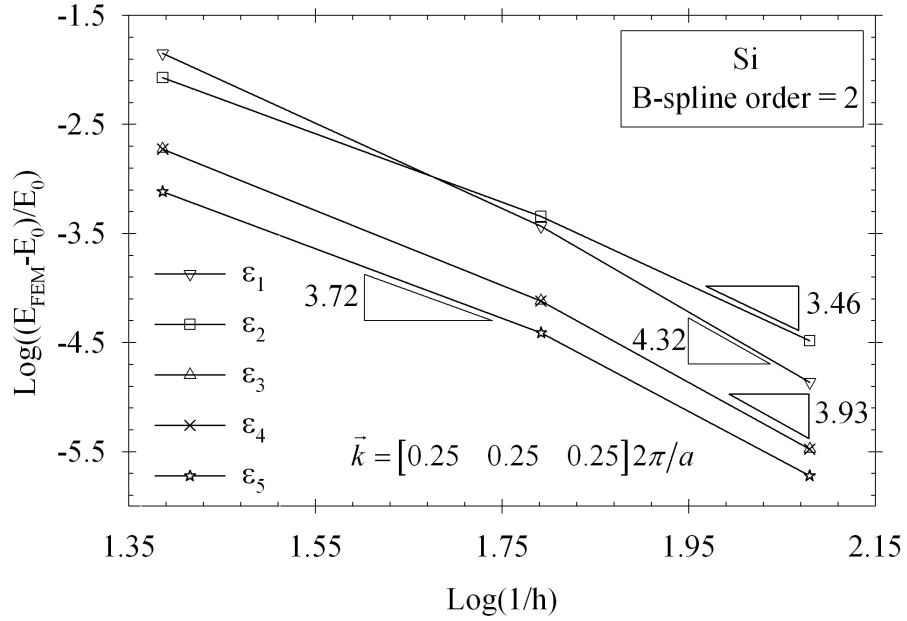


Figure 42. Convergence rates for the first five eigenvalues at a given  $\vec{k}$  point.

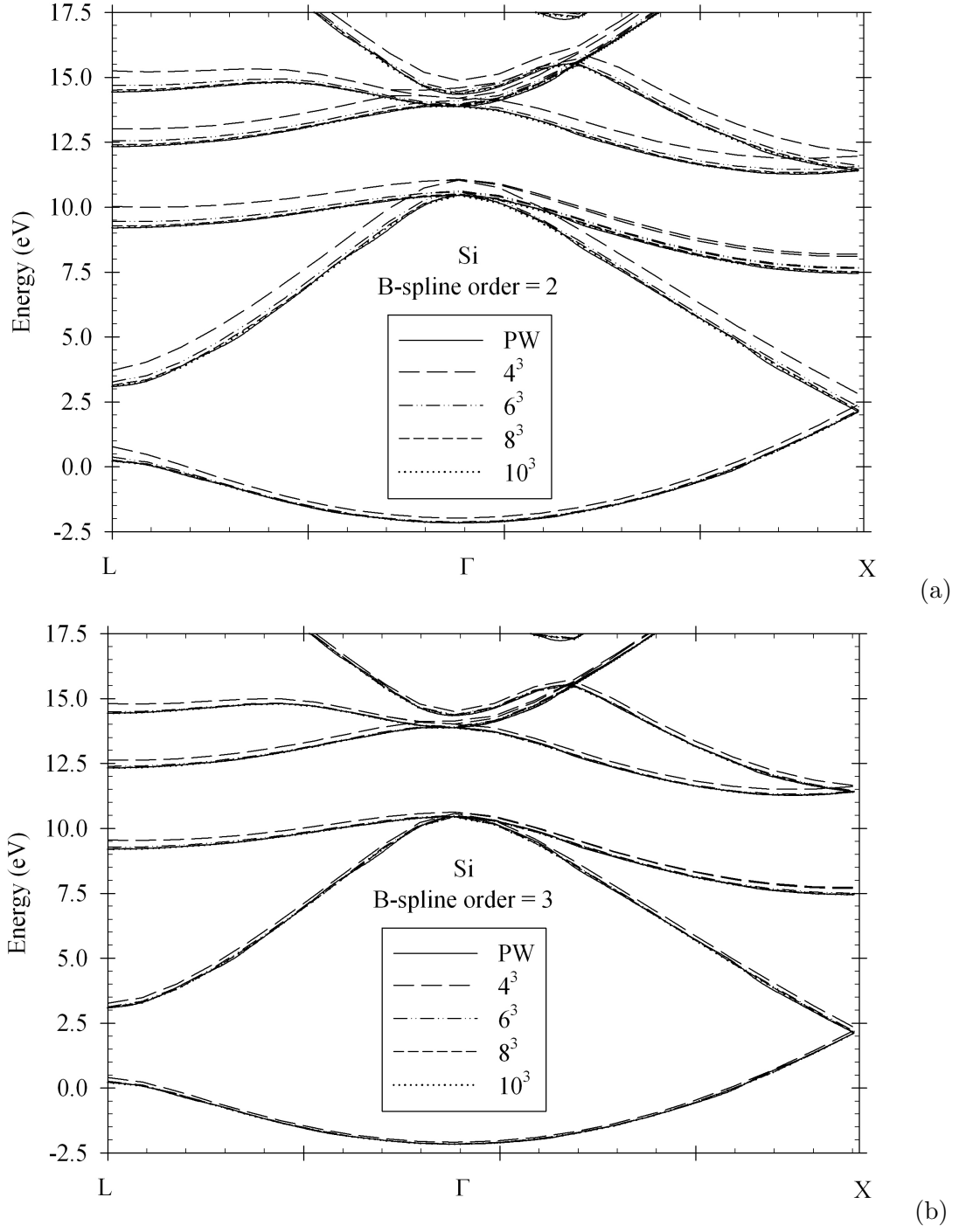


Figure 43. Band structure for silicon pseudo-potential (a)  $p = 2$ , (b)  $p = 3$

Accordingly, the solution from higher density mesh of the Poisson problem is projected onto lower density mesh of the SWE problem. Figures 43 (a-b) show the band structure for silicon pseudo-potential. In Figure 43 (a) it can be seen that as the mesh is refined the computed solution converges to the reference plane-wave solution [1].  $12^3$  mesh gives almost the same solution as that of plane-wave case. A similar trend is observed for cubic B-splines in Figure 43 (b), where rapid convergence is observed with  $8^3$  mesh resulting in almost matching solution as compared to the plane-wave case. Figure 42 shows the convergence rates for first five eigenvalues at a given  $\mathbf{k}$  point for quadratic B-splines. We get optimal convergence rates for the solution.

#### 4.3.4 Self-consistent study

We begin this study with one-dimensional case of isolated Indium atom. Then we discuss three-dimensional cases of bulk silicon, gallium Arsenide (GaAs) and graphene. Band diagram for bulk silicon and infinite graphene sheet are obtained by self-consistent solution procedure described in section 4.1 applied to periodic systems. HGH pseudopotential [4] is employed in both cases. As noted in section 4.1, we employ Pulay mixing scheme [55] and a history of five calculated densities from previous iterations to evaluate the new density. This procedure ensures convergence for fixed point iteration. Monkhorst-Pack algorithm [64] is employed for Brillouin zone integration.

Three different resolution meshes are used in the same domain, varying mesh resolution for Schrödinger equation, a fixed higher resolution mesh for Poisson problem and a equally spaced mesh for electron charge density, which is four times denser than the corresponding

mesh for Schrödinger equation. The electron charge densities are calculated at nodal points and interpolated at other spatial coordinates using equal order Lagrange basis functions. The solution from each mesh is projected onto other meshes at integration points in self-consistent procedure. Initial electron charge density can be obtained by superposition of electron charge densities of isolated atoms. This ensures faster convergence for bulk material.

#### 4.3.4.1 Indium atom with all electron potential (1D case)

In this case we used all electron potential of Indium atom . The following are the Kohn-Sham equations [61] that must be solved for this problem in a radial domain defined by interval  $[0, \xi]$ . Since this is a one-dimensional problem for an isolated atom we will be solving radial Schrödinger equation and Poisson problem in spherical coordinates with only the radial term.

$$\left[ -\frac{1}{2} \frac{d^2}{dr^2} + \frac{l(l+1)}{2r^2} + V(r) \right] R_{n,l}(r) = \varepsilon_{n,l} R_{n,l}(r) \quad (4.66)$$

$$\lim_{r \rightarrow 0} R_{n,l}(r) = \lim_{r \rightarrow \infty} R_{n,l}(r) = 0 \quad (4.67)$$

$$V(\mathbf{r}) = V_n + V_H + V_{XC} = -\frac{49}{r} + V_H + V_{XC} \quad (4.68)$$

$$V_H(\mathbf{r}) = \int \frac{\rho_e(\mathbf{r}')}{|\mathbf{r} - \mathbf{r}'|} d\mathbf{r}' = 4\pi \int_{r'=0}^{\infty} r'^2 \frac{\rho_e(r')}{|r - r'|} dr' \quad (4.69)$$

$$V_{XC} = V_{XC}(\mathbf{r}; \rho_e) \quad (4.70)$$

$$\rho_e(r) = \frac{1}{2\pi} \sum_{n,l} (2l+1) f_{n,l} \frac{R_{n,l}^2(r)}{r^2} \quad (4.71)$$

where  $R_{n,l}(r)$  is the radial wave-function,  $l$  stands for orbital angular momentum quantum number,  $n$  stands for principal quantum number,  $\varepsilon_{n,l}$  stands for eigenvalues,  $V_H$  for Hartree potential,  $V_{XC}$  for exchange-correlation potential and  $f_{n,l}$  for occupation number.

Since the electron charge density and Hartree terms are functions of radial co-ordinates only, the corresponding Poisson problem to be solved for obtaining the Hartree term is

$$\frac{d^2 U(r)}{dr^2} = -4\pi r \rho_e \quad (4.72)$$

where  $U(r) = rV_H(r)$  and boundary conditions are zero Dirichlet boundary conditions.

$$U(r)|_{r=0} = 0; \quad U(r)|_{r \rightarrow \infty} = 0 \quad (4.73)$$

We use Vosko-Wilk-Nusair (VWN) for obtaining correlation terms [65]. A logarithmic mesh is created along the radial direction by varying the control points as follows.

$$r_{\max} = 20; \quad \delta = \frac{10r_{\max}}{(10 + (6 - r_{\max})) 200} \quad (4.74)$$

$$r_p = \frac{r_{\max}}{e^{\delta(numel+p-1)} - 1}; \quad B_i = r_p \left( e^{(i-1)\delta} - 1 \right) \quad (4.75)$$

where  $numel$  stands for the number of elements along radial direction,  $B_i$  stands for the  $i^{th}$  control point and  $p$  stands for the B-spline order.

Once the electron charge density is calculated, the total energy  $E_t(\rho)$  can be calculated as follows [61].

$$E_t(\rho) = E_k(\rho) + E_n(\rho) + E_H(\rho) + E_{XC}(\rho) = \sum_i f_i \varepsilon_i + \int \tilde{V}(\mathbf{r}) \rho(\mathbf{r}) d\mathbf{r} \quad (4.76)$$

where  $E_k(\rho)$  is the kinetic energy,  $E_n(\rho)$  is the energy of electrostatic interaction with nuclei,  $E_H(\rho)$  is the Hartree energy and  $E_{XC}(\rho)$  is the exchange-correlation energy. The integrals extend over all space in three dimensions. These terms in summation are calculated as follows.

$$E_k(\rho) = \sum_i f_i \int \psi_i^*(\mathbf{r}) \left( -\frac{1}{2} \nabla^2 \right) \psi_i(\mathbf{r}) d\mathbf{r} = \sum_i f_i \varepsilon_i - \int V(\mathbf{r}) \rho(\mathbf{r}) d\mathbf{r} \quad (4.77)$$

where  $\psi_i(\mathbf{r}) = \psi_{n,l,m}(\mathbf{r}) = \frac{1}{r} R_{n,l}(r) Y_{l,m}(\theta, \phi)$  and  $Y_{l,m}(\theta, \phi)$  is spherical harmonics. Here  $\mathbf{r}$  represents position vector in three dimensional space and  $r$  represents radial distance from nucleus of an atom.

$$E_n(\rho) = \int V_n(\mathbf{r}) \rho(\mathbf{r}) d\mathbf{r} \quad (4.78)$$

$$E_H(\rho) = \frac{1}{2} \int \frac{\rho(\mathbf{r}) \rho(\mathbf{r}')}{|\mathbf{r} - \mathbf{r}'|} d\mathbf{r} d\mathbf{r}' = \frac{1}{2} \int V_H(\mathbf{r}) \rho(\mathbf{r}) d\mathbf{r} \quad (4.79)$$

$$E_{XC}(\rho) = \int \varepsilon_{XC}[\rho(\mathbf{r})] \rho(\mathbf{r}) d\mathbf{r} \quad (4.80)$$

$$\tilde{V}(\mathbf{r}) = \varepsilon_{XC} - V_{XC} - \frac{1}{2} V_H(\mathbf{r}) \quad (4.81)$$

Numerical results are given in Table III and Figures 44 through 48. The calculated values are compared with NIST values [61, 66–68] for Indium atom. B-splines of order 4 and order 6 were used with meshes varying from 50 elements to 400 elements. The various meshes are listed in Figure 44.

Table III shows the total energy calculated for fourth order B-spline basis functions with 200 and 400 elements as a function of  $\xi$ , where  $\xi$  defines the radial domain  $[0, \xi]$ . As the domain length increases and approaches 20 atomic units, the computed value for total energy,  $E_t(\rho)$ , approaches NIST value.

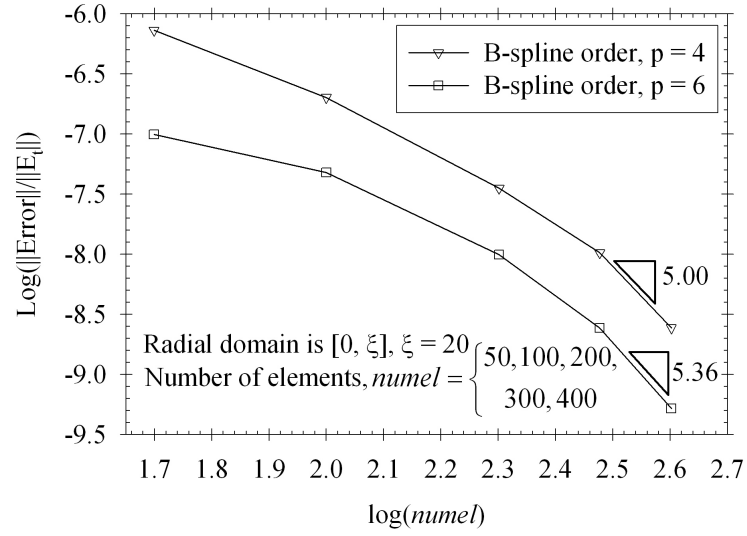
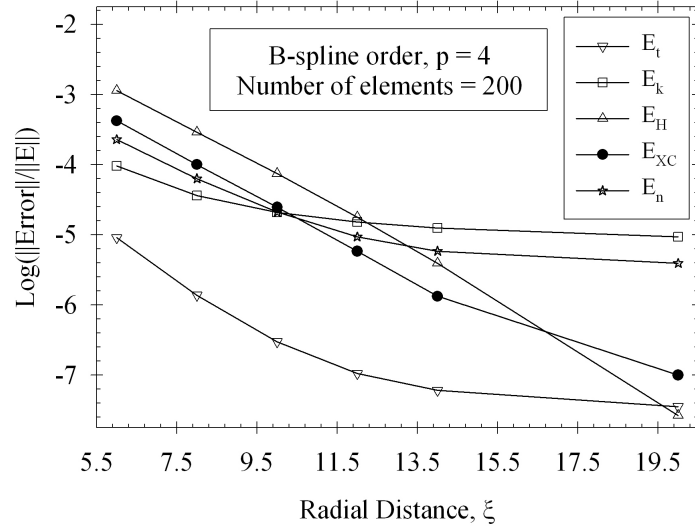


| $\xi$       | $numel = 200$ | $numel = 400$ |
|-------------|---------------|---------------|
| 6           | -5737.256830  | -5737.259150  |
| 8           | -5737.301165  | -5737.302151  |
| 10          | -5737.307346  | -5737.307900  |
| 12          | -5737.308460  | -5737.308833  |
| 14          | -5737.308716  | -5737.308999  |
| 20          | -5737.308860  | -5737.309046  |
| <b>NIST</b> | -5737.309064  | -5737.309064  |

TABLE III

TOTAL ENERGY FOR INDIUM ATOM FOR B-SPLINE ORDER K=4 AND MESH RESOLUTIONS N=200 AND N=400. IN COLUMN NIST REFERENCE VALUES ARE PROVIDED. ALL VALUES ARE IN HARTREE

Figures 45 and 46 show the convergence for total energy,  $E_t(\rho)$ , energy due to electron-nuclei interaction,  $E_n(\rho)$ , kinetic energy,  $E_k(\rho)$ , Hartree energy,  $E_H(\rho)$ , and exchange correlation energy,  $E_{XC}(\rho)$ , as a function of  $\xi$ . Figure 45 gives plots for fourth order B-spline with 200 element mesh, while Figure 46 presents plots for fourth order B-spline with 400 element mesh. We see errors in these energies,  $Error \rightarrow 0$  as  $\xi \rightarrow 20$ . Figures 47 and 48 are plots for total energy of individual orbitals of Indium atom as a function of  $\xi$  for fourth order B-splines with 200 and 400 element meshes respectively. Again we find convergence of energy values as  $\xi \rightarrow 20$ .

Figure 44. Convergence plot for  $E_t(\rho)$  as a function of  $numel$ Figure 45. Convergence plot for energies (equations 74-78) as a function of radial domain length,  $\xi$  for B-spline order  $p = 4$  and 200 elements

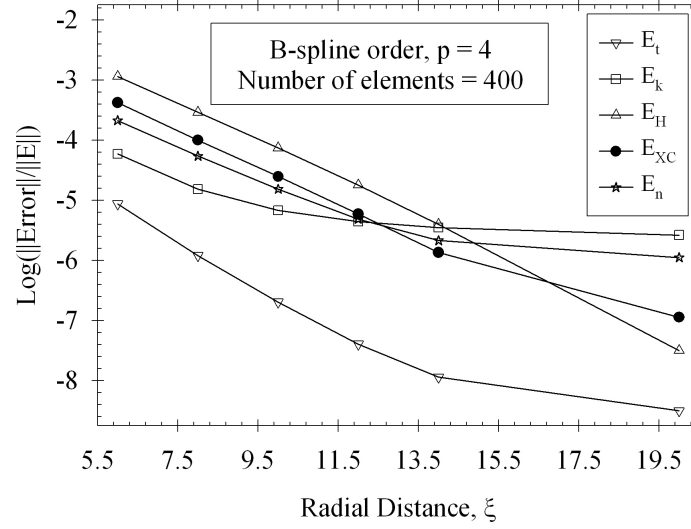


Figure 46. Convergence plot for energies (equations 74-78) as a function of radial domain length,  $\xi$  for B-spline order  $p = 4$  and 400 elements

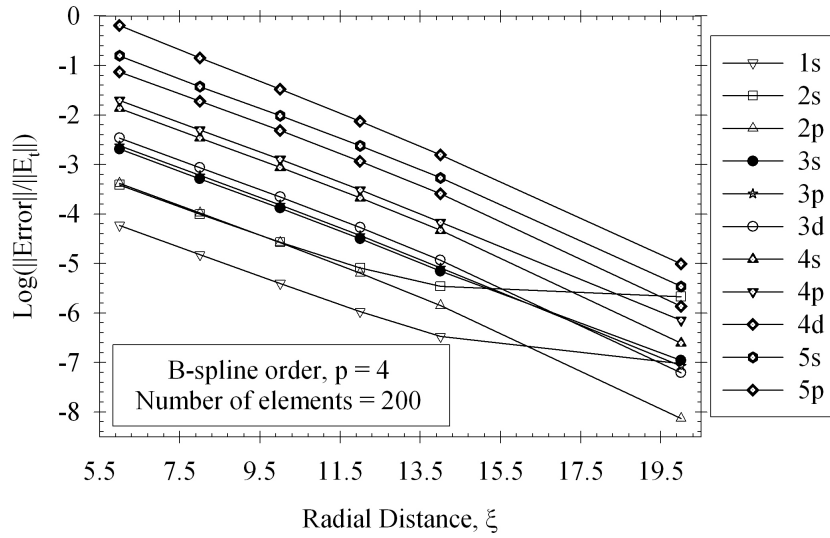


Figure 47. Convergence plot for total energies of each orbital as a function of radial domain length,  $\xi$  for B-spline order  $p = 4$  and 200 elements

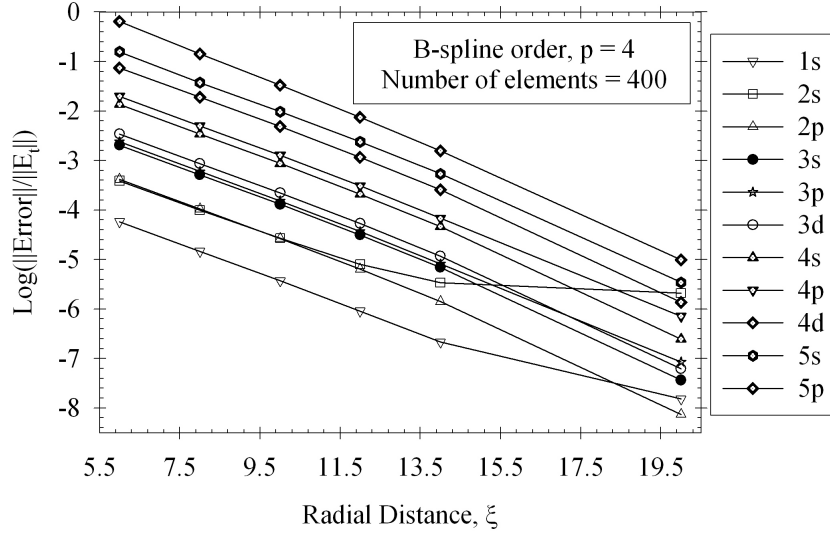


Figure 48. Convergence plot for total energies of each orbital as a function of radial domain length,  $\xi$  for B-spline order  $p = 4$  and 400 elements

Higher resolution mesh consistently gives better precision in computed values. This study presents data on number of B-splines basis functions required for single atom all-electron density functional theory calculations for required precision in results.

#### 4.3.4.2 Bulk silicon and self-consistent procedure

The primitive unit cell (FCC cubic structure) for bulk silicon is defined in section 4.3.2.3. A typical conventional unit cell and primitive unit cell is shown in Figure 49, while Figure 50 shows first Brillouin zone (reciprocal space) and its irreducible wedge for the corresponding primitive unit cell. The atomic positions are shown with each primitive cell containing two silicon atoms at positions  $(0, 0, 0)$  and  $(a/4, a/4, a/4)$ .

The high symmetry points of Brillouin zone are defined below.

$$\Gamma = (0, 0, 0); L = \frac{2\pi}{a} \left( \frac{1}{2}, \frac{1}{2}, \frac{1}{2} \right); K = \frac{2\pi}{a} \left( \frac{3}{4}, \frac{3}{4}, 0 \right);$$

$$X = \frac{2\pi}{a} (1, 0, 0); W = \frac{2\pi}{a} \left( 1, \frac{1}{2}, 0 \right); U = \frac{2\pi}{a} \left( 1, \frac{1}{4}, \frac{1}{4} \right)$$

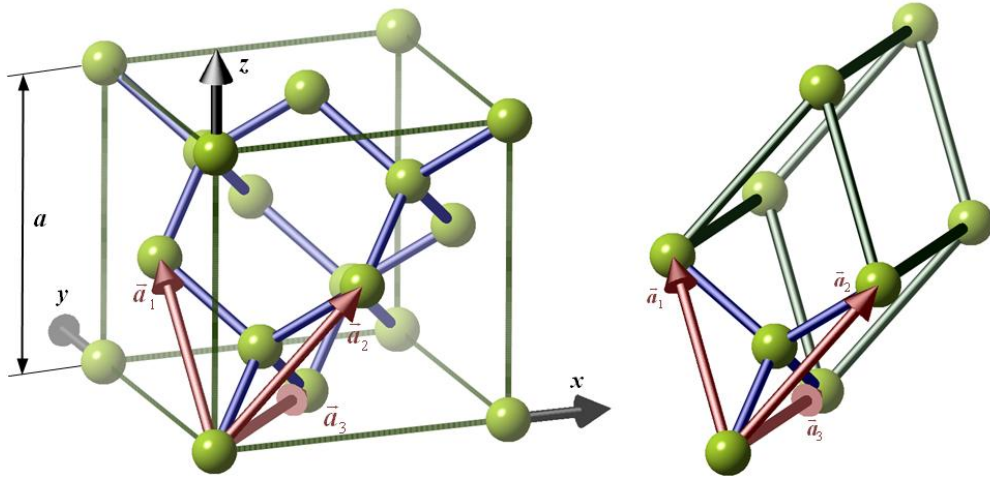


Figure 49. Conventional unit cell and Primitive unit cell.

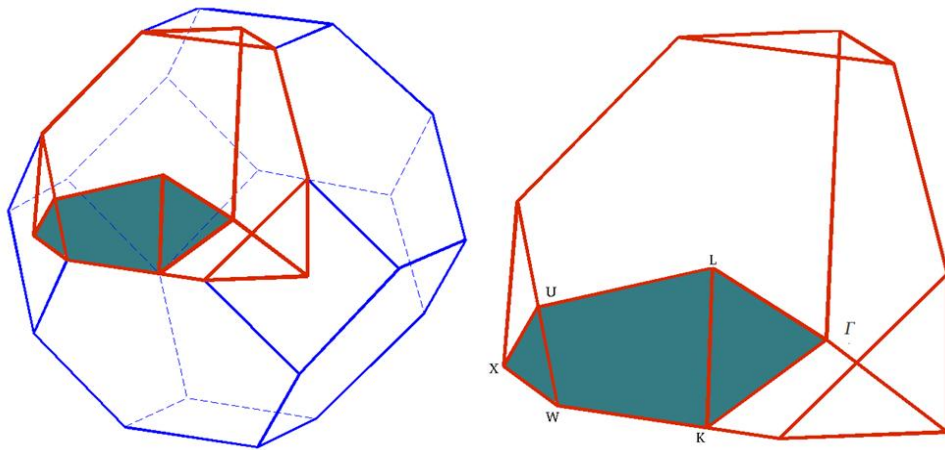


Figure 50. First Brillouin zone and irreducible wedge

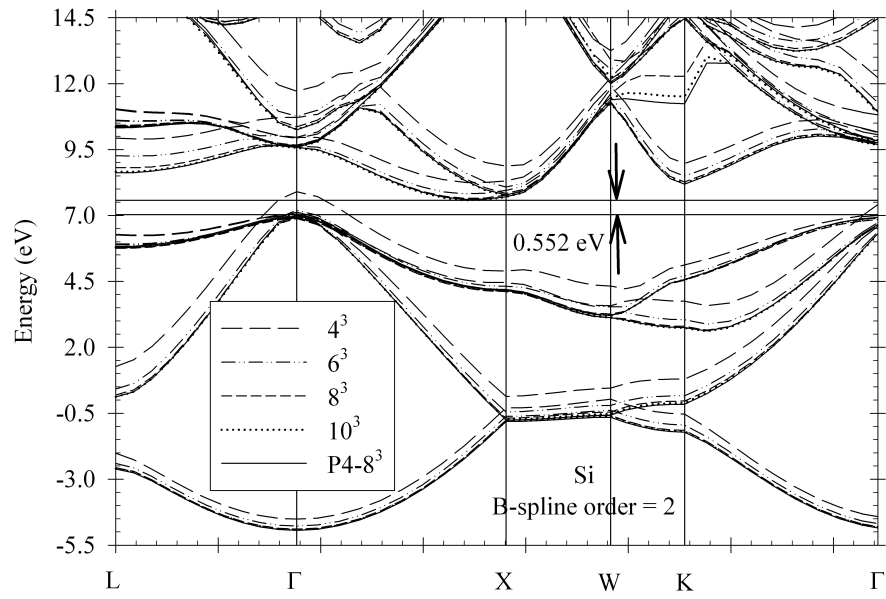


Figure 51. Band diagram for Bulk silicon and B-spline order  $p = 2$

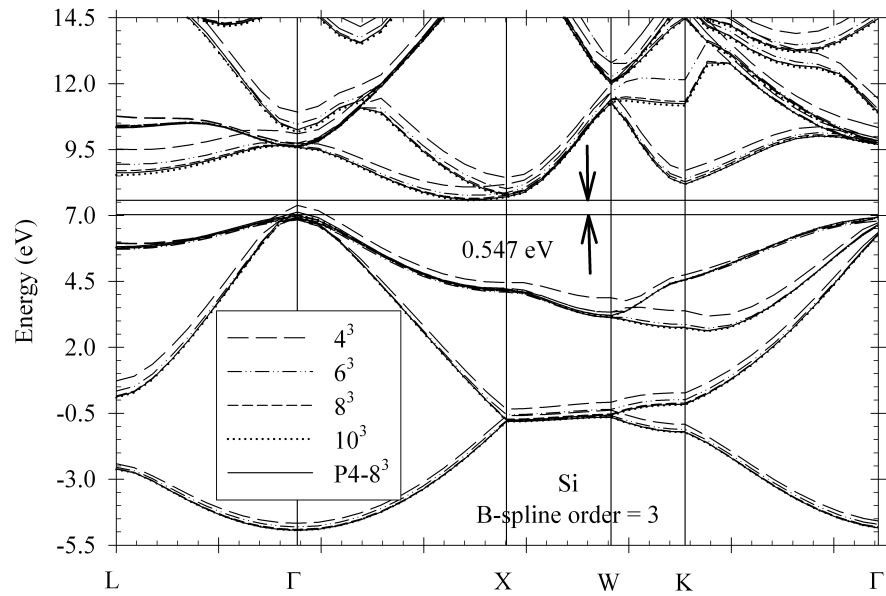


Figure 52. Band diagram for Bulk silicon and B-spline order  $p = 3$

Since the eigenfunctions are functions of wavevector  $\mathbf{k}$  after application of Bloch's theorem (section 4.1.1) the electronic charge density has to be evaluated by integrating in Brillouin zone. Equation (4.7) in section 4.1 transforms as follows.

$$n_{\mathbf{k}}(\mathbf{x}) = \sum_{i, \varepsilon_{i,\mathbf{k}} < \varepsilon_F} f_{i,\mathbf{k}} |\phi_{i,\mathbf{k}}(\mathbf{x})|^2$$

$$\rho_e(\mathbf{x}) = \frac{1}{\Omega_{BZ}} \int_{\Omega_{BZ}} n_{\mathbf{k}}(\mathbf{x}) d\mathbf{k} = \sum_{\mathbf{k}} \omega_{\mathbf{k}} n_{\mathbf{k}}(\mathbf{x})$$

where  $\Omega_{BZ}$  is the volume of the first Brillouin zone. Monkhorst-Pack algorithm [64] is used to numerically integrate the electron charge density in Brillouin zone. In the case of silicon, 44  $\mathbf{k}$  points in irreducible Brillouin zone were used to obtain electron charge density.

Figures 51 and 52 show the band diagram plots for second and third order B-spline basis functions along the symmetry points in Brillouin zone and the results are compared to fourth order B-spline solutions. HGH pseudopotentials [4] and Perdew-Zunger [69] exchange-correlation potential were used for the calculations. Optimal convergence rates are obtained as shown below. Experimentally silicon has 1.13 eV band gap. However the DFT method underestimates band gap below 0.6 eV. This is well known artifact of DFT calculations with LDA exchange-correlation functional.

#### 4.3.4.3 Gallium arsenide (GaAs)

GaAs has FCC cubic structure similar to Bulk silicon (Si). The primitive unit cell and Brillouin zone for GaAs is defined in a similar manner to bulk silicon. However in this case gallium atom is located at  $(0,0,0)$ , while Arsenic atom is located at  $(a/4, a/4, a/4)$ . The lattice constant for GaAs is  $a = 10.6831 \text{ a.u.}$  Brillouin zone integration was carried out with 44 integration points in irreducible part.

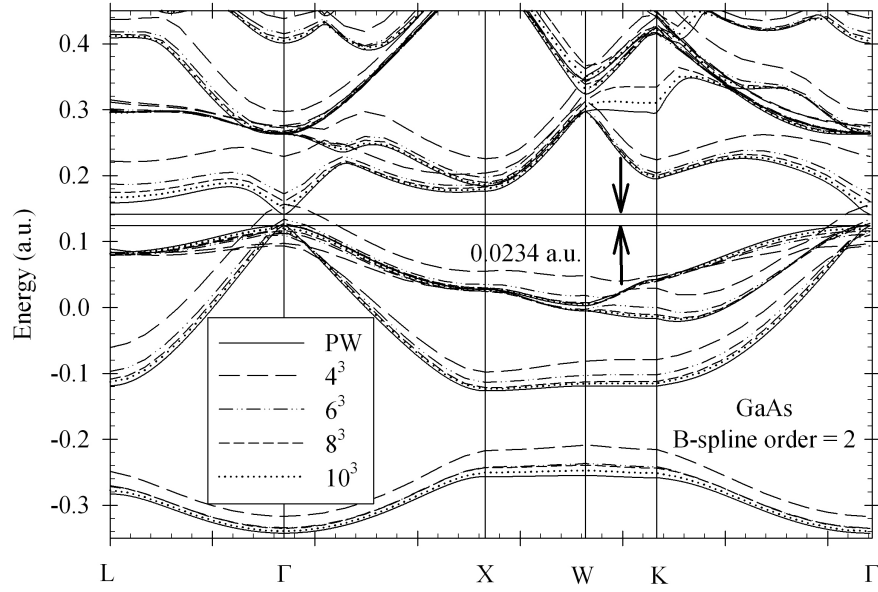


Figure 53. Band diagram for gallium arsenide (GaAs) and B-spline order  $p = 2$

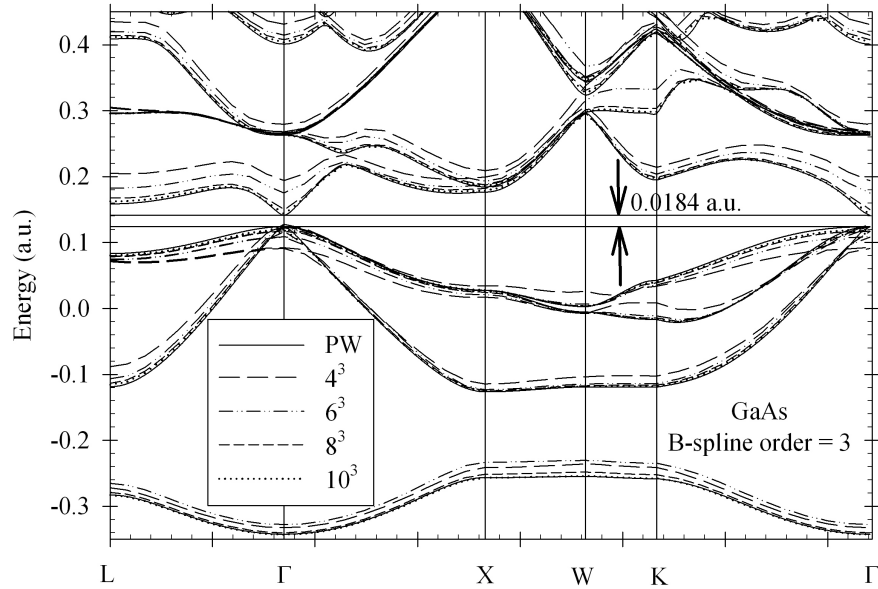


Figure 54. Band diagram for gallium arsenide (GaAs) and B-spline order  $p = 3$



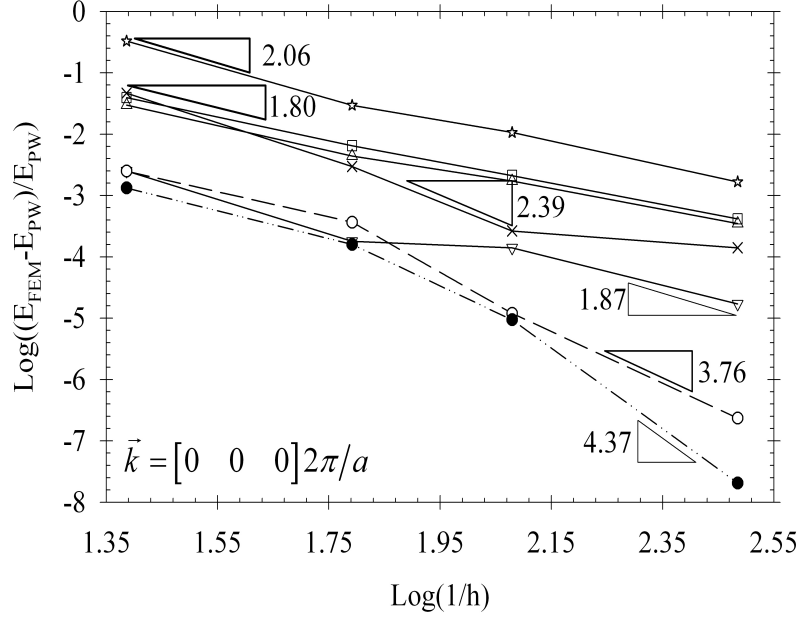


Figure 55. Convergence rates for gallium arsenide (GaAs) and B-spline order  $p = 2$

HGH pseudopotentials [4] and Perdew-Zunger exchange-correlation potential [69] were used in this case of finite element calculations. Planewave solutions were obtained from Pask *et al.* [1]. Figures 53-54 plot the band diagrams along high-symmetry lines of first Brillouin zone. PW method predicts a band gap of 0.0173 Hartree atomic units. Optimum convergence rates are obtained for eigenvalues and super-convergence for total energies (because of higher order inter-element continuity of B-spline basis functions) as shown above in Figure 55.

#### 4.3.4.4 Graphene (3D case)

The domain or unit cell is defined by the following primitive lattice vectors.

$$\mathbf{a}_1 = (a, 0, 0), \mathbf{a}_2 = \left(a/2, \sqrt{3}/2a, 0\right), \mathbf{a}_3 = (0, 0, 3a) \quad (4.82)$$

where  $a = \sqrt{3}a_{CC}$ . The lattice parameter  $a_{CC} = 2.6834 \text{ a.u.}$  is shown in Figure 56.

Figure 56 shows the 2D primitive unit cell and first Brillouin zone for a graphene sheet. However, for computations in 3D we consider the length in third dimension as thrice the lattice parameter  $a_{CC}$  (with carbon atoms located in a plane that is exactly in the middle of third dimension) and periodic boundary conditions are assumed on the surfaces in all three directions. The irreducible Brillouin zone of graphene is  $1/12^{th}$  of the part of first Brillouin zone and 110  $\mathbf{k}$  points were considered in irreducible part for electron charge density integration. Figure 57 shows the band diagram plot along high symmetry points. Both the  $\sigma$  and  $\pi$  bands are captured as shown above.

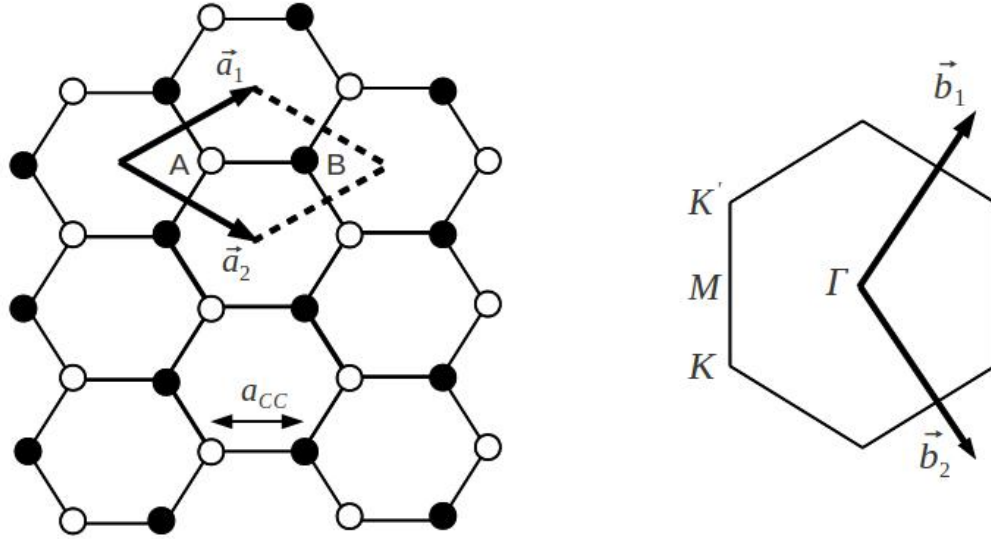


Figure 56. Primitive unit cell and First Brillouin zone with high-symmetry points

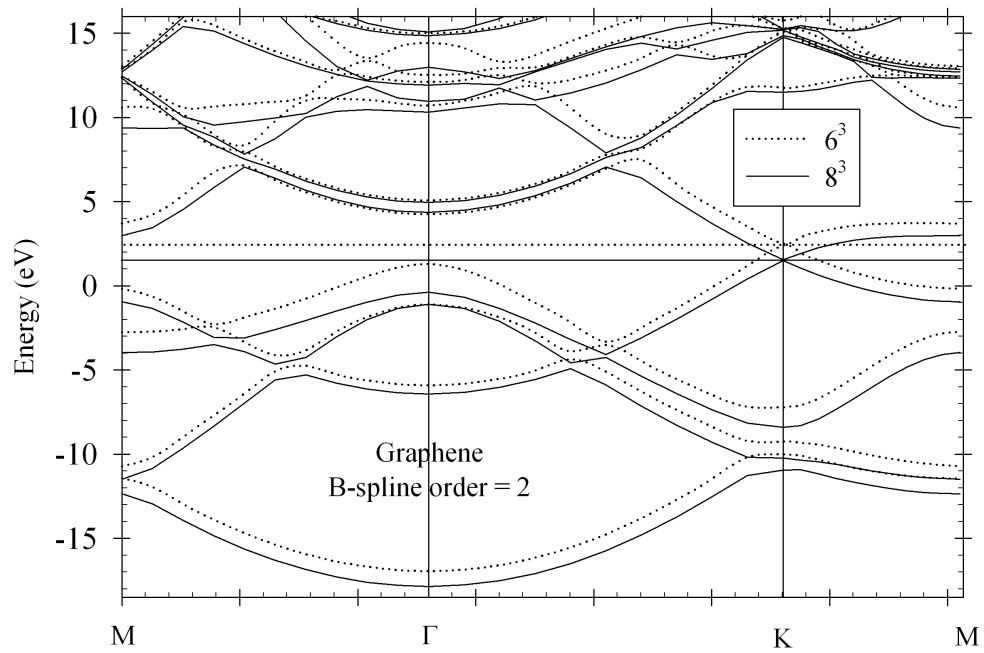


Figure 57. Band diagram for graphene and B-spline order  $p = 2$

## 5 CONCLUDING REMARKS AND FUTURE WORK

The thesis presents a finite element multiscale variational framework for analysis of materials involving coupled mechanical and electronic properties. The framework can be extended to include thermal and other effects.

In Chapter 2, we have presented a hierarchical multiscale computational framework for bridging the gap between molecular mechanics at nanoscales and quasi-continuum mechanics at microscales in the modeling of CNTs. The proposed two-level scale separation results in a coupled self-consistent system of equations which is then systematically decoupled to yield a set of equations for modeling defect-free CNTs, and a second set for modeling the defects in CNTs. The ensuing finite element method also furnishes two level statement of the problem, with level-one providing a method for modeling defect free nanostructure, and level-two providing a method for modeling defects in the nanostructure. In the quasi-continuum model interatomic interactions are incorporated via nanoscale material moduli that are based on interatomic potentials which are in turn functions of the local state of deformation. Two types of interatomic potentials, i.e., modified Morse potentials and the Tersoff-Brenner potentials are employed in the evaluation of nanoscale material moduli. The concept of formation energy of vacancy is employed to extract the fine scale force fields that are then used in the level-two finite element discretization to model defects. Point defects that arise because of vacancies and

affect atomic structure locally are discretely modeled. Representative numerical examples are shown to validate the model and demonstrate its range of applicability.

In Chapter 3, we presented two finite element formulations for the solution of the Schrödinger wave equation, (a) GLS formulation, and (b) HVM formulation. The GLS formulation when reduced to the standard eigenvalue problem, yields solution at a computational cost that is comparable to that of the Galerkin method, however with higher accuracy in the evaluation of the higher eigenvalues as compared to the Galerkin method. The HVM formulation also yields optimal convergence rates, however it leads to a quadratic eigenvalue problem that adds to the cost of computation. The numerical convergence rates of the methods are investigated via the Kronig-Penney problem that serves as a benchmark test case for investigating the mathematical properties of the methods. The quadratic elements show a substantial gain in accuracy as compared to the 3D linear elements. Amongst the quadratic elements, quadratic bricks show better accuracy as compared to the quadratic tetrahedral element.

In Chapter 4, We have presented here a real-space variational finite element framework for self-consistent solution of periodic Kohn-Sham equations. Lagrange basis functions has  $C^0$  continuity between elements. We have employed B-splines and NURBS basis functions, which provides higher order inter-element continuity. Higher order Lagrange basis functions oscillate around the solution. This is called as Gibbs phenomenon. Higher order B-splines and NURBS have variation diminishing property [46] and do not display Gibb's phenomenon. This is especially useful in representing high gradient functions using higher order B-spline and NURBS basis functions. In addition NURBS functions can exactly represent geometries that includes conic sections (cylinders, spheres etc.), where boundary conditions can be imposed exactly and

thus avoid errors due to approximation of geometries. Since B-Splines and NURBS provide local support they provide significant advantages over planewave basis functions in parallel implementation by minimizing communication between processors. Thus some of the shortcomings addressed in [70] with respect to geometry of domain and lower order of polynomials have been addressed here. In addition real space formulations enables all types of boundary conditions to be implemented with ease. Since different meshes are employed for Poisson and Schrödinger wave equation (SWE), it is trivial to implement solution in different size domains for non-periodic systems where Poisson problem need to be solved in a larger domain while SWE in a smaller domain.

Having established the method by comparison to PW *ab-initio* methods, as part of future work, parallelization of code is underway to study large scale coupled problems involving electronic/mechanical/thermal properties and defects presently. Some of the applications include flexible electronics in biomedical applications, thermoelectric devices, and generally any silicon based electronic devices.

## APPENDICES

## A THE NON-LOCAL TERM

The non-local term embedded within  $V_{eff}$  requires further explanation. The non-local term can be expanded as follows using equation (4.23).

$$\int_{\Omega^e} (e^{-i\mathbf{k}\bullet\mathbf{x}} N_i V^{nL} e^{i\mathbf{k}\bullet\mathbf{x}} N_j) d\mathbf{x} = \sum_{a,l,m} \left\{ \begin{array}{l} \int_{\Omega^e} (e^{-i\mathbf{k}\bullet\mathbf{x}} \sum_n [e^{i\mathbf{k}\bullet\mathbf{R}_n} \chi_{lm}^a(\mathbf{x} - \boldsymbol{\tau}_a - \mathbf{R}_n)] N_i(\mathbf{x}) d\mathbf{x}) \times h_l^a \times \\ \int_{\Omega} (e^{i\mathbf{k}\bullet\mathbf{x}'} \sum_{n'} [e^{-i\mathbf{k}\bullet\mathbf{R}_{n'}} \chi_{lm}^a(\mathbf{x}' - \boldsymbol{\tau}_a - \mathbf{R}_{n'})] N_j(\mathbf{x}') d\mathbf{x}') \end{array} \right\} \quad (\text{A.1})$$

where  $\int_{\Omega^e}$  stands for integration over an element domain  $\Omega^e$  of finite element mesh, while  $\int_{\Omega}$  stands for integration over the entire domain  $\Omega$  or the unit cell. Hence this non-local term leads to fully populated stiffness matrix as shown below by expanding the terms in matrix form.

**Remark A.1:** *The blue term in equation (A.2) is localized since the integral is over an element domain  $\Omega^e$  and the shape functions have local support, i.e. only a few shape functions have non-zero values. This implies that the element level non-local term occupies only rows associated with the element  $e$  of the global stiffness matrix.*

**Remark A.2:** *The red term in equations (A.2) and (A.3) is nonlocal, since the integral is defined over the entire domain or unit cell,  $\Omega$ , despite the shape functions having local support. This implies that all shape functions in this term necessarily have non-zero values. As a result of this term the element stiffness matrix occupies all the columns of global stiffness matrix.*



# Appendix A (Continued)

$$\begin{aligned}
& \int_{\Omega^e} (w(\mathbf{x}) e^{-i\mathbf{k} \bullet \mathbf{x}} V^{nL} e^{i\mathbf{k} \bullet \mathbf{x}} v(\mathbf{x})) d\mathbf{x} = \sum_{a,l,m} \\
& \left\{ \begin{aligned} & \int_{\Omega^e} (e^{-i\mathbf{k} \bullet \mathbf{x}} \sum_n [e^{i\mathbf{k} \bullet \mathbf{R}_n} \chi_{lm}^a(\mathbf{x} - \boldsymbol{\tau}_a - \mathbf{R}_n)] w(\mathbf{x}) d\mathbf{x}) \times h_l^a \\ & \times \int_{\Omega} (e^{i\mathbf{k} \bullet \mathbf{x}'} \sum_{n'} [e^{-i\mathbf{k} \bullet \mathbf{R}_{n'}} \chi_{lm}^a(\mathbf{x}' - \boldsymbol{\tau}_a - \mathbf{R}_{n'})] v(\mathbf{x}') d\mathbf{x}') \end{aligned} \right\} = \sum_{a,l,m} \\
& \left\{ \begin{aligned} & \begin{bmatrix} d_1 \\ d_2 \\ \vdots \\ d_n \end{bmatrix}^T \int_{\Omega^e} \begin{pmatrix} N_1(\mathbf{x}) \\ N_2(\mathbf{x}) \\ \vdots \\ N_n(\mathbf{x}) \\ \sum_n [e^{i\mathbf{k} \bullet \mathbf{R}_n} \chi_{lm}^a(\mathbf{x} - \boldsymbol{\tau}_a - \mathbf{R}_n)] \end{pmatrix} e^{-i\mathbf{k} \bullet \mathbf{x}} \times d\mathbf{x} \times h_l^a \times \\ & \int_{\Omega} \begin{pmatrix} e^{i\mathbf{k} \bullet \mathbf{x}'} \sum_{n'} [e^{-i\mathbf{k} \bullet \mathbf{R}_{n'}} \chi_{lm}^a(\mathbf{x}' - \boldsymbol{\tau}_a - \mathbf{R}_{n'})] \times \\ \begin{bmatrix} N_1(\mathbf{x}) & N_2(\mathbf{x}) & \vdots & \vdots & N_n(\mathbf{x}) \end{bmatrix} \end{pmatrix} d\mathbf{x}' \\ & \begin{bmatrix} c_1 & c_2 & \vdots & \vdots & c_n \end{bmatrix}^T \end{aligned} \right\} \quad (\text{A.2})
\end{aligned}$$

where

$$\begin{aligned}
& \int_{\Omega} \begin{pmatrix} e^{i\mathbf{k} \bullet \mathbf{x}'} \sum_{n'} [e^{-i\mathbf{k} \bullet \mathbf{R}_{n'}} \chi_{lm}^a(\mathbf{x}' - \boldsymbol{\tau}_a - \mathbf{R}_{n'})] \times \\ \begin{bmatrix} N_1(\mathbf{x}) & N_2(\mathbf{x}) & N_3(\mathbf{x}) & N_4(\mathbf{x}) & \dots & N_n(\mathbf{x}) \end{bmatrix} \end{pmatrix} d\mathbf{x}' = \\
& \sum_{e=1}^{numel} \int_{\Omega^e} \begin{pmatrix} e^{i\mathbf{k} \bullet \mathbf{x}'} \sum_{n'} [e^{-i\mathbf{k} \bullet \mathbf{R}_{n'}} \chi_{lm}^a(\mathbf{x}' - \boldsymbol{\tau}_a - \mathbf{R}_{n'})] \times \\ \begin{bmatrix} N_1(\mathbf{x}) & N_2(\mathbf{x}) & N_3(\mathbf{x}) & N_4(\mathbf{x}) & \dots & N_n(\mathbf{x}) \end{bmatrix} \end{pmatrix} d\mathbf{x}' \quad (\text{A.3})
\end{aligned}$$

## B PSEUDOPOTENTIAL

The local pseudopotential term for HGH pseudopotential [4] is converted into its equivalent density as follows. The plots of potential as well as density terms are shown to give a comparison of long range behavior of local pseudopotential term to short range behavior of density. The advantage of using the density is that one need not consider large number of atoms to achieve accuracy in numerical calculation at a location  $\mathbf{x}$ .

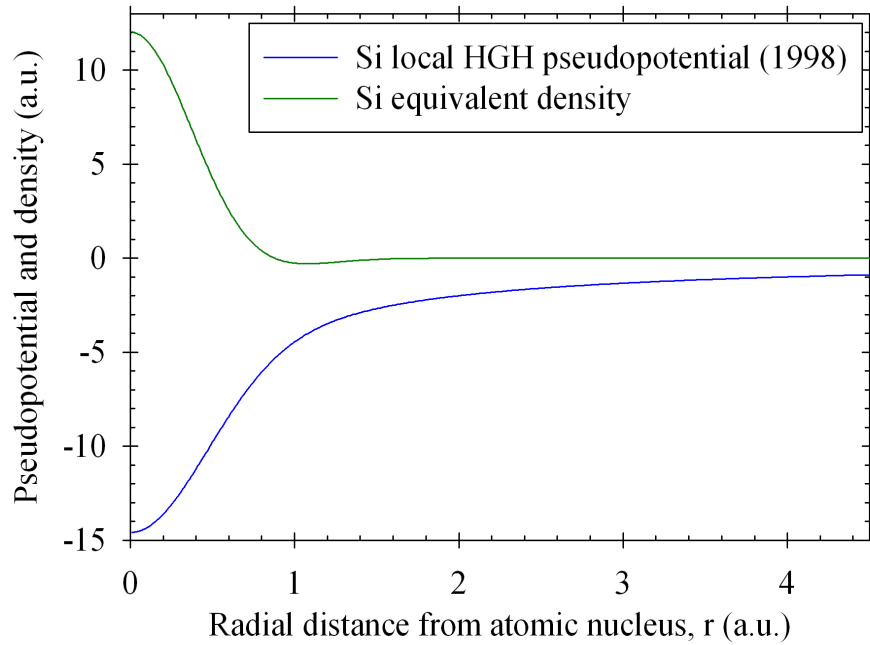


Figure 58. Silicon Local pseudopotential [2, 4] and its corresponding charge density

## CITED LITERATURE

1. Pask, J. and Sterne, P.: Finite element methods in ab initio electronic structure calculations. Modelling and Simulation in Materials Science and Engineering, 13:R71, 2005.
2. Pask, J., Klein, B., Sterne, P., and Fong, C.: Finite-element methods in electronic-structure theory. Computer physics communications, 135(1):1–34, 2001.
3. Chang, T. and Gao, H.: Size-dependent elastic properties of a single-walled carbon nanotube via a molecular mechanics model. Journal of the Mechanics and Physics of Solids, 51(6):1059–1074, 2003.
4. Hartwigsen, C., Goedecker, S., and Hutter, J.: Relativistic separable dual-space Gaussian pseudopotentials from H to Rn. Physical Review B, 58(7):3641–3662, 1998.
5. Iijima, S. et al.: Helical microtubules of graphitic carbon. nature, 354(6348):56–58, 1991.
6. Maiti, A.: Carbon nanotubes: Bandgap engineering with strain. Nature Materials, 2(7):440–442, 2003.
7. Pitkethly, M.: Nanomaterials-the driving force. Materials Today, 7:20–29, 2004.
8. Qian, D., Wagner, G., Liu, W., Yu, M., and Ruoff, R.: Mechanics of carbon nanotubes. Applied Mechanics Reviews, 55:495, 2002.
9. Liu, W., Karpov, E., Zhang, S., and Park, H.: An introduction to computational nanomechanics and materials. Computer Methods in Applied Mechanics and Engineering, 193(17-20):1529–1578, 2004.
10. Belytschko, T., Xiao, S., Schatz, G., and Ruoff, R.: Atomistic simulations of nanotube fracture. Physical Review B, 65(23):235–430, 2002.

# CITED LITERATURE (Continued)

11. Belytschko, T. and Xiao, S.: Coupling methods for continuum model with molecular model. International Journal for Multiscale Computational Engineering, 1(1):115–126, 2003.
12. Arroyo, M. and Belytschko, T.: Continuum mechanics modeling and simulation of carbon nanotubes. Mechanica, 40(4):455–469, 2005.
13. Yakobson, B., Brabec, C., and Bernholc, J.: Nanomechanics of carbon tubes: Instabilities beyond linear response. Physical Review Letters, 76(14):2511–2514, 1996.
14. Nardelli, M., Yakobson, B., and Bernholc, J.: Brittle and ductile behavior in carbon nanotubes. Physical review letters, 81(21):4656–4659, 1998.
15. Morse, P.: Diatomic molecules according to the wave mechanics. II. vibrational levels. Physical Review, 34(1):57, 1929.
16. Tersoff, J.: Empirical interatomic potential for carbon, with applications to amorphous carbon. Physical Review Letters, 61(25):2872–2879, 1988.
17. Tersoff, J.: Empirical interatomic potential for carbon, with applications to amorphous carbon. Physical Review Letters, 61(25):2879–2882, 1988.
18. Brenner, D.: Empirical potential for hydrocarbons for use in simulating the chemical vapor deposition of diamond films. Physical Review B, 42(15):9458–9471, 1990.
19. Brenner, D., Shenderova, O., Harrison, J., Stuart, S., Ni, B., and Sinnott, S.: A second-generation reactive empirical bond order (REBO) potential energy expression for hydrocarbons. Journal of Physics: Condensed Matter, 14:783–802, 2002.
20. Goze, C., Vaccarini, L., Henrard, L., Bernier, P., Hernandez, E., and Rubio, A.: Elastic and mechanical properties of carbon nanotubes. Synthetic Metals, 103(1-3):2500–2501, 1999.
21. Popov, V., Van Doren, V., and Balkanski, M.: Elastic properties of single-walled carbon nanotubes. Physical Review B, 61(4):3078–3084, 2000.
22. Zhang, S., Khare, R., Lu, Q., and Belytschko, T.: A bridging domain and strain computation method for coupled atomistic–continuum modelling of solids. International journal for numerical methods in engineering, 70(8):913–933, 2007.

### CITED LITERATURE (Continued)

23. Peng, Z., Yonggang, H., Geubelle, P., and Kehchih, H.: On the continuum modeling of carbon nanotubes. Acta Mechanica Sinica, 18(5):528–536, 2002.
24. Zhang, P., Huang, Y., Geubelle, P., Klein, P., and Hwang, K.: The elastic modulus of single-wall carbon nanotubes: a continuum analysis incorporating interatomic potentials. International Journal of Solids and Structures, 39(13-14):3893–3906, 2002.
25. Chong, K.: Nanoscience and engineering in mechanics and materials. Journal of Physics and Chemistry of Solids, 65(8-9):1501–1506, 2004.
26. Liu, B., Jiang, H., Huang, Y., Qu, S., Yu, M., and Hwang, K.: Atomic-scale finite element method in multiscale computation with applications to carbon nanotubes. Physical Review B, 72(3):035435, 2005.
27. Zhou, L. and Shi, S.: Formation energy of Stone–Wales defects in carbon nanotubes. Applied physics letters, 83:1222–1224, 2003.
28. Li, L., Reich, S., and Robertson, J.: Defect energies of graphite: density-functional calculations. Physical Review B, 72(18):184109, 2005.
29. Pask, J.: A finite-element method for large-scale ab initio electronic structure calculations. Ph.d. thesis, University of California, Davis, 1999.
30. Pask, J., Klein, B., Fong, C., and Sterne, P.: Real-space local polynomial basis for solid-state electronic-structure calculations: A finite-element approach. Physical Review B, 59(19):12352, 1999.
31. Jun, S. and Liu, W.: Moving Least-Square Basis for Band-Structure Calculations of Natural and Artificial Crystals. Material substructures in complex bodies: from atomic level to continuum, page 163, 2007.
32. Chelikowsky, J., Troullier, N., and Saad, Y.: Finite-difference-pseudopotential method: Electronic structure calculations without a basis. Physical review letters, 72(8):1240–1243, 1994.
33. Chelikowsky, J., Troullier, N., Wu, K., and Saad, Y.: Higher-order finite-difference pseudopotential method: An application to diatomic molecules. Physical Review B, 50(16):11355, 1994.

### CITED LITERATURE (Continued)

34. Hughes, T.: Multiscale phenomena: Green's functions, the Dirichlet-to-Neumann formulation, subgrid scale models, bubbles and the origins of stabilized methods. Computer methods in applied mechanics and engineering, 127(1-4):387–401, 1995.
35. Masud, A. and Franca, L.: A hierarchical multiscale framework for problems with multiscale source terms. Computer Methods in Applied Mechanics and Engineering, 197(33-40):2692–2700, 2008.
36. Masud, A. and Hughes, T.: A stabilized mixed finite element method for Darcy flow. Computer Methods in Applied Mechanics and Engineering, 191(39-40):4341–4370, 2002.
37. Masud, A. and Khurram, R.: A multiscale/stabilized finite element method for the advection-diffusion equation. Computer methods in applied mechanics and engineering, 193(21-22):1997–2018, 2004.
38. Masud, A. and Bergman, L.: Application of multi-scale finite element methods to the solution of the Fokker-Planck equation. Computer methods in applied mechanics and engineering, 194(12-16):1513–1526, 2005.
39. Masud, A. and Khurram, R.: A multiscale finite element method for the incompressible Navier-Stokes equations. Computer methods in applied mechanics and engineering, 195(13-16):1750–1777, 2006.
40. Masud, A. and Xia, K.: A variational multiscale method for inelasticity: Application to superelasticity in shape memory alloys. Computer methods in applied mechanics and engineering, 195(33-36):4512–4531, 2006.
41. Hohenberg, P. and Kohn, W.: Inhomogeneous electron gas. Physical Review, 136(3B):B864–B871, 1964.
42. Kohn, W., Sham, L., et al.: Self-consistent equations including exchange and correlation effects. Physical Review, 140(4A):A1133–A1138, 1965.
43. Martin, R.: Electronic structure: basic theory and practical methods. Cambridge Univ Pr, 2004.
44. Singh, D. and Nordström, L.: Planewaves, Pseudopotentials, and the LAPW method. Springer Verlag, 2006.

### CITED LITERATURE (Continued)

45. Pickett, W.: Pseudopotential methods in condensed matter applications. Computer Physics Reports, 9(3):115–197, 1989.
46. Hughes, T., Cottrell, J., and Bazilevs, Y.: Isogeometric analysis: CAD, finite elements, NURBS, exact geometry and mesh refinement. Computer Methods in Applied Mechanics and Engineering, 194(39-41):4135–4195, 2005.
47. Masud, A., Kannan, K., and Xia, K.: A multiscale framework for computational nanomechanics: application to carbon nanotubes. Proceedings of the 5th International Conference on Computation of Shell and Spatial Structures, (eds.) E. Ramm, W. A. Wall, K. U Bletzinger, M. Bischoff, Salzburg, Austria, June 1-4, 2005.
48. Masud, A. and Kannan, K.: A multiscale computational framework for the modeling of carbon nanotubes. Proceedings of the VIII International Conference on Computational Plasticity (COMPLAS VIII), (eds.) E. Onate, D. R. J. Owen, CIMNE Barcelona, Spain, September 5-8, 2005.
49. Xiao, J., Gama, B., Gillespie, J., et al.: An analytical molecular structural mechanics model for the mechanical properties of carbon nanotubes. International Journal of Solids and Structures, 42(11-12):3075–3092, 2005.
50. Jiang, H., Zhang, P., Liu, B., Huang, Y., Geubelle, P., Gao, H., and Hwang, K.: The effect of nanotube radius on the constitutive model for carbon nanotubes. Computational Materials Science, 28(3-4):429–442, 2003.
51. Mielke, S., Troya, D., Zhang, S., Li, J., Xiao, S., Car, R., Ruoff, R., Schatz, G., and Belytschko, T.: The role of vacancy defects and holes in the fracture of carbon nanotubes. Chemical Physics Letters, 390(4-6):413–420, 2004.
52. Tezduyar, T. and Osawa, Y.: Finite element stabilization parameters computed from element matrices and vectors. Comput. Methods Appl. Mech. Engrg, 190(411):430, 2000.
53. Strang, G. and Fix, G. J.: An analysis of the finite element method. Prentice-Hall, Englewood Cliffs, NJ, 1973.
54. Pierret, R.: Advanced semiconductor fundamentals. Addison-Wesley Longman Publishing Co., Inc. Boston, MA, USA, 1987.
55. Pulay, P.: Convergence acceleration of iterative sequences. The case of SCF iteration. Chemical Physics Letters, 73(2):393–398, 1980.

# CITED LITERATURE (Continued)

56. Bazilevs, Y., Gohean, J., Hughes, T., Moser, R., and Zhang, Y.: Patient-specific isogeometric fluid-structure interaction analysis of thoracic aortic blood flow due to implantation of the Jarvik 2000 left ventricular assist device. Computer Methods in Applied Mechanics and Engineering, 198(45-46):3534–3550, 2009.
57. Bazilevs, Y., Calo, V., Hughes, T., and Zhang, Y.: Isogeometric fluid-structure interaction: theory, algorithms, and computations. Computational Mechanics, 43(1):3–37, 2008.
58. Cottrell, J., Reali, A., Bazilevs, Y., and Hughes, T.: Isogeometric analysis of structural vibrations. Computer Methods in Applied Mechanics and Engineering, 195(41-43):5257–5296, 2006.
59. Benson, D., Bazilevs, Y., Hsu, M., and Hughes, T.: Isogeometric shell analysis: The Reissner-Mindlin shell. Computer Methods in Applied Mechanics and Engineering, 199(5-8):276–289, 2010.
60. Piegl, L. and Tiller, W.: The NURBS book. Springer Verlag, 1997.
61. Romanowski, Z.: A B-spline finite element solution of the Kohn–Sham equation for an atom. Modelling and Simulation in Materials Science and Engineering, 16:015003, 2008.
62. Kannan, R. and Masud, A.: Stabilized Finite Element Methods for the Schrodinger Wave Equation. Journal of Applied Mechanics, 76:021203, 2009.
63. Cohen, M. and Bergstresser, T.: Band structures and pseudopotential form factors for fourteen semiconductors of the diamond and zinc-blende structures. Physical Review, 141(2):789–796, 1966.
64. Monkhorst, H. and Pack, J.: Special points for Brillouin-zone integrations. Physical Review B, 13(12):5188–5192, 1976.
65. Vosko, S. and Wilk, L.: Influence of an improved local-spin-density correlation-energy functional on the cohesive energy of alkali metals. Physical Review B, 22(8):3812–3815, 1980.
66. Kotochigova, S., Levine, Z., Shirley, E., Stiles, M., and Clark, C.: Local-density-functional calculations of the energy of atoms. Physical Review A, 55(1):191–199, 1997.



**CITED LITERATURE (Continued)**

67. Kotochigova, S., Levine, Z., Shirley, E., Stiles, M., and Clark, C.: Erratum: Local-density-functional calculations of the energy of atoms [Phys. Rev. A 55, 191 (1997)]. Physical Review A, 56(6):5191–5192, 1997.
68. Kotochigova, S., Levine, Z., Shirley, E., Stiles, M., and Clark, C.: <http://www.nist.gov/pml/data/dftdata/index.cfm>.
69. Perdew, J. and Zunger, A.: Self-interaction correction to density-functional approximations for many-electron systems. Physical Review B, 23(10):5048–5079, 1981.
70. Suryanarayana, P., Gavini, V., Blesgen, T., Bhattacharya, K., and Ortiz, M.: Non-periodic finite-element formulation of Kohn-Sham density functional theory. Journal of the Mechanics and Physics of Solids, 58(2):256–280, 2010.

## VITA

Raguraman Kannan

### EDUCATION

**2011 PhD in Materials Engineering** (University of Illinois, Chicago, expected Aug 2011)

- **Advisor:** Arif Masud

**2002 MS in Mechanical Engineering**, Texas A&M University, College Station.

**1997 BE in Mechanical Engineering**, Bharathidasan University, India.

### EXPERIENCE

**2005-2011 Graduate Research Assistant** (University of Illinois, Chicago)

**2008-2010 Teaching Assistant**, University of Illinois, Urbana-Champaign.

**2004-2005 Teaching Assistant**, University of Illinois, Chicago.

### RESEARCH INTERESTS

Numerical modeling for novel materials involving multiscale and multiphysics phenomena (carbon nanotubes, silicon nanowires), method development to combine quasi-continuum and discrete models (molecular mechanics/dynamics quantum mechanics/dynamics), coupling algorithms in multiphysics problems involving combination electrical/electronic/mechanical/thermal properties (applications are flexible electronics, modeling point defects in materials).

## TEACHING INTERESTS

Continuum mechanics, applied mechanics of solids, theory of elasticity, statics and dynamics, structural mechanics/dynamics, linear/nonlinear/transient finite element methods, computational inelasticity.

## PROFESSIONAL MEMBERSHIP

American Society of Mechanical Engineers (ASME)

## PUBLICATIONS

1. Kannan, R., and Masud, A.: Stabilized Finite Element Methods for the Schrödinger Wave Equation. Journal of Applied Mechanics, 76:021203, 2009.
2. Masud, A., and Kannan, R.: A multiscale computational framework for the modeling of carbon nanotubes. International Journal for Numerical Methods in Engineering, 78(7):863–882, 2009.